GROWTH AND CHARACTERIZATION OF III-NITRIDES MATERIALS SYSTEM FOR PHOTONIC AND ELECTRONIC DEVICES BY METALORGANIC CHEMICAL VAPOR DEPOSITION

A Dissertation
Presented to
The Academic Faculty

by

Dongwon Yoo

In Partial Fulfillment
of the Requirements for the Degree
Doctor of Philosophy in the
School of Materials Science and Engineering

Georgia Institute of Technology
August 2007

GROWTH AND CHARACTERIZATION OF III-NITRIDES MATERIALS SYSTEM FOR PHOTONIC AND ELECTRONIC DEVICES BY METALORGANIC CHEMICAL VAPOR DEPOSITION

Approved by:

Dr. Russell D. Dupuis, Advisor
School of Materials Science and Engineering
Georgia Institute of Technology

Dr. Christopher J. Summers
School of Materials Science and Engineering
Georgia Institute of Technology

Dr. Zhong Lin Wang
School of Materials Science and Engineering
Georgia Institute of Technology

Dr. Joy Laskar
School of Electrical and Computer Engineering
Georgia Institute of Technology

Dr. Shyh-Chiang Shen
School of Electrical and Computer Engineering
Georgia Institute of Technology

Date Approved: July 3rd 2007

ACKNOWLEDGEMENTS

There are many people who have given me precious guidance for reaching this point of my research career. I would like to express my sincere gratitude to all those who helped make the present work possible. First and foremost, I am indebted to my academic advisor Dr. Russell Dupuis. I would like to thank him, for providing the valuable opportunity in the field of MOCVD and the endless support to carrying out research work. His guidance full of academic and technical knowledge over my entire period in the Advanced Materials and Devices Group has been invaluable, and he has also challenged me to the best engineer possible; for that I am really grateful.

I would also like to thank Dr. Jae-Hyun Ryou who has always provided the guidance. I consider myself extremely fortunate to be able to work with the talented and selfless individuals past and present for their cooperation in research, encouragement, and discussions. Without them, I could not have accomplished the research described in this thesis. The generous support of DARPA, NASA, Epichem, and others is also gratefully recognized.

Finally and the most importantly, I would like to thank my entire family for all of their support. I owe much to my wife Yoon who has provided all her love throughout my time. For giving me everything to be where I am today, I cannot thank my parents, Kyongwi Kim Yoo and Dr. Yeonchul Yoo enough. I must mention that their endless love, wisdom and encouragement has sustained throughout my life.

TABLE OF CONTENTS

LIST OF TABLES

LIST OF FIGURES

SUMMARY

Within the past ten years, a wide variety of group III-Nitride-based photonic and electronic devices have opened a new era in the field of semiconductor research. Fueled by their great potential which extends beyond the capabilities of Si technology, they have become of great commercial importance. The direct and large bandgap nature, intrinsic high carrier mobility, and the capability of forming heterostructures allow them to dominate photonic and electronic device market such as light emitters, photodiodes, or high-speed/high-power electronic devices.

Avalanche photodiodes (APDs) based on group III-Nitride materials are of interest due to their potential capability for low dark current densities, high sensitivities and high optical gains in the ultraviolet (UV) spectral region. Wide-bandgap GaN-based APDs, such as AlGaN and GaN-based *p-i-n* diodes, are excellent candidates for short-wavelength photodetectors because they have the capability for cut-off wavelengths in the ultraviolet (UV) spectral region less than $\lambda = 290$ nm. These intrinsically solar-blind UV APDs will not require filters to operate in the solar-blind spectral regime at $\lambda < 290$ nm. A high density of defects is usually introduced during the growth of GaN-based heteroepitaxial layers on lattice-mismatched substrates; thereby, causing a device failure by premature microplasma breakdown before the electric field reaches the level of the bulk avalanche breakdown field, which has been a major issue for GaN-based APDs. In contrast, photomultiplier tubes (PMTs) offer high-sensitivity UV detection with a photocurrent gain as high as 10^6; however, PMTs require a high-voltage power supply (> 1,200V) and are relatively fragile and expensive. Due to their compact footprint and

material characteristics, APDs are small, stable, and less expensive compared with PMTs. The extensive research on epitaxial growth development and optimization of $Al_xGa_{1-x}N$ ($0 \leq x \leq 1$) epitaxial layers grown on low dislocation density native bulk III-N substrates have brought UV APDs into realization. GaN and AlGaN UV *p-i-n* APDs demonstrated first and record-high true avalanche gain of > 10,000 and 50. The large stable optical gain is attributed to the improved crystalline quality of epitaxial layers grown on low dislocation density bulk substrates.

The superior physical and electronic properties for group III-Nirides has brought much research interest to high speed/high power devices such as GaN *p-i-n* rectifiers. The AlN-free full-vertical GaN *p-i-n* rectifiers grown on *n*-type 6H-SiC substrates by employing a conducting AlGaN:Si buffer layer provide the advantage of the reduction of sidewall damage from plasma etching and lower forward resistance due to the reduction of current crowding in the bottom *n*-type layer. The AlGaN:Si nucleation layer was proven to provide excellent electrical properties while also acting as a good buffer layer for subsequent GaN growth. The reverse breakdown voltage for a relatively thin 2.5 μm-thick *i*-region was found to be over -400V. For GaN *p-i-n* rectifiers grown on bulk GaN substrates, the reverse blocking voltage of $V_r \sim$ -540V was demonstrated.

CHAPTER 1

INTRODUCTION TO GROUP III-NITRIDES

1.1 Application of Group III-Nitride Photonic and Electronic Devices

Within the past ten years, a wide variety of group III-Nitride-based photonic and electronic devices have opened a new era in the field of semiconductor research. Fueled by their great potential which extends beyond the capabilities of Si technology, they have become of great commercial importance. The direct and large bandgap nature, intrinsic high carrier mobility, and the capability of forming heterostructures allow them to dominate photonic and electronic device market such as light emitters, photodiodes, or high-speed/high-power electronic devices. By alloying and forming heterostructures with AlN or InN, GaN has wide wavelength coverage ranging from entire visible spectral range in addition to the infrared and deep ultraviolet (1771 nm ~ 200 nm, 0.7 eV ~ 6.2 eV) ranges. The high thermal and chemical stability of GaN give those devices the advantage of operating in hostile environments. Like most wide bandgap semiconductors, the nitrides exhibit superior radiation hardness compared to the other smaller bandgap counterparts such as Si or GaAs, allowing them to be incorporated into demanding space applications. For these reasons, the research on group III-Nitride semiconductor materials has attracted much attention in both the consumer and defense industries.

For the indirect bandgap semiconductors such as Si or Ge, the carrier recombination releases heat to the lattice, but for direct bandgap materials characterized by direct recombination, under forward bias, in the active region, electrons are injected from *n*-side and holes are injected from *p*-side. Photons can be easily produced by conduction band-to-valence band electron-hole recombination in the "active region." Compared to other sources of light, semiconductor light emitters are convenient and attractive due to their compactness, high efficiency, low-power consumption, long

lifetime, spectral purity, and speed. Semiconductor photonic devices can be found in numerous applications such as traffic lights, color display panels or white light sources for solid-state street/room lighting. Nowadays, they expand the applications to architectural decorative lightings as well as vehicle main head lights.

Beyond the purpose of visible illumination, a compact and efficient UV light source is expected to provide new applications, such as fluorescence-based bio-chemical agent detection, UV-based curing, or water sterilization and etc., because most biological molecules contain chemical bonds having strong optical resonance within the UV spectral range of approximately 270 nm to 350 nm. In addition, the capability of high sensitivity, extremely low noise, and low dark current densities in short-wavelength radiation in the ultraviolet (UV) spectral region makes group III-Nitride devices a prime candidate for high-efficiency UV photodetection or short-range covert communication in the battlefield.

1.2 Beginning of Group III-Nitride Research

The recent prosperity of group III-Nitride research was initiated by the demonstration of the metalorganic chemical vapor deposition (MOCVD) growth technique by Manasevit in late 1960's [1]. Shortly after this, Manasevit, et al. applied this technique to grow GaN on sapphire substrates.[2] The selection of an oxide substrate such as sapphire was mainly due to the unavailability of native bulk GaN substrates and the high temperature stability of these oxides; however, further development was slow due to growth related issues. Among other existing growth techniques such as hydride vapor phase epitaxy (HVPE), liquid phase epitaxy (LPE), or molecular beam epitaxy (MBE), MOCVD started to receive much attention due to its suitability of heterostructure epitaxy since Dupuis, et al. [3] demonstrated the capability of MOCVD for optoelectronic

devices by the high-efficiency solar cells with first device-quality heterostructures. In the initial stage of research for group III-Nitrides, GaN films had high background doping as well as high dislocation density. Yoshida, et al. [4] deposited an AlN buffer layer to overcome the nucleation problems of GaN grown directly on a sapphire substrate. This buffer layer technique was very effective in improving the overall material quality on sapphire, so the concept was applied to MOCVD growth by Amano et al in 1986.[5] The worldwide attention on the research of group III-Nitrides were stimulated by the success in the material quality improvement with low temperature GaN nucleation layer by Nakamura [6] in the early 1990's and later by the success in blue light emitting diodes (LEDs) and laser diodes (LDs) by Nakamura, et al. [7], leading toward the fundamental understanding of group III-Nitride material system.

1.3 Materials Properties

Like most semiconductors, the atom arrangement in the nitride semiconductors is tetrahedrally coordinated; therefore, each atomic site has the four nearest neighbors occupying the vertices of a tetrahedron. The wurtzite crystal structure consists of two interpenetrating hexagonal close packed sub-lattices. Each sub-lattice is shifted along the c-axis by 3/8 of the cell height. GaN, AlN, or InN exhibits a stable hexagonal wurtzite crystal structure rather than a meta-stable zincblende structure. In an ideal wurtzite structure, c/a ratio is 1.633. The deviation from the ideal c/a ratio increases as the electronegativity difference between group III atoms and group V atoms increases.[8] The c/a ratio can also be correlated with the differences in the electronegativity. AlN has 1.601 of c/a and GaN exhibits 1.627 while InN shows 1.612. The difference is attributed

to the creation of the dipole, resulting in polarization. The space group for the hexagonal wurtzite structure is $P6_3mc$ (C^4_{6v}). The $P6_3mc$ space group is created by the combination of a 6_3 screw-axis along the c-axis, a mirror parallel to the c-axis and a-axis, and a glide plane along the c-axis. The unit cell of the wurtzite crystal structure and the Wigner-Seitz unit cell are shown in Figure 1.1 (a) and (b), respectively. A dashed line indicates a tetrahedral bonding.

The Nitrogen atom has the strongest electronegativity among the group V elements. The large difference in electronegativity between nitrogen and group III elements adds a strong ionic bonding component to the covalent bonding between Ga, Al, or In, resulting in a tightly bonded crystal structure. In addition, the charge carriers in the valence band of III-nitrides are well localized due to the strong electron affinity of the nitrogen atoms. These characteristics make III-nitride semiconductors leading materials for high-power/high-temperature applications.

Nitrogen atoms create a large ionic bonding component in the III-nitride materials; thus, these atoms play an important role in forming a tightly bonded crystal structure. The bonding energy of AlN is 11.5 eV/atom while that of GaN is 8.9 eV/atom. In comparison, InN shows 7.7 eV/atom of bonding energy to 6.5 eV/atom from GaAs. The tightly bonded structure with a larger bonding energy contributes to a chemical bond length that is shorter in comparison to other semiconductors. Combined with the wide bandgap, this characteristic makes III-nitrides perfect candidate materials for many optoelectronic applications operating in hostile environments. Figure 1.2 shows the values of chemical bond lengths depicted for various semiconductors.[9] The bowing parameters for $Al_xGa_{1-x}N$ and $In_xGa_{1-x}N$ were neglected in Figure 1.2.

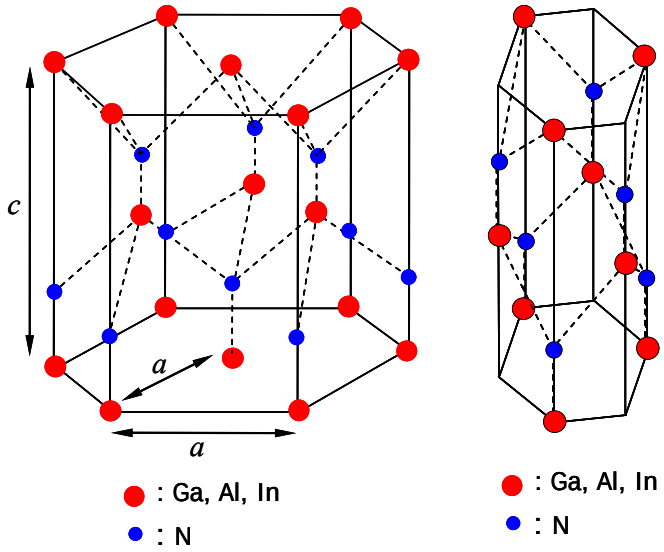

(a) (b)

Figure 1.1: (a) Unit cell for the hexagonal wurtzite structure (b) Wigner-Seitz unit cell for the III-nitrides.

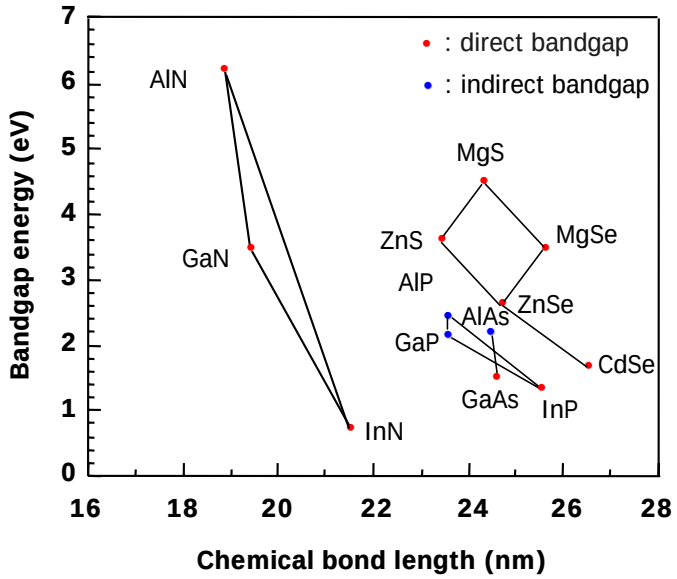

Figure 1.2: Bandgap energy versus chemical bond length for III-Nitrides and other semiconductors.

All of the III-Nitrides crystallize in stable wurtzite (hexagonal Bravais lattice) and zinc-blende (face-centered cubic Bravais lattice) polytypes. In a wurtzite form, the bandgaps are all direct. One of the advantages of the III-Nitride material system is that the bandgap can be tunable from 6.2 eV (~ 200 nm) to 0.7 eV (~1771 nm) by alloying and forming heterostructures with AlN and InN, respectively. The fundamental bandgap energy of approximately 0.7 eV for wurtzite-structure InN has been recently discovered [10,11,12,13,14,15,16,17,18], indicating InN is actually a narrow bandgap compound semiconductor. It is quite different from the previously, widely accepted value of 1.9 eV (~ 653 nm). The recent discovery of wide bandgap energy for InN gives group III-Nitride semiconductors a big advantage for devices operated under various conditions. For example, GaN alloyed with InN can be useful for devices for optical communications using long wavelengths such as $\lambda = 1.55$ or 1.33 μm.

Figure 1.3 displays bandgap energy as a function of *a* lattice parameter for the wurtzite III-Nitrides with E_g (AlN) = 6.2 eV, E_g (GaN) = 3.4 eV, and E_g (InN) = 0.7 eV. The zinc-blende energy gaps are slightly lower and are direct only for GaN and InN.[19] It is noted that the energy gap of the InAlN ternary alloy covers a wide range of spectrum from the infrared for InN to the deep ultraviolet for AlN. Hence, heterostructures of wurtzite group III-Nitride alloys can be incorporated into light emitters and detectors that operate in the entire range of the spectrum. The composition dependence of the bandgap for $Al_xIn_{1-x}N$ shown in Figure 1.3 can be described by the standard bowing equation 1.1.[16]

$$E_g^{AlInN}(x) = E_g^{AlN}(x) + E_g^{InN}(1-x) - bx(1-x) \tag{1.1}$$

The bowing parameter of b for AlInN is 2.53 eV obtained by ab initio pseudopotential calculation [20]. For InGaN and AlGaN material systems, bowing parameters are found to be 1.0 eV and 1.4 eV, respectively.[16,21]

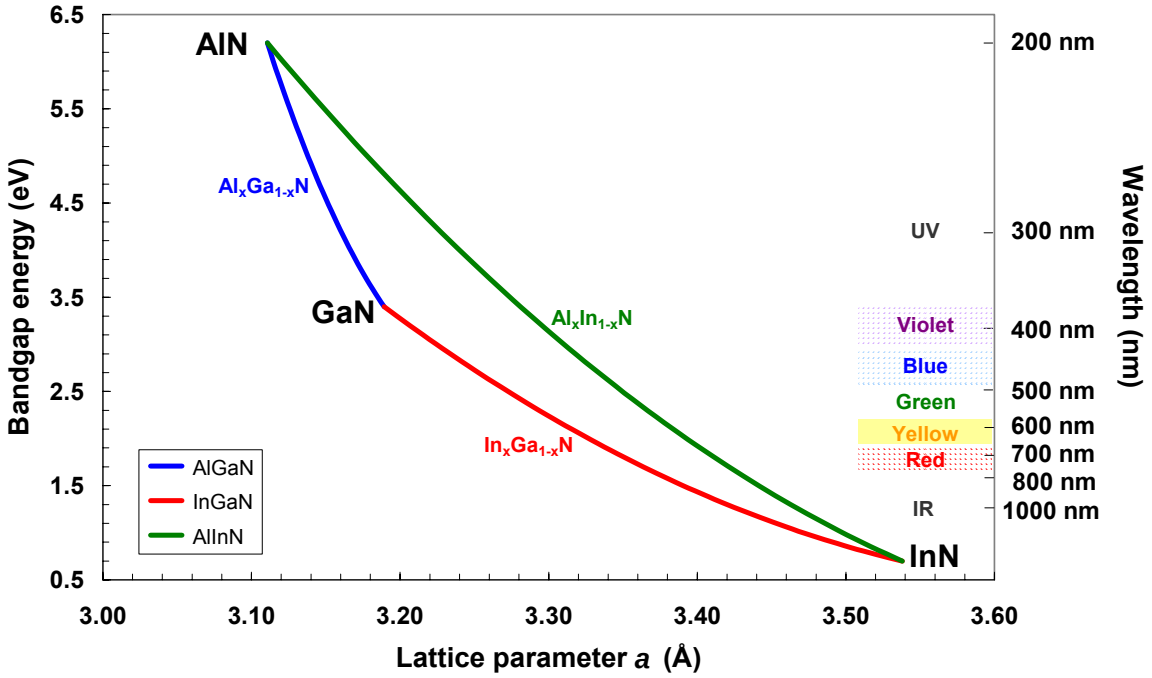

Figure 1.3: Energy bandgap (eV) as a function of lattice parameter (Å) for wurtzite III-Nitride alloys.

One of the technological difficulties of the group III-Nitirde system is that a lattice-matched substrate still has some limitations such as availability for bulk AlN or cost/substrate quality issue for large area bulk GaN substrate. Consequently, almost all of the previous research work was carried out using substrates that do not have a lattice matched condition. Despite of ~ 14.8% *a*-axis lattice mismatch over GaN, readily available low-cost, and high-thermal stability sapphire substrates are still used as platform in a variety of research activities. Since the growth of III-nitride

heterostructures takes place at an elevated temperature, the difference in thermal expansion between substrate and epitaxial layer also has to be taken into consideration. Table 1.1 [22] lists some of the important properties of the group III-Nitride materials.

Table 1.1: Material properties of GaN, AlN, and InN.

Property	GaN	AlN	InN
Lattice constant, a [Å]	3.189	3.112	3.548
Lattice constant, c [Å]	5.185	4.982	5.76
Thermal expansion ($\Delta a/a$) [10^{-6}/K]	5.59	4.2	4
Thermal expansion ($\Delta c/c$) [10^{-6}/K]	3.17	5.3	3
Thermal conductivity (κ) [W/cm·K]	1.3	2	0.8
Static dielectric constant (ε_0)	9.5	8.5	15
High-ω dielectric constant (ε_ω)	5.35	4.68	8.4
Electron effective mass (m_e)	$0.20m_0$	-	$0.11m_0$

As discussed earlier in this chapter, group III-Nitride materials have tightly bonded crystal structures due to the strong polarity of the bonding between group III and group V atoms. They are chemically stable and physically tolerant. For the wurtzite structure GaN, it has a high thermal conductivity and a high electron saturation velocity (v_s), which makes it a suitable material for power electronic devices. SiC has been known as the choice of substrate for high power/high temperature electronic devices partly due to very good thermal expansion coefficient match with AlN along the basal plane and partly due to advance in manufacturing technology [23] over other competing substrates. Unlike the case of AlN, the thermal expansion differs from GaN and InN by

more than 20%. The value of thermal expansion for sapphire is 78% greater than that of AlN and 34% larger than the case of GaN. This difference adds an additional difference of 0.34% and 0.20% in lattice parameter, respectively, due to thermal contraction while cooling down from the growth temperature.[9] For the growth of GaN on a SiC substrate, AlN grown at high temperature has been chosen as a buffer due to the small *a*-axis lattice mismatch of approximately 1% [24] for SiC-AlN. The *a*-axis thermal expansion ($\Delta a/a_0$) among GaN, AlN and 6H-SiC is plotted in Figure 1.4 based on the materials data.[25,26] Also, the a-axis lattice mismatch depending on the temperature change is shown in Figure 1.5. The mismatch is plotted based on ($a_{\text{AlN or GaN}} - a_{\text{SiC or AlN}}$)/$a_{\text{SiC or AlN}}$. Table 1.2 [27,28,29,30,31] summarizes some of the important properties of these materials.

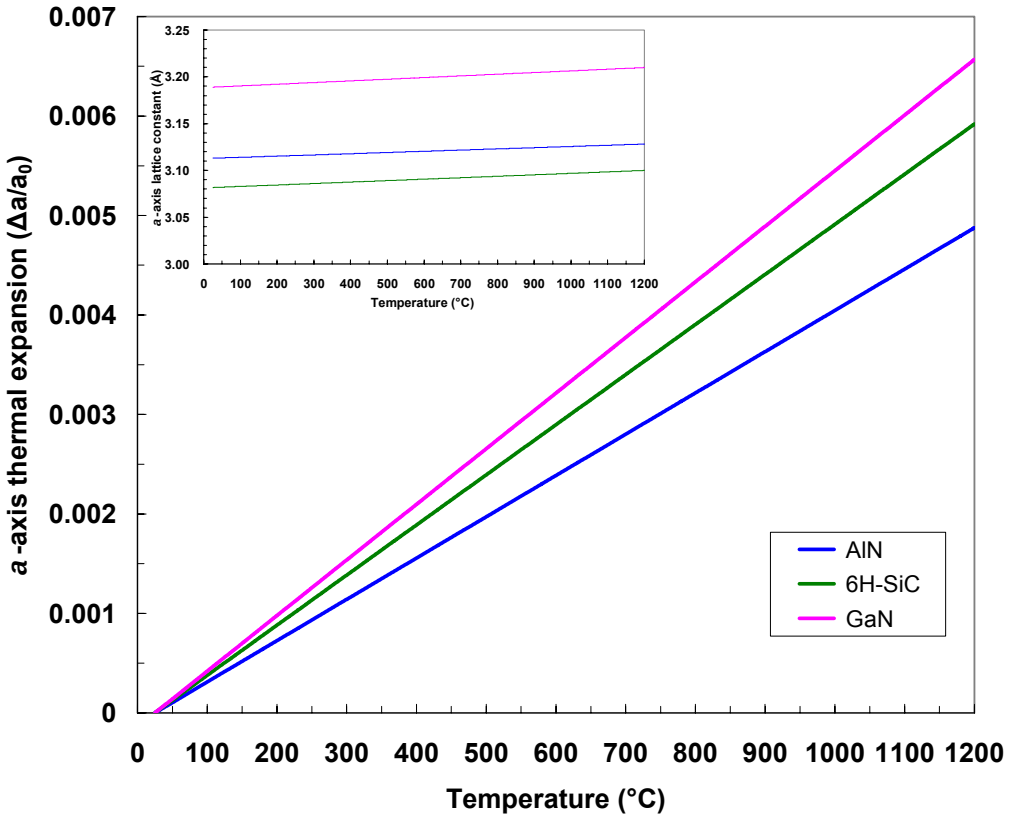

Figure 1.4: *a*-axis thermal expansion ($\Delta a/a_0$) for GaN, AlN and 6H-SiC with thermal expansion of *a*-axis lattice constant as inset.[25,26]

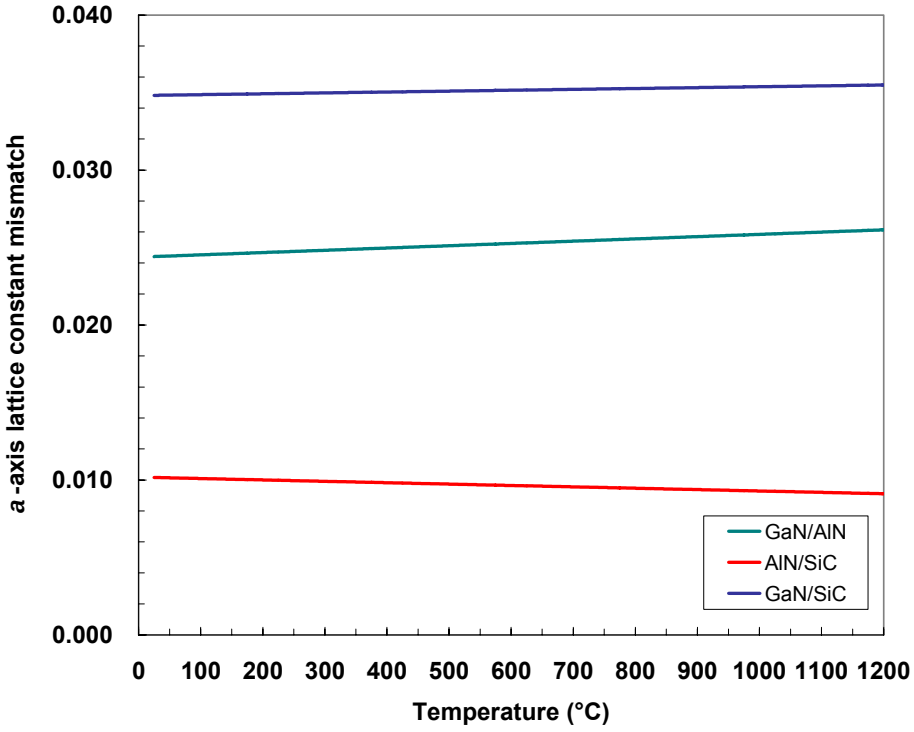

Figure 1.5: *a*-axis lattice mismatch for GaN, AlN and 6H-SiC.[25,26]

Table 1.2: Material properties of Si, 4H-SiC, 6H-SiC, and GaN.[27,28,29,30,31]

Material Property	Si	4H-SiC	6H-SiC	GaN
Bandgap (eV)	1.12	3.265	3.023	3.4
Breakdown field (10^5 V/cm)	3	18	22	35
Saturated velocity (10^7 cm/s)	1	1	2	2.5
Electron mobility ($cm^2/V{\cdot}s$)	1350	800	800	1000
Hole mobility ($cm^2/V{\cdot}s$)	450	120	120	30
Thermal conductivity (W/cm·K)	1.5	4.9	4.9	1.3
Dielectric constant (ε_0)	11.8	9.7	9.7	9.5

The crystal axis of GaN exhibits a 30° rotation relative to that of sapphire in the basal plane due to the large lattice mismatch of over 14%. SiC shows a closer match of lattice parameter and coefficient of thermal expansion than that of sapphire. The lattice mismatch and resulting misfit dislocation separation are listed in Table 1.3.[9]

Table 1.3: Lattice mismatch (%) and resulting misfit dislocation separation (Å) corresponding to complete misfit relaxation of basal plane interfaces.[9]

		GaN	AlN	InN	Sapphire	6H-SiC
Lattice mismatch (%)	Sapphire	14.8	12.5	25.4	·	11.5
	SiC	3.3	1	14	-11.5	·
	GaN	·	-2.4	10.6	-14.8	-3.3
Dislocation distance (Å)	Sapphire	17.2	20.3	10.6	·	21.9
	SiC	8.09	276.7	20.4	21.9	·
	GaN	·	114.4	27.3	17.2	80.9

1.4 Metalorganic Chemical Vapor Deposition

In CVD, two or more materials in a gaseous form are introduced into a reaction chamber where they chemically react with one another to form a new material deposited on the wafer surface. The MOCVD growth technique involves a sequence of chemical reactions among different precursors. A metalorganic (or alkyl) precursor exists in either liquid or solid form and is stored in an all welded stainless steel container, commonly referred to as "bubbler". A carrier gas passes (or bubbles) through this precursor container and carries metalorganic precursor molecules into an epitaxial growth chamber; thus, precursors must exhibit an appropriate volatility. Also, precursors should have the proper reactivity to thermally decompose in an epitaxial growth chamber. Hence, for the selection of suitable precursors, vapor pressure and pyrolysis data should be taken into

consideration. Trimethylgallium (TMGa), triethylgallium (TEGa), trimethylaluminum (TMAl), and trimethylindium (TMIn) are commonly used as group III precursors in the group III-Nitride epitaxy. The general reaction to form group III-Nitrides is described by the equation 1.2.

$$R_3M + NH_3 \leftrightarrow MN + 3 \cdot RH \tag{1.2}$$

In this equation, R is an alkyl group, for example, methyl (CH_3) or ethyl (C_2H_5) and M represents the group III metal such as gallium (Ga), aluminum (Al), or indium (In). N represents the group V elements such as P, As, N, or Sb, and H is hydrogen. In the case of GaN, trimethylgallium (TMGa) and ammonia (NH_3) react based on the equation 1.3.

$$(CH_3)Ga + NH_3 \leftrightarrow GaN + 3 \cdot CH_4 \tag{1.3}$$

Unlike group III precursors, group V species are already in gaseous form under normal conditions. The extremely low dissociation rate by the order of 10^{-16} of the dimer molecule of nitrogen at typical growth temperatures limits the use of nitrogen as a group V precursor [32]. Instead, ammonia (NH_3) is commonly employed, due to its decomposition rate of 4% up to 950°C [33].

The MOCVD growth process can be categorized into four processes, i.e., gas input, pyrolysis, diffusion, and surface reaction. Then, a by-product formed during the epitaxial growth such as CH_4 is pumped away with carrier gases. Figure 1.6 shows the schematic illustration of GaN epitaxial growth. Epitaxial materials used in this dissertation were grown metalorganic chemical vapor deposition (MOCVD) using a reactor system (manufactured by Thomas Swan Scientific Equipments) equipped with Close-Coupled Showerhead (CCS)^{TM} growth technology. For a vertical rotating disk

reactor, stable flow regimes exist in a growth chamber at certain combinations of spinning rate, flow rate, pressure and temperature in vertical reactor design [34], but these parameters do not apply to CCS technology. CCS technology can provide inherent growth uniformity due to diffusion governed by mass transport from completely and uniformly intermixed gas phases. As shown in Figure 1.7 [35], metalorganic group III precursors are introduced into the top plenum chamber and hydrides precursors are introduced into the lower plenum chamber through a water-cooled showerhead surface over the entire area of deposition. The showerhead is constructed to enable precursors to be separated right up to the point where they are injected onto the substrates via high density of injection nozzles. The complete intermixed uniform distribution of gas phases is created at approximately 5 mm out of total 11 mm spacing between the showerhead and a substrate. The linear vertical temperature distribution in a growth chamber with CCS configuration can lead to high uniformity precursor decomposition efficiency. In addition, close packed wafer configuration results in high area utilization. These two factors produce high precursor utilization efficiency. The three-zone heater system creates the temperature uniformity via modification of the temperature profile, resulting in higher yield.

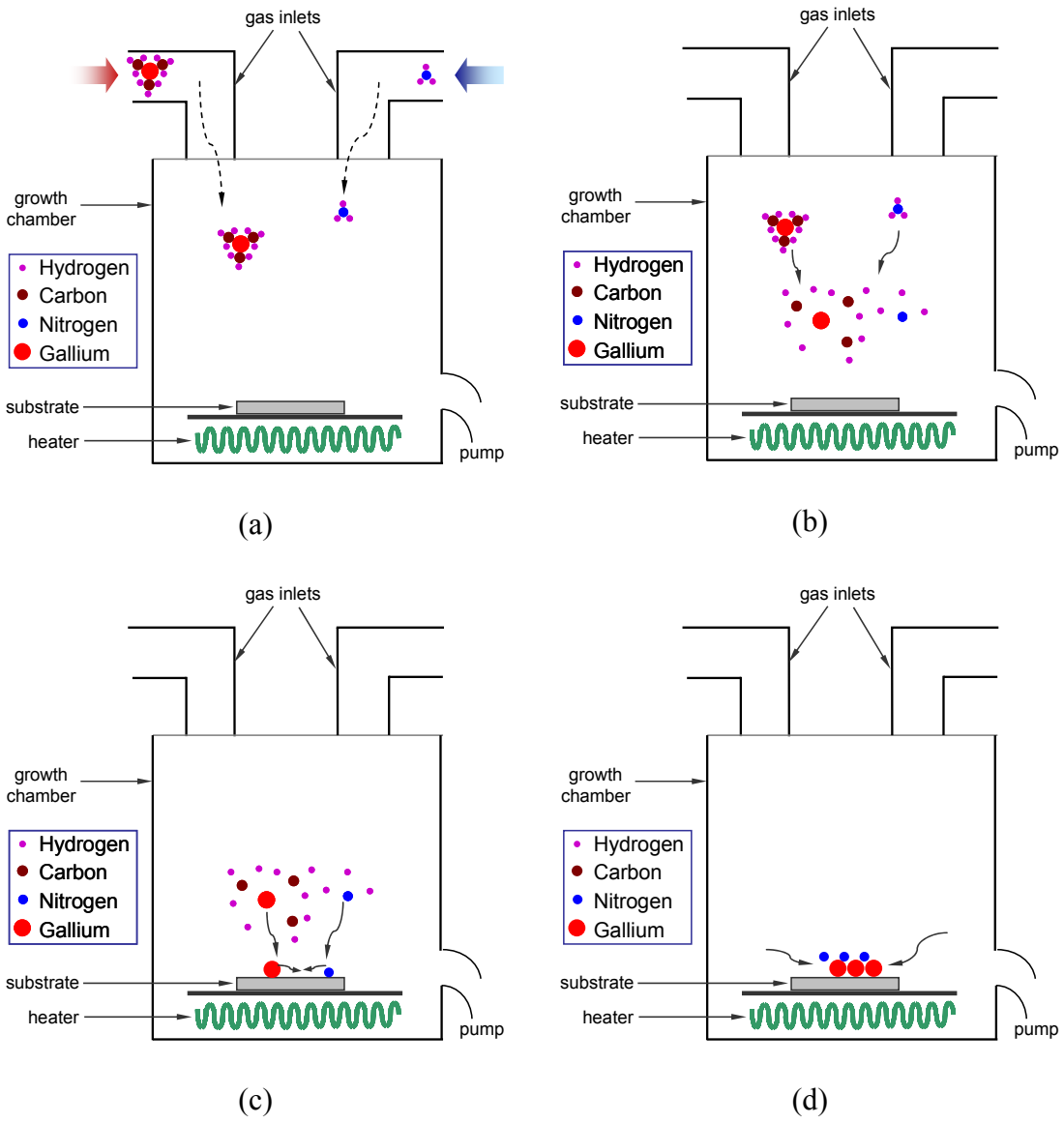

Figure 1.6: Schematic illustration of MOCVD epitaxial growth process (a) gas input (b) pyrolysis (c) diffusion (d) surface reaction.

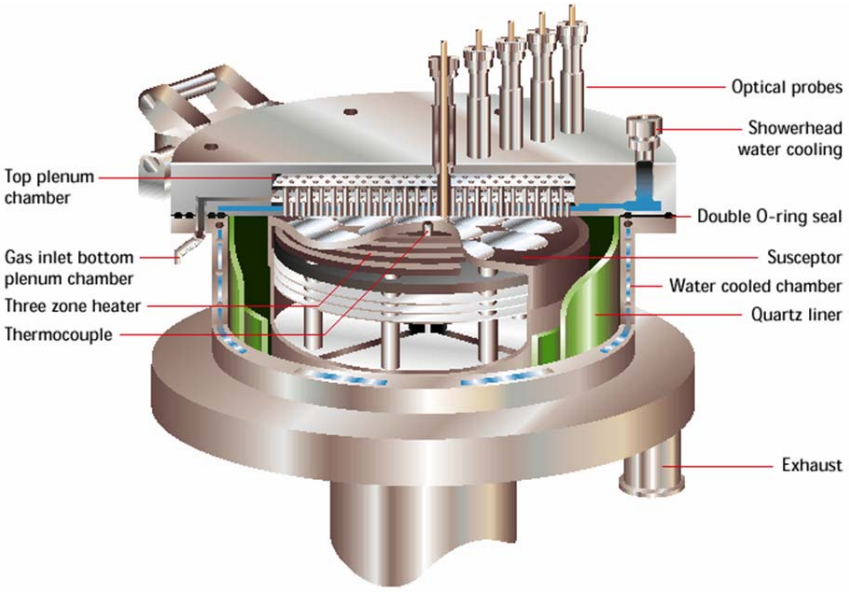

(a)

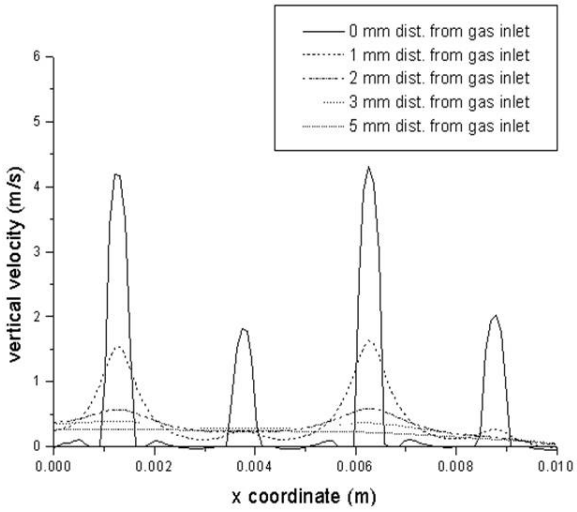

(b)

Figure 1.7: (a) Schematic illustration of MOCVD epitaxial growth chamber with closed coupled showerhead (CCS) technology manufactured by Thomas Swan Scientific Equipments (b) Vertical gas phase velocity distribution versus *x*-coordinate.[35]

1.5 Scope of This Dissertation

The purpose of this dissertation is to investigate the MOCVD growth of group III-Nitrides materials system for photodiode and electronic device applications. The research work described in this dissertation is focused on the eptixial growth and material characterization of $Al_xGa_{1-x}N$ ($0 \leq x \leq 1$). The history of the research and important aspects of group III-Nitride materials properties as well as the understanding MOCVD system employed in this study have been addressed in this chapter. Chapter 2 covers the principles of material characterization. Particular attention is given to *in-situ* reflectance, temperature, and curvature analysis tool and X-ray diffractometry because of versatility and design consideration of epitaxial growth provided by these techniques. Chapter 3 will be devoted to the complete discussion of the epitaxial growth of $Al_xGa_{1-x}N$ ($0 \leq x \leq 0$) materials system and the development of ultraviolet avalanche photodiodes. In the beginning of Chapter 4, the focus will shift to the AlN-free direct growth of GaN on SiC substrates employing AlGaN:Si conducting buffer layer. The data from *p-i-n* power rectifiers will be discussed in this chapter. Finally, this dissertation concludes with Chapter 5, a summary of results and a discussion of potential future research work.

CHAPTER 2

PRINCIPLES OF MATERIAL CHARACTERIZATIONS

2.1 Introduction

The research on semiconductor materials requires various kinds of characterization techniques for proper understanding of the material; thereby, improving performance of devices and increasing the yield. Thus, the application of a desired structural, optical and electrical characterization to each necessary step is critical. *In-situ* curvature/reflectivity analysis tool can provide the complete set of information for designing III-V heteroepitaxial growth process. The primary characterization tools employed in this study will be described.

2.2 *In-situ* Analysis Tool

The wafer size for group III-Nitride device production has recently entered into the era of 4″. It increases the urgent need for the accurate measurement of bowing and temperature because the same degree of strain can cause a much larger difference in distance between a substrate and a susceptor, resulting in larger degree of non-uniformity over a wafer; thereby, lowering the yield for useful devices. The temperature at a substrate during the epitaxial growth is one of the key parameters. It can affect such elements as composition of ternary and quaternary alloys, growth rate or doping level. Substrate temperature also has an effect on the thickness of the nucleation layer, surface roughness and the material quality of subsequently growing layers; thereby, giving a significant impact on the device performance. The temperature is also affected by the substrate bowing. Thus, careful *in-situ* monitoring and accurate control of temperature on the substrate and bowing by the proper design of epitaxial structures during the growth is indispensable.

The growth of ultraviolet (UV) avalanche photodiode (APD) structures requires multiple layers of epitaxial structures having large mismatches between substrates and epitaxial structures and between epitaxial layers, which involves strain accumulation during the growth. The accumulated strain during the growth results in the bowing of the wafers. Also, the bowing can occur during the heat up before the growth and the cooling down after the growth of the epitaxial structures mainly due to the difference in the thermal expansion coefficient and temperature gradient of top and bottom of wafers. The wafer bowing frequently accompanies defect formation such as cracks in epitaxial layers and non-uniform growth of the structures across the wafers. Therefore, *in-situ* monitoring of bowing of the wafers can provide invaluable information of thermal and mismatch induced strain, especially for the growth of deep UV APD in which large mismatch between AlN and AlGaN layers is inevitable

Generally, the temperature is monitored by either thermocouples or pyrometers; however, the thermocouples are mounted on the backside of the susceptor where they do not necessarily measure the temperature in a correct fashion. The limited thermal contact between the susceptor and the substrate along with the substrate cooling across the surface can cause inaccurate temperature measurements. In contrast to thermocouples, optical pyrometers measure the temperature directly on a growing layer or on a substrate. Hence, whenever the contact-free temperature measurement is required, the pyrometry is the method of choice.

The pyrometry is based on the fact that all bodies emit electromagnetic radiation, so-called thermal radiation, at any temperature above absolute zero; therefore, the temperature of a body can be derived from the measurement of the radiation intensity. In order to determine the temperature of a body from its incandescence intensity, the information regarding emissivity is absolutely needed; however, especially in heteroepitaxy, the emissivity is changed during the epitaxial growth. Therefore, a simultaneous measurement of the reflectivity of a sample is essential to perform an

accurate measurement. The relation between the radiation emitted by a body at a certain wavelength and its temperature is given by Planck's law. The incandescence intensity of a black body is given by the equation 2.1.

$$dP_s = \frac{2}{h^4 c^3} \frac{(\hbar\omega)^5}{e^{\hbar\omega/k_b T - 1}} d\lambda \tag{2.1}$$

where the emission from a black body is P_s.

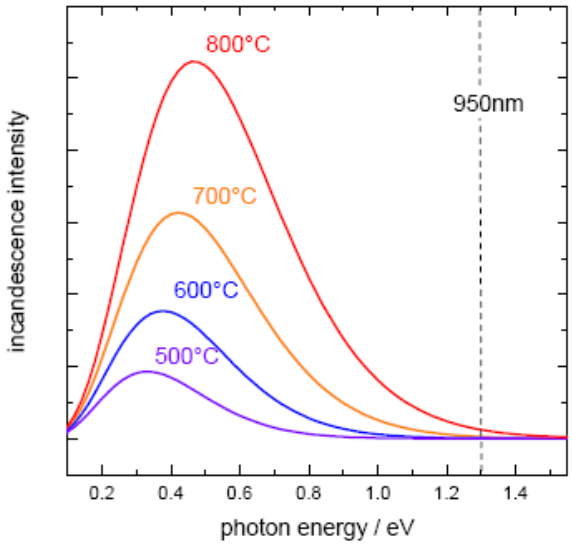

Fig. 2.1: Emission of a black body by Planck's law versus temperature.[36]

Figure 2.1 shows the emission of a black body at various temperatures ranging from 500˚C to 800˚C.[36] The thermal radiation occurs mainly from the infrared to the visible part of the electromagnetic spectrum. As the temperature rises, the emitted radiation power increases and the peak incandescence intensity is shifted towards shorter wavelengths (higher photon energy). The estimation of real temperature based on

Planck's law can introduce a large degree of inaccuracy due to the fact that a black body shows ideal behavior in its emission and absorption of radiation. It is assumed that all incoming radiation is fully absorbed independent of wavelengths. It can be explained in the same fashion as the emission of radiation. When it comes to a real body, this has never been the case. The difference between the emission from a real body (P) and that from a black body (P_s) can be described by the emissivity in the equation 2.2

$$\varepsilon(\lambda, T) = \frac{P}{P_s} \tag{2.2}$$

ε(λ,T) gives the ratio of the emitted radiation with respect to that from a black body; thus, Planck´s law needs to corrected by the emissivity in order to estimate the emission of a real body as shown in the equation 2.3

$$dP = \varepsilon \cdot dP_s = \varepsilon \cdot \frac{2}{h^4 c^3} \frac{(\hbar\omega)^5}{e^{\hbar\omega / k_b T - 1}} d\lambda \tag{2.3}$$

Another fact that must be taken into account is that the absorption and emission of radiation at different wavelengths is affected by the optical properties of growing materials as well as the surface roughness. In order to derive the temperature of a sample by measuring its incandescence intensity, the emissivity must be measured as accurately as possible; however, the emissivity is often changed during the epitaxial growth due to the change in the band gap depending on the temperature. Also, the measured intensity may be affected by optical properties such as substrate properties or refractive index during the heteroepitaxy. Furthermore, the thermal radiation experiences reflections at the interfaces between different epitaxial layers or a layer and a substrate. It can lead to constructive and destructive interferences, resulting in significant oscillations of the

emitted intensity, depending on the thickness of the growing layer as shown in Figure 2.2. This leads to non-existing change in temperature while this reflectance measurement is still used to estimate the growth rate.

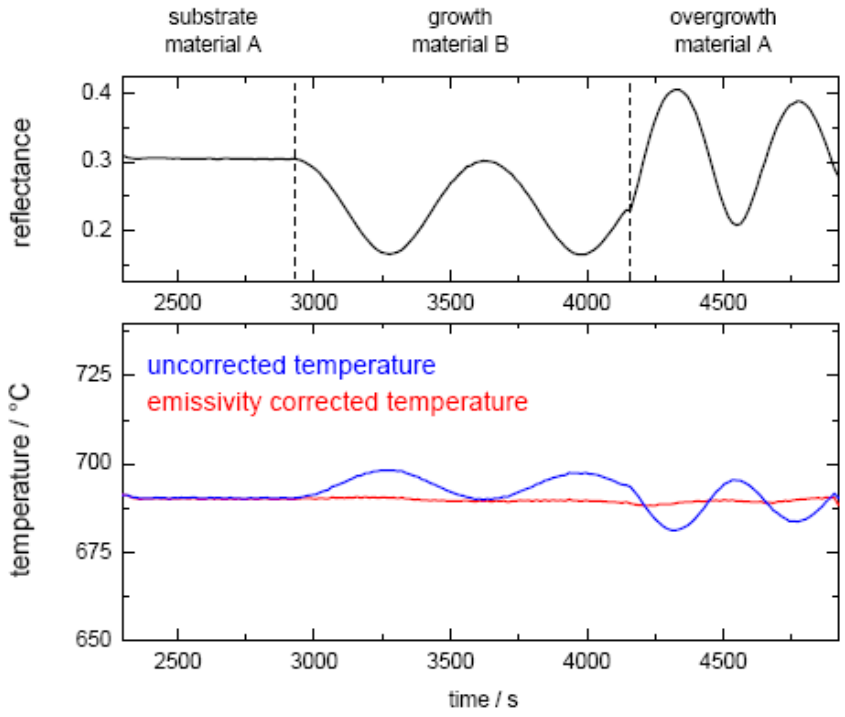

Fig. 2.2: True temperature measurement during heteroepitaxy.[36]

The reflectance measurement at the same wavelength as pyrometry is necessary to determine the actual emissivity of the substrate during the epitaxy. The substrate is illuminated and the intensity of the reflected light from the substrate is measured. The summation of absorbed (α), reflected (R), and transmitted (t) radiation should be equal to the intensity of incident light shown in the equation 2.3.

$$\alpha + R + t = 1 \tag{2.3}$$

For opaque substrates, such as the one-side polished sapphire substrate, the transmission through a substrate can be neglected. In this case, the following equation can be established.

$$\alpha + R = 1 \tag{2.4}$$

The emissivity can be derived from the reflectance measurement based on Kirchhoff's law in the equation 2.5.

$$\alpha(\lambda, T) = \varepsilon(\lambda, T) \tag{2.5}$$

The absorption is equal to the emissivity of a body and the true temperature can be determined by applying Planck's law. The interference effect during the epitaxy leads to oscillations in the reflectance, resulting in oscillations in the emissivity. *In-situ* reflectance measurement can be used to determine reflected radiation (R) at the substrate in the equation 2.6

$$\varepsilon = 1 - R \tag{2.6}$$

Thus, the emissivity corrected pyrometry can be performed as shown in Figure 2.3.

It becomes more difficult to perform an accurate temperature measurement if a transparent substrate such as SiC or both-side polished sapphire is used. In this case, the pyrometer does not measure the temperature of the substrate and it is also affected by the underlying susceptor as shown in Figure 2.4. The substrate temperature can be corrected by ΔT between the substrate and the susceptor in the equation 2.7.

$$T_{substrate} = T_{susceptor} + \Delta T_{substrate/susceptor} \tag{2.7}$$

This calibration can be carried out using the eutectic point measurement using Al-Si substrate. The true temperature measurement system manufactured by LayTec, GmbH. is schematically shown in Figure 2.5

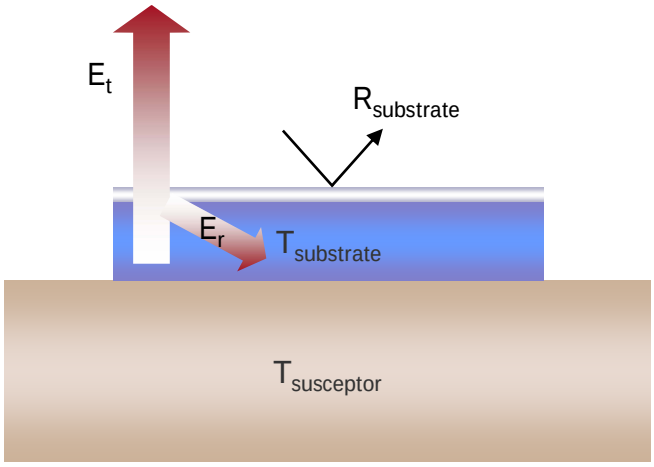

Fig. 2.3: Emissivity correctred pyrometry of tranaparent layers on an absorbing substrate.

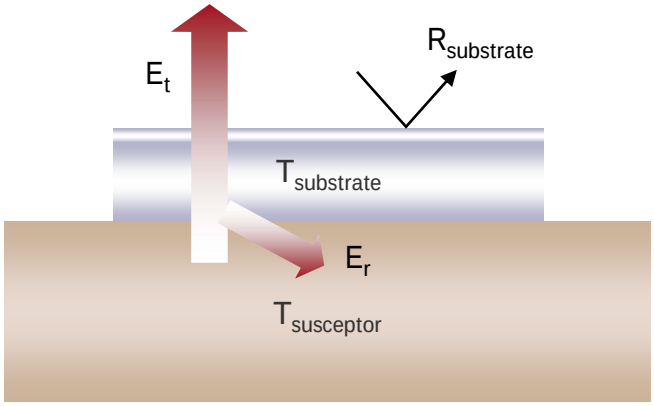

Fig. 2.4: Temperature measurement of transparent layers on a transparent substrate.

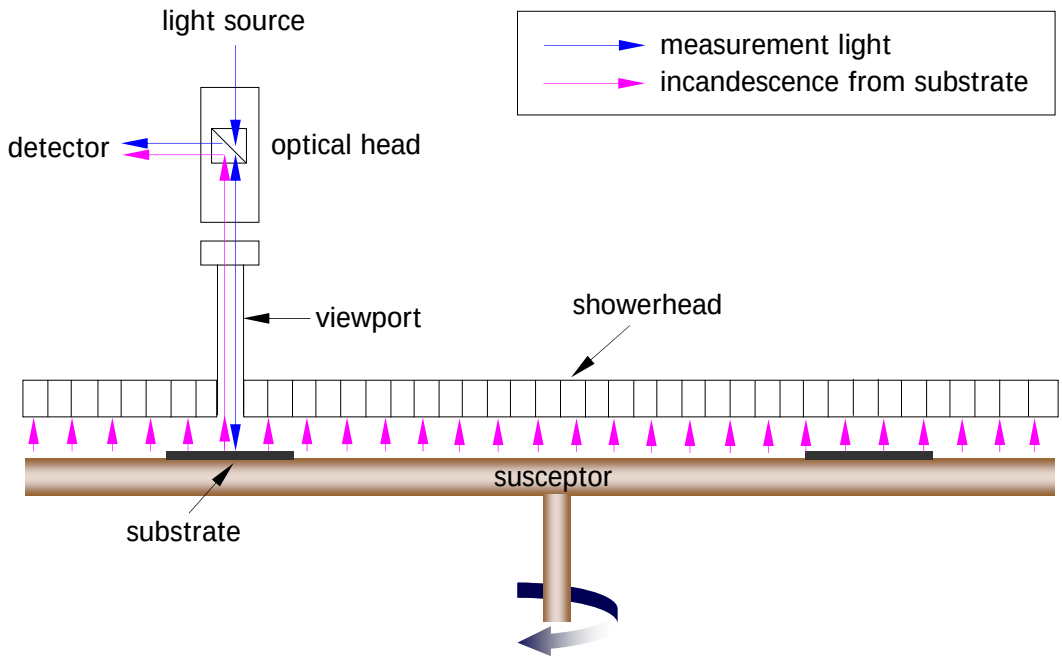

Fig. 2.5: *In-situ* true temperature measurement system.

The optical sensors have gained much attention in the past few years and demonstrated their outstanding suitability in performing *in-situ* measurements. *In-situ* reflectance measurement gives direct access to the growing layers and it can be implemented through a normal incidence viewport as shown in Figure 2.5. The information obtained during *in-situ* reflectance measurement can provide detailed analysis such as growth rate, layer composition or surface roughness. It can also be used in the emissivity correction of pyrometer for an accurate measurement of the true temperature. The light of a chosen wavelength is impinging onto the layer of interest. The intensity of the partly reflected light is measured by a photo diode or a CCD array. The intensity of reflected light source is called reflectance (R), for a single interface between vacuum and a bulk material with refractive index n and extinction index k. It is given by the equation 2.7.

$$R = \frac{I_{reflected}}{I_{incident}} = (n-1)^2 + \frac{k^2}{(n+1)^2} + k^2 \qquad (2.7)$$

The refractive index n and the extinction index k show dispersion. They depend on the wavelength of the incoming light and also change with the composition of the layers and with the actual substrate temperature. The intensity of reflected light is measured at a single wavelength as a function of time. If a growing layer is transparent at the wavelength of the incoming light, these transients show an intensity-modulation related to the interference effect; thus, the periodicity of the modulation can be used to determine the thickness and growth rate of the layer. Part of the incoming light can be reflected at the growing surface while the remaining part can be penetrated into the layer and partly reflected back at the interface between the substrate and the bottom of the layer. The overall intensity of the reflected light is determined by superposition of all of the reflected beams. The constructive and destructive interference will occur due to the phase difference among reflected beams. It will introduce the intensity modulation of the reflected light, so-called Fabry-Pérot oscillations.

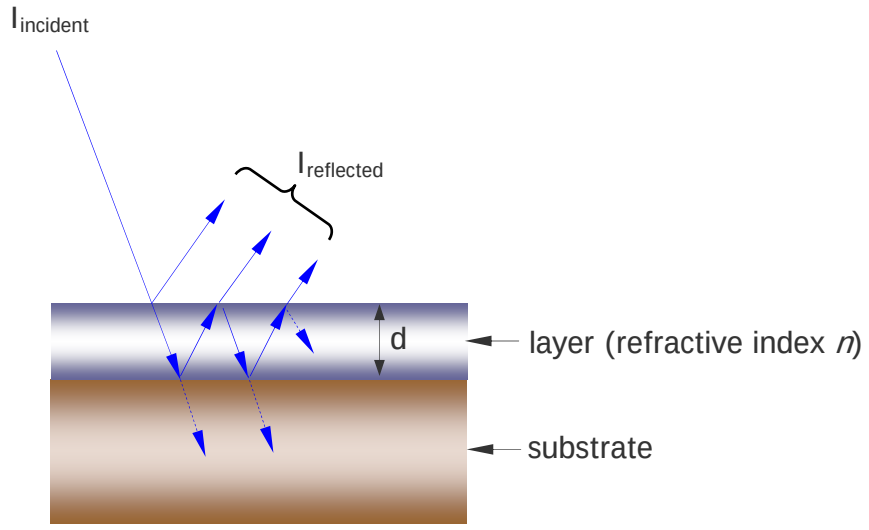

Fig. 2.6: Reflection of incoming light at a growing layer on an absorbing substrate.

The phase difference and the intensity of the reflected light at the surface depend on the thickness of the growing layer and optical properties of the materials as well as the wavelength of the light. In the case of constructive interference, the maximum intensity (peak) of reflectance will occur when the path difference between two beams is equal as described in equation 2.8. For destructive interference, the minimum intensity (valley) of reflectance will be obtained when two beams show the difference of an odd number of the half wavelength of incident light as shown in the equation 2.9.

$$2nd = m\lambda \tag{2.8}$$

$$2nd = (m + \frac{1}{2})\lambda \tag{2.9}$$

here n is the refractive index of a material, d is the thickness of growing layer, and m is an even number.

Hence, the thickness of the epitaxial layer can be derived by measuring Fabry-Pérot oscillations.

The intensity of reflectance measurements can be affected by the properties of growing layers as well as growth conditions. The influence of surface quality on the intensity of reflected light can appear as ideal growth behavior, i.e. constant intensity of maxima and minima. The amplitude of intensity modulations will be decreased if a growing layer absorbs a wavelength of incoming light whose k_{layer} is not zero. The increase in surface roughness during the epitaxy can be seen as the decrease in both maxima and minima of reflectance. The increase in layer-substrate bowing or local fluctuations can be seen as the decrease in maxima and the increase in minima of reflectance, i.e. damping. Figure 2.7 summarizes each case during the epitaxy.

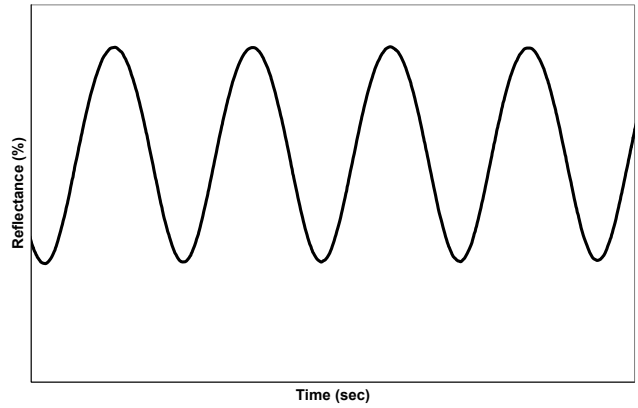

(a)

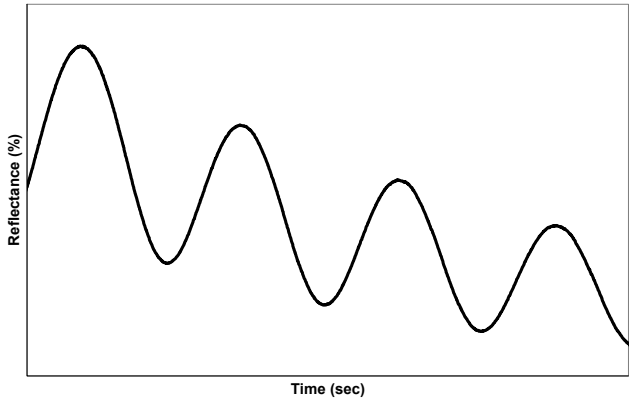

(b)

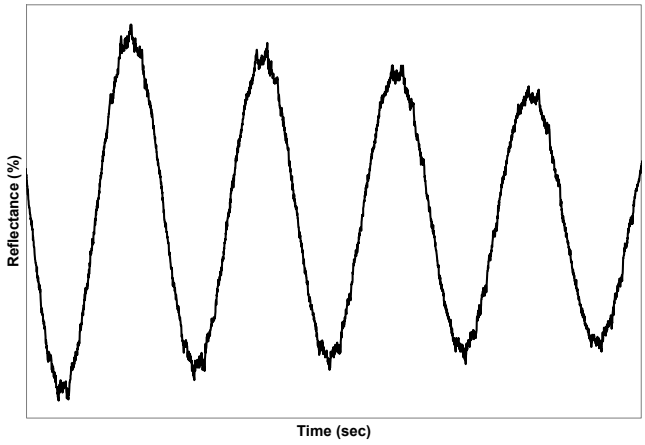

(c)

Fig. 2.7: Influence of surface quality on the intensity of reflected light: (a) ideal growth (b) roughness increase (c) damping.

The bowing occurs due to a temperature difference between the topside of a substrate and backside of a substrate during the heat-up, high-temperature growth, and cool-down. Figure 2.8 shows the schematic drawing of LayTec's EpiCurve® TT system. *In-situ* curvature measurement EpiCurve TT is based on the following relation: the laser spot distance (ΔX_D) is linearly proportional to the bowing ($1/R_C$). The group III-nitride heteroepitaxy on non-lattice matched substrate causes strain build-up to the laser-substrate-system. The curvature on the growing epitaxial layer can be described in equation 2.10.

$$\frac{1}{R_C} \cong -\frac{(\Delta X_D - \Delta x_o)}{2\Delta x_o Z_D} \tag{2.10}$$

The resolution increases with the initial laser spot distance (Δx_o) and the distance between the substrate and the detector (Z_D). The convex bowing is seen as negative in km^{-1} and the concave bowing is appeared as positive in km^{-1}. The relation is schematically drawn in Figure 2.9. The *in-situ* curvature measurement combined with the reflectance measurement and true-temperature measurement provides the full-set of information needed for group III-nitride heteroepitaxy. LayTec's EpiCurve TT system offers the following features.

- Control of curvature
- Wide band pyrometry at 950 nm for temperature control
- Wide band reflectometry at 950 nm for emissivity correction
- Single wavelength reflectometry at 633 nm or 950 nm depending on the material system
- Monitoring of Surface morphology evolution

- *In-situ* monitoring synchronized with wafer rotation
- Individual wafer monitoring
- Complete measurement on each wafer and non-wafer area on a susceptor
- Adjustable probing area depending on a substrate and interest
- User-definable separate area measurement on a single wafer
- Monitoring of etching back effect
- Hardware interface to epitaxial growth system
- High-temperature database of substrate and optical properties of materials
- Built-in software algorithm for growth rate simulation

By incorporating EpiCurve TT system into the epitaxial growth, parameters such as wafer curvature, growth temperature, reflectance, refractive index, absorption coefficient, growth rate, layer thickness, or layer composition can be obtained.

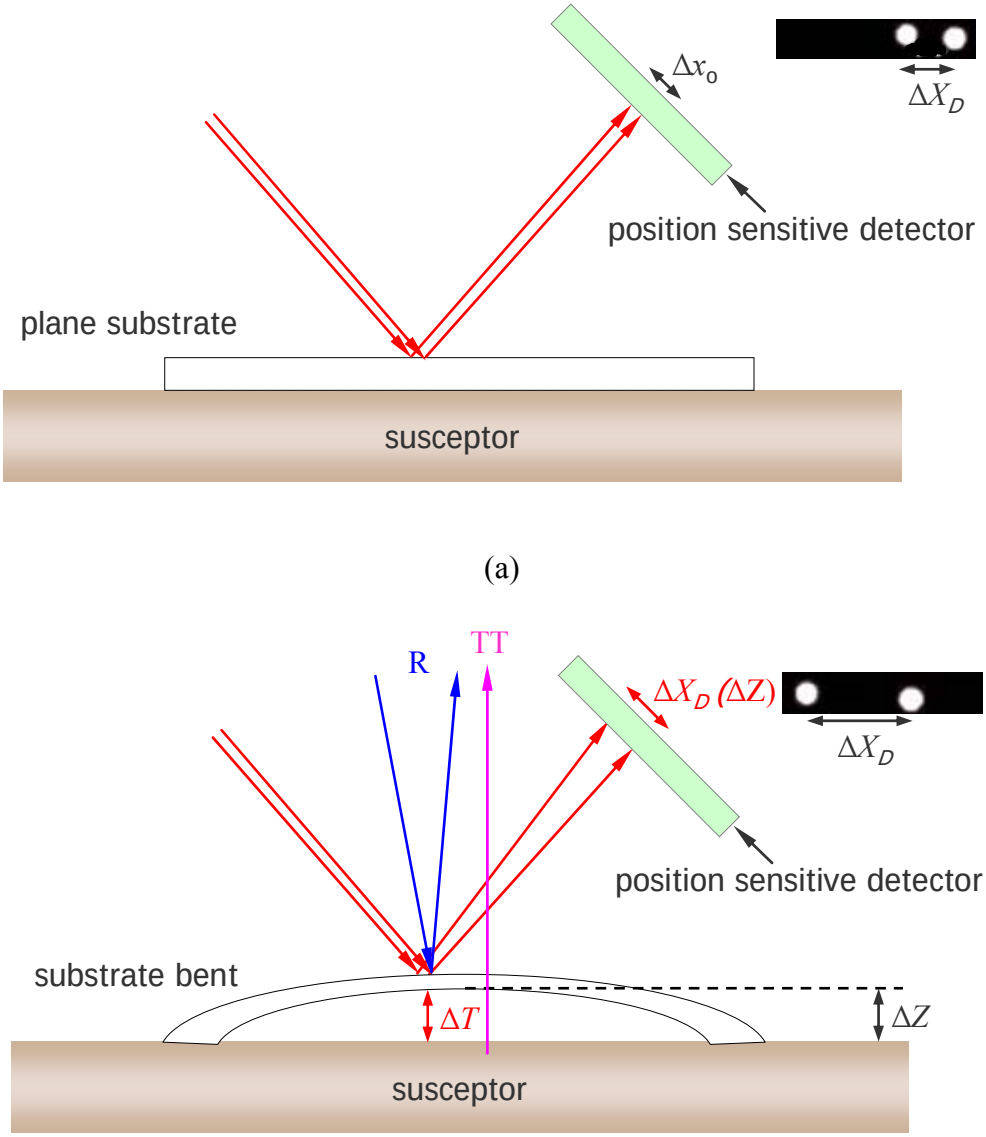

Fig. 2.8: Schematic drawing of LayTec's EpiCurve® TT system showing distance variation between two beams: (a) plane substrate at room temperature (b) substrate bent at high temperature growth due to the strain.

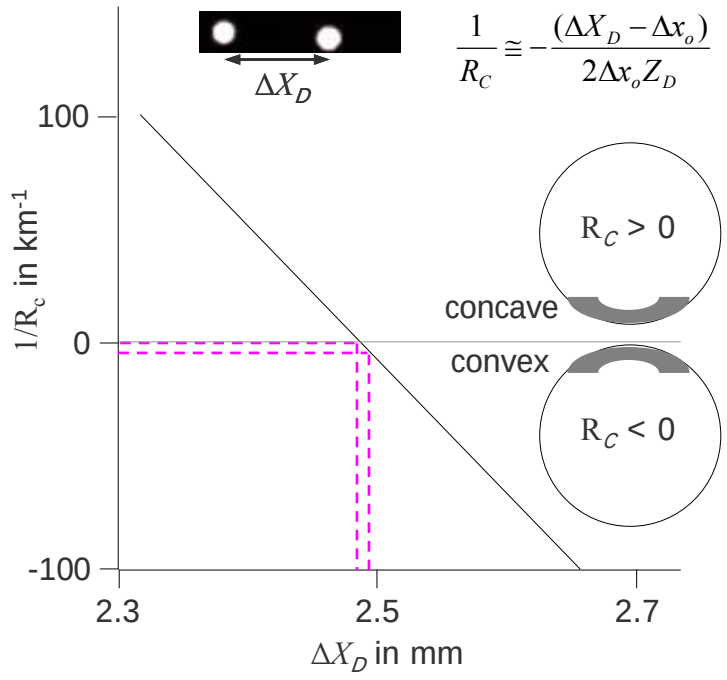

Fig. 2.9: Relation between laser spot distance (ΔX_D) and substrate bowing ($1/R_C$).

2.3 X-Ray Diffractometry

X-ray diffractometry (XRD) is an extremely powerful *ex-situ* structural characterization technique for all crystalline material systems due to the periodic nature of crystal. The convenient and non-destructive characterization makes the determination of layer parameters such as alloy composition, uniformity of epitaxial layers, thickness, built-in strain and strain relaxation, and crystalline perfection related to the dislocation density possible.[37, 38] In addition to *in-situ* analysis tool, XRD makes it possible to correlate the structural properties of materials to the design of epitaxial growth processes. The reciprocal space is basically a three-dimensional Fourier transform of the real space periodicity. Just as other diffraction techniques, XRD probes the reciprocal space periodicity. Consequently, if a perfect crystal structure is given by three-dimensional δ-functions, each reciprocal space point should have zero spread with infinite height, but as for the real crystal structures, these peaks are broadened due to the presence of defects such as dislocations or stacking faults. Thus, the broadness in a peak, called "full-width at half-maxima" (FWHM), can be used as a good indicator of the material quality.

All of the XRD data presented in this dissertation are taken using Philips X'Pert® MRD (Material Research Diffractometer) high-resolution (0.0001°) X-ray diffractometer. For X-ray rocking curve and reciprocal space mapping setup, point source of X-ray (characteristic Cu $K_{\alpha 1}$ and $K_{\alpha 2}$ radiation: λ=1.5405 and 1.5443 Å, respectively) is collimated and monochromated by a four-crystal (i.e., four reflections) Ge (220) monochromator (Bartels monochromator [39]) to achieve high angular resolution. The four-crystal monochromator is the key element for higher angular-resolution diffraction measurements relative to a normal double-crystal diffractometer. The Monochromated and collimated primary X-ray beam (λ = 1.5405 Å) ($\mathbf{k_0}$) is diffracted from a particular set of planes of the sample and then the diffracted beam ($\mathbf{k}$) is detected by either one of

detector positions. Figure 2.10 shows a schematic drawing of the Philips X'Pert MRD X-ray diffractometer. The diffractometer features a high-slew-rate, high-accuracy goniometer with 0.0001° step resolution for the sample cradle. The sample cradle can be translated along the *x*-axis, *y*-axis, and *z*-axis (sample height). It can also be rotated along the ω-axis (θ-axis, sample rocking), ϕ-axis (sample rotation), and ψ-axis (sample tilt). The detector and the sample cradle can be rotated about the rocking axis independently or coupled with each other at the same offset angle. The X'Pert MRD includes a secondary optics assembly: detector 2 for the X-ray rocking curve and detector 1 with an analyzer crystal for the reciprocal space mapping (RSM). The analyzer crystal section makes use of a Ge (110) channel-cut crystal that is aligned to the (220) reflection.

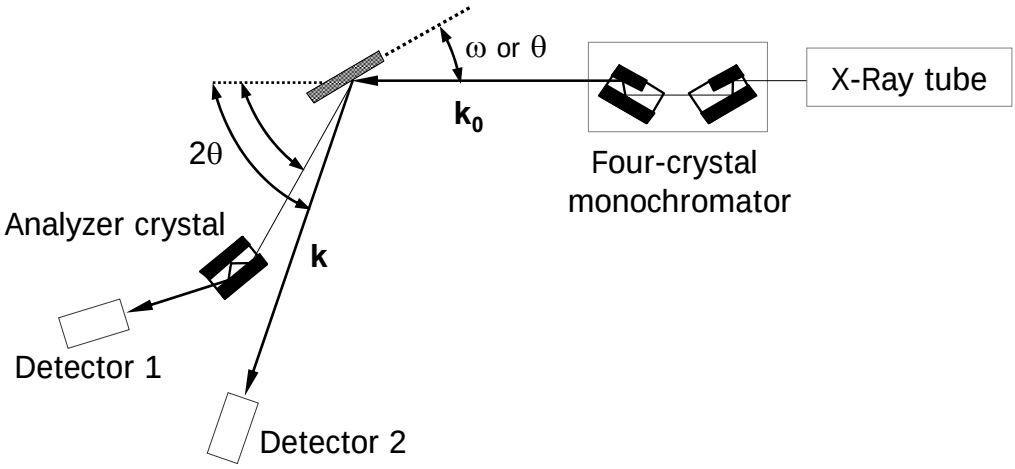

Fig. 2.10: Schematic top-down view of X-ray diffractometer.

Lattice planes in three-axis (*a*, *b*, and *c*) crystals are indexed by Miller indices (*h k l*). (*h k l*) indicates the first plane in the family from the origin intercepting *a/h*, *b/k*, and *c/l* on the axes. Bragg's law in equation 2.11 describes the diffraction of x-rays by different crystallographic planes in a crystal.

$$n\lambda = 2d_{hkl} \sin\theta_B \tag{2.11}$$

In equation 2.11, n is the diffraction order as an integer, λ is the X-ray wavelength, d_{hkl} is the spacing between adjacent crystallographic planes, and θ_B is the Bragg angle of incidence and diffraction to the plane. The incident beam and diffracted beam are always coplanar; therefore, the angle between the diffracted beam and transmitted beam is always 2θ. For most crystals, d_{hkl} is ~ 3 Å. The diffracted beams will have the destructive interference if Bragg's Law is not satisfied. If the beam path of $AB+CD$ is a multiple of X-Ray wavelength λ, two waves will give the constructive interference. It is schematically illustrated in Figure 2.11

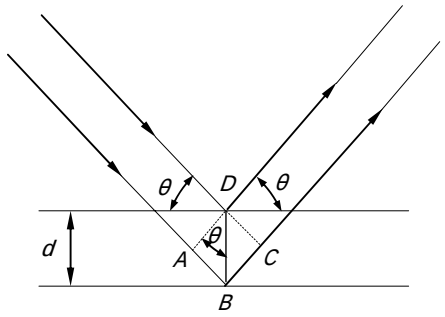

Fig. 2.11: Schematic illustration of Bragg's diffraction condition.

The parameter d_{hkl} is defined differently for each Bravais lattice because of the different relationships among the crystallographic axes. The lattice spacing of plane (*h k l*) for a cubic crystal ($a = b = c$) is described by equation 2.12.

$$\frac{1}{d_{hkl}^2} = \frac{h^2 + k^2 + l^2}{a^2} \tag{2.12}$$

The d_{hkl} for a hexagonal Bravais lattice is described by the equation 2.13.[40]

$$\frac{1}{d_{hkl}^{\ 2}} = \frac{4}{3}\left(\frac{h^2 + hk + k^2}{a^2}\right) + \frac{l^2}{c^2} \tag{2.13}$$

Equations 2.11 and 2.12 (or 2.13) provide correlations between specific planes and Bragg angles for the wavelength of X-Ray λ. Thus, for a symmetric plane i.e. (*0 0 l*), the *c*-axis of a hexagonal crystal can be determined from a single symmetric scan using the two equations (2.11 and 2.13) described the above.

One of the most frequently employed XRD scans to analyze epitaxial layers is a rocking curve (ω-scan). In this geometry, the detector is kept at a fixed angle with respect to the primary beam (2θ) while the sample is rocked or rotated with respect to the axis perpendicular to the schematic diagram shown in Figure 2.10. Symmetric rocking curves are commonly used to determine the *c*-lattice constants of relatively lattice-matched materials; however, in this configuration, the detector is not moved along with the sample, resulting in only a small angular probing range of approximately 1°. In the case of the group III-Nitrides grown on non-lattice matched substrates such as sapphire, Bragg angles for epitaxial layers are much smaller than that of the substrate so that a rocking curve cannot provide the non-lattice matched information between the epitaxial layers and the substrate. For group III-Nitrides, large degrees of mismatch exist;

therefore, rocking curve (ω-scan) can be used to determine the relative crystalline quality among samples. On the other hand, an asymmetric rocking curve on a plane such as ($1\ 0\ \bar{1}\ 2$) or ($1\ 0\ \bar{1}\ 4$) can provide more information because the full-width half-maximum (FWHM) of these peaks are sensitive to threading dislocations.

The other technique for the characterization of highly mismatched layers is the ω-2θ scan. In this diffraction condition, the detector moves at twice the angular rotation rate of the sample (ω) so that the measured diffraction angle remains equal to the incident beam angle. The angular spread of the diffracted beam is not measured; therefore, the diffraction peaks are narrower and do not overlap as much as in the ω scan.

A two-dimensional mapping of reciprocal lattice is obtained through the combining a ω-2θ scan with ω-scan along reciprocal lattice points as shown in Figure 2.12. This technique is called reciprocal space map (RSM) and is particularly useful in determining the strain condition in epitaxial heterostructures. An asymmetric RSM is a direct measurement technique that does not require any assumptions about the strain condition in the material in order to calculate composition, while a symmetric RSM contains information about the crystalline quality of epitaxial films.

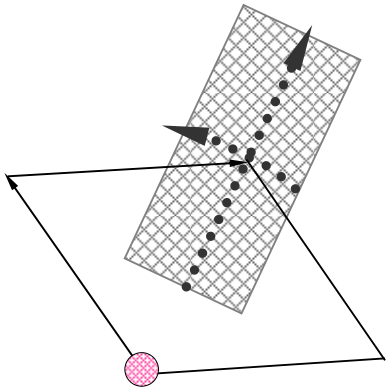

(a)

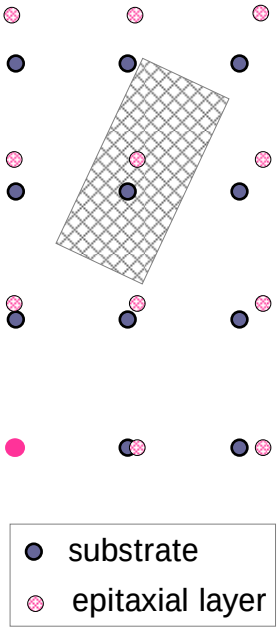

(b)

Fig. 2.12: (a) Schematic illustration of ω-2θ scan and ω-scan along reciprocal lattice points for RSM (b) RSM schematic illustration for epitaxial layer with smaller lattice constant than that of substrate.

2.4 Atomic Force Microscopy

Atomic force microscopy (AFM) invented by Binning, Quate, and Gerber in 1986 employs a microscopic probe tip (non-conductive Si tip in this study) to probe surface features of an epitaxial layer of interest in a raster scan. The important performance parameters for AFM tips are the aspect ratio, the radius of the curvature, the opening angle, the overall geometrical shape, and the tip material. Certain probe tip manufactures utilize a carbon nanotube structure onto AFM tips for the enhancement of resolution and durability. AFM is a very useful non-destructive measurement technique to determine the overall surface smoothness or features in the three-dimensional platform, growth mode during the epitaxy, and defect density, but it requires relatively longer time for analysis. Basically, the surface morphology is generated by plotting the force to track the surface features with equal distance between the probe tip and the layer surface. In detail, the tip is mounted at the end of a cantilever, bending in response to the force between the tip and the sample. As the cantilever flexes, the light from a laser is reflected onto the photodetector. Changes in the bending of the cantilever can be measured by evaluating the difference between the incoming signal and the reflected signal. The AFM tool used to analyze surface morphology of samples in this dissertation was a Veeco Dimension 3100® with the Olympus AC160® tip with resonant frequency of 300 KHz and spring constant of 42 N/m. Contact mode or tapping mode is the method of choice for surface profiling; however, if the surface of a sample is not smooth enough, the oscillation amplitude of a cantilever cannot track the features on the actual surface instantaneously. In addition, the contact mode is generally recommended for small area scans, for example 1×1 μm^2, because of the friction between the tip and the surface. Hence, all of the measurements were carried out in a tapping mode. In addition to these, torsional resonance (TR) [41] mode is also available for certain AFMs. The TR mode measures and controls dynamic lateral forces between the probe tip and the sample surface. With the aid of the advanced sensing hardware and electronics to characterize torsional

oscillations of the cantilever, the TR mode enables a detailed examination of in-plane anisotropy. Also, it can provide new perspectives in the study of structures and properties of group III-V materials. The operation of tapping mode is illustrated in Figure 2.13 [41] and a schematic drawing of an AFM is shown in Figure 2.14.

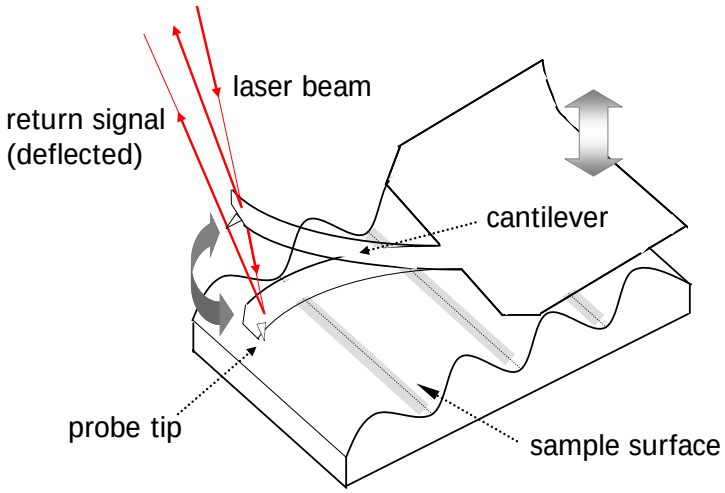

Fig. 2.13: Schematic illustration for tapping mode operation of AFM.

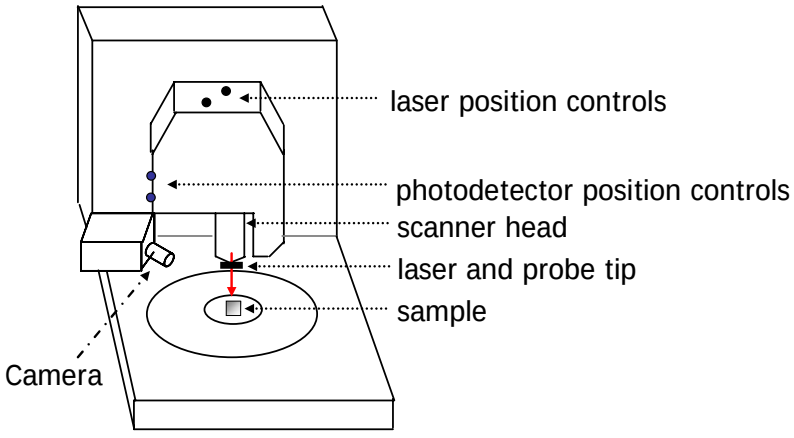

Fig. 2.14: Geometric configuration of AFM.

2.5 Nomarski Optical Microscopy

As-grown sample generally goes through the inspection process by Nomarski optical microscopy after the material growth is completed. The smooth surface does not necessarily guarantee the desired characteristics of epitaxial layers; thereby, having high performance of the devices. However, the rough surface features on as-grown surface are the indication of wrongfully chosen growth parameters or other issues with preparation or growth process. For example, hexagonal pits on GaN or AlN surface are generally the indication of low growth temperature and hill-locks on GaN surface suggest a three-dimensional enhanced growth mode rather than two-dimensional growth mode. In case of AlGaN on GaN, the strain relaxation can be seen as cracks on the surface. Nomarski employs a differential interference contrast (DIC) technique; thus, it provides excellent sensitivity for the observation of surface roughness. The optical microscope resolution (d) is given by Abbe's law in equation (2.14).[42]

$$d = \frac{0.612\lambda}{n\sin\alpha} \tag{2.14}$$

Here λ is the wavelength used to illuminate an object, n is a refraction index of the medium through which λ travels, and α is an aperture angle. The maximum resolution that can be achieved using blue-green light ($\lambda \sim 400$ nm) incorporated into the Nomarksi optical microscope used in this dissertation is approximately 200 nm.

2.6 Scanning Electron Microscopy

Scanning electron microscopy (SEM) is commonly used to view the surface features or cross-sections of as-grown samples or fabricated devices. SEM offers several advantages over other microscopy such as optical microscope or transmission electron microscope (TEM) due to its high resolution with relatively short, simple preparation step.[43] Electrons accelerated to a high kinetic energy up to 35 KeV are used as a radiation source. The wavelength of accelerated electrons (λ in nm) is based on relativistic theory shown in equation 2.15.

$$\lambda = \frac{h}{\sqrt{2m_e eV}\sqrt{1+\frac{eV}{2m_e c^2}}} \tag{2.15}$$

Here h is Planck constant (4.136×10^{-15} eV·s), c is the speed of light in vacuum (2.998×10^{-1} nm/s), e is the electron charge (1.602×10^{-19} C), V is potential difference [V], and m_e is the electron mass (9.109×10^{-28} g). It enables high resolution down to a few nanometer scale. The schematic illustration of SEM is shown in Figure 2.15. [44]

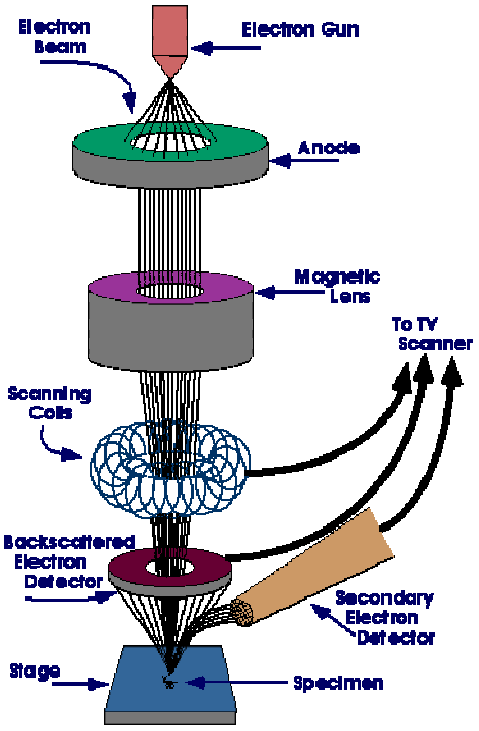

Fig. 2.15: Schematic illustration of a SEM column.[44]

2.7 Secondary Ion Mass Spectroscopy

Secondary ion mass spectrometry (SIMS) is an analytical characterization technique which detects very low concentrations of atoms such as impurities or dopants with respect to the primary elements of the material of interest. It can provide a wide range of elemental depth profiles from a few angstroms to tens of microns. SIMS works by sputtering the sample surface slowly with focused primary ion beams, producing the physical damage. The ejected secondary ions are extracted and analyzed using a mass spectroscopy system. In SIMS, if an ejected atom is not charged, it cannot be analyzed in a mass spectrometer. The number of ions ejected per incident primary ion is called the secondary ion yield. It can be plotted against the sputtering time; however, this can be meaningful when the secondary ion yield is scaled to a unit of atomic concentration in

comparison with previous calibration runs using ion-implanted samples and the sputtering time is scaled to a unit of depth by scaling with the depth of the hole formed when the sputtering is completed. One of the limitations often observed during SIMS is a high concentration of any elements abundant in nature, such as carbon, nitrogen, or oxygen at the surface, showing gradual decrease into the material by implantation of these species by the primary ions. SIMS data presented in this dissertation were gathered by Evans Analytical Group.

2.8 UV-Visible Photospectrometry

The optical transmittance measurement is a characterization technique which can be used to determine the absorption wavelength, the opacity, and the alloy composition of as-grown epitaxial layers on a wider-bandgap substrate. Photons lose their energy as they excite electrons from the valence band to the conduction band. Photons directed toward a surface of as-grown epitaxial layers have a very high probability of being absorbed if their energy is greater than the bandgap energy of the sample. Otherwise, photons are transmitted through the epitaxial layers. The bandgap energy can be calculated from basic information and the alloy composition for ternary nitride materials can also be determined. Details regarding the determination of bandgap energy and alloy composition can be found in the following literature.[45,46,47,48,49]

As mentioned, the optical transmittance measurement can provide the bandgap information. The broad transmittance cut-off essentially means that the material absorbs below band gap, which indicates that the energy band diagram of a material has states in-between the two band-edges. There is a conduction band edge and a valence band edge; nevertheless, an electron cannot have an eigenstate with energy in-between based on a band theory. As a result, the minimum energy of absorption has to be the bandgap

energy; however, defects and impurities can change the Hamiltonian so that there can be solutions to the Schrodinger's equation with energy eigenvalues, creating new energy states in between two bands. Thus, there can be absorptions below the bandgap energy. If a material has a small number of defects, the optical transmittance spectra will show sinusoidal oscillations for wavelengths below the bandgap and a sharp decay at the bandgap energy as compared to the case of broad transmittance cut-off in Figure 2.16. The oscillations are due to microcavity effect, which occurs when an epitaxial layer creates a very small cavity; therefore, in the case of thicker epitaxial layer, the sinusoidal part is seen to have more oscillations than that of thinner layer. With the substrate (generally too thick with respect to epitaxial layers), the cavity becomes too large so that positions of the maxima and minima of oscillations become too close, which cannot be detected.

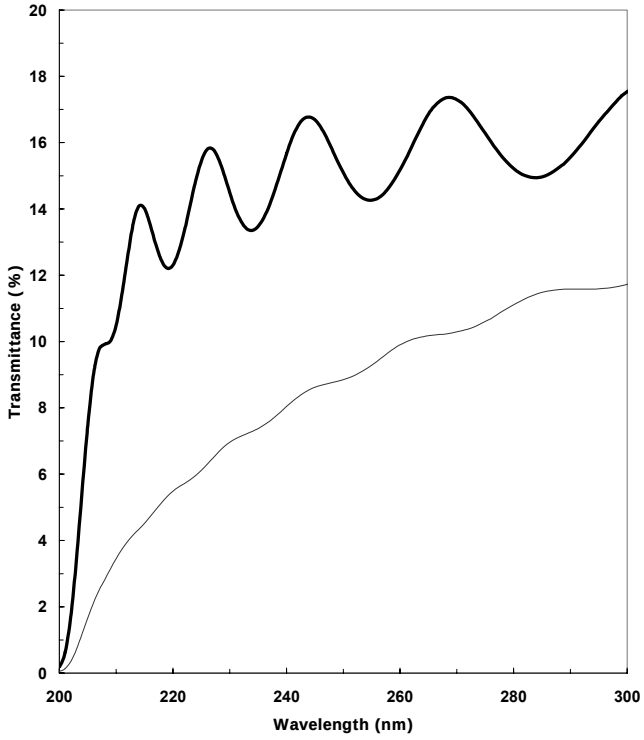

Fig. 2.16: Examples of optical transmittance spectra showing broad cut-off versus sharp decay at the bandgap energy.

2.9 Photoluminescence Measurement

Photoluminescence (PL) refers to the measurement of the spontaneous emission spectrum of a direct bandgap semiconductor material that is being excited by a laser. The photon energy of the incident laser beam must be high enough to generate electron-hole pairs across the bandgap of the material being characterized. The electrons and holes go through either a radiative or non-radiative recombination process. When the photons via radiative recombination are measured as a function of wavelength, the data can be used to determine the bandgap of a semiconductor. Also, it can provide information regarding defect states within the bandgap. A direct bandgap energy material that can be analyzed by a certain wavelength of laser is described by equation 2.16

$$E_g = \frac{hc}{\lambda} = \frac{1249.8}{\lambda} \tag{2.16}$$

In this equation, E_g is the bandgap energy of a material in eV and λ is the wavelength of a laser in nm. The 266 nm Q-switched Nd:YAG laser in the Accent Optical Technologies RPM-2000 system used for the study is capable of measuring photoluminescence characteristics of a semiconductor material up to 4.698 eV.

2.10 Hall-Effect Measurement

Hall-effect measurement is a simple characterization technique which can be used to determine the Hall mobility and concentration of the majority carrier in epitaxial layers grown on non-conductive substrates. It can be accurately applied to the case when only one epitaxial layer is intentionally doped and the layer thickness is known. The basic physical principle underlying the Hall-Effect is Lorentz force given by equation 2.17.

$$\vec{F} = q\left(\vec{E} + \vec{v} \times \vec{B}\right) \tag{2.17}$$

Here $\vec{E}$ is electric field, $\vec{v}$ is velocity of carrier, and $\vec{B}$ is magnetic field. As an electron moves along the direction perpendicular to an applied magnetic field, it experiences a force acting normal to the direction of a magnetic field and moves in response to this force and the force applied by the internal electric field. If a constant current flows along the one direction (*x*-direction) in the presence of a magnetic field parallel to *z*-direction, electrons subjected to Lorentz force drift away from the direction of the current flow (in the *y*-direction), resulting in the excess charge on one side of the sample. This excess charge is the source of the Hall voltage (V_H). For *n*-type material, the sheet carrier concentration (n_s) can be obtained by measuring the Hall voltage as shown in equation 2.18.

$$n_s = \frac{I\vec{B}}{q|V_H|} \tag{2.18}$$

As shown in the equation 2.19, the sheet resistance (R_S) can also be determined by use of the van der Pauw resistivity measurement technique. [50]

$$R_S = \frac{|V_H|}{\mu I\vec{B}} = \frac{1}{n_s q\mu} \tag{2.19}$$

The variable-temperature Hall-Effect measurement provides the information about the activation energy of dopant in an epitaxial layer or the bandgap of the epitaxial layer.

2.11 Resistivity Mapping

The resistivity mapping is employed to determine the uniformity of the electrical characteristics of as-grown epitaxial layers. Resistivity measurements were performed in this study using a contactless measurement system manufactured by Lehighton Electronics Inc. LEI-1510C®, which utilizes an eddy current technique to obtain the sheet conductance or resistance and bulk conductivity or resistivity. The measurement configuration, such as the number of measurement points as well as spatial distribution is all user-definable. A magnetic coil, driven by alternating current, drives the measurement system. A conductive epitaxial layer responds to the time-varying magnetic fields from the transducer; therefore, the layer of interest must have a greater conductance than any other layers, including the substrate. Due to this limitation, in the case of a conducting substrate such as *n*-type 6H SiC, the resistivity has to be determined by an alternative method, e.g., Hall-effect measurement.

CHAPTER 3

DEVELOPMENT OF UV AVALANCHE PHOTODIODES

3.1 Introduction

A wide variety of group III-Nitride-based photonic devices have become of great commercial importance in the past decade. These devices have exploited the heteroepitaxial growth of III-N layers on relatively large-area, low cost sapphire and SiC substrates. Photodiodes based on III-N materials can provide improved receiver sensitivity, low noise, and low dark current densities for short-wavelength radiation in the ultraviolet (UV) spectral region. However, for these detectors to compete with photomultiplier tube (PMT) technology in many applications, they are required to have a very high sensitivity and, for optimal sensitivity, they should also operate in Geiger mode, requiring stable avalanche breakdown characteristics. Wide-bandgap UV avalanche photodiodes (APDs), consisting of GaN and SiC *p-i-n* diodes, have demonstrated extremely low leakage currents at 300K and radiation-hardened advantages over photodetectors fabricated in all other currently available semiconductor material systems.[51,52,53,54,55,56,57] However, wide-bandgap Geiger-mode UV avalanche photodiodes demonstrated to date suffer from a relatively high dislocation and defect density, resulting in a low device performance uniformity and a low yield.[57,58] III-N wide-bandgap "intrinsically" deep-UV avalanche photodiodes operating at wavelengths $\lambda < 280$ nm have not yet been developed, especially devices operating in Geiger mode. Even though there have been several reports on APDs grown on sapphire and SiC substrates, the yield of working devices is known to be extremely low, mainly due to the high density of defects in device epitaxial structures which originate from misfit dislocation during heteroepitaxy. In contrast, photomultiplier tubes (PMTs) offer high-sensitivity UV detection with a photocurrent gain as high as 10^6 [59]; however, PMTs

require a high-voltage power supply (> 1,200V) and are relatively fragile and expensive. Due to their compact footprint and material characteristics, APDs are small, stable, and less expensive in comparison to PMTs. Ultraviolet-enhanced Si avalanche photodetectors (UV APDs) can also be used in UV detection systems, but these detectors require complex filters for solar-blind operation, and have demonstrated photon-counting only to $\lambda \sim 400$ nm [60].

It is becoming clear that growth on low-dislocation-density "bulk" III-N substrates has several intrinsic advantages for advanced high-performance devices required for critical applications. UV APDs, a prime candidate for high-sensitivity UV photodetection in a wide variety of sensing applications such as ozone or flame detection in the range 350 ~ 200 nm, is one example. Also, UV APDs based on the AlGaN-GaN material system provide the required detection capabilities in the $\lambda \sim 350$ nm spectral band relevant for bioagent detection. The development of GaN- and AlGaN-based *p-i-n* APDs, however, has been hampered by high dislocation densities in the epitaxial layers, commonly observed in III-N heteroepitaxial growth. The high density of defects and dislocations can lead to a premature microplasma breakdown in the active region of the detector before the electric field in the depletion region can reach the bulk avalanche breakdown field, which has been a major issue for GaN-based APDs.[54,61] This is especially true for deep-UV APDs. Larger-area APD devices failed to work due to the higher probability of the incorporation of defects in the active area and AlGaN-based APD on sapphire has never been demonstrated.

In order to minimize the dislocation density of the devices, the growth of GaN and AlGaN *p-i-n* UV avalanche photodiodes described in this dissertation was carried out by metalorganic chemical vapor deposition (MOCVD) on low-dislocation density ($<10^5$ cm^{-3}) *n*-type "bulk" GaN substrates [52,62].

3.2 Technological Challenges

The wide-bandgap semiconductor avalanche photodiodes offer potentially important advantages in terms of low leakage currents, high radiation hardness, and excellent wavelength selectivity for photon detection in deep UV. However, high dislocation densities, poor device performance uniformities, and hence low device yields have been major barriers for these devices to be commercialized. "Visible-blind" UV APDs have been demonstrated in GaN and 4H-SiC materials (E_g = 3.26 eV); however, APDs made based on the GaN material system have exhibited low yields due to the lack of availability of low-dislocation-density "native" substrates and epitaxial materials.[63,64,65,66] The uniformity of SiC APDs is limited by micropipes and other defects. In addition, SiC is an indirect bandgap material, therefore, the absorption is not strong enough at wavelengths just above bandgap. The badngap is not large enough to achieve solar-blind ($\lambda \sim 280$ nm) and the SiC material system does not have the capability to design peak absorption wavelength. While GaN and SiC by themselves are not suitable for "intrinsically" deep UV APDs due to their relatively low bandgap energies, deep UV APDs having acceptable rejection can be achieved with these materials by having appropriate filters. Due to their wider and direct bandgap nature, GaN-based materials, such as AlGaN or AlInN, will enable heterojunction and intrinsic deep UV APDs to be fabricated in a single material system. However, the lack of a comprehensive understanding of the III-N material systems for Geiger-mode APD applications impedes the progress of such photon detection technologies. Extensive investigation of the semiconductor materials growth process as well as on device operation and device structure design and processing will therefore be needed before the inherent advantages of GaN-based deep UV APDs can be exploited. To address these technological challenges, the MOCVD growth development will be intensively studied for the realization of low-defect-density GaN-based materials such as GaN, AlGaN, AlInN, or InAlGaN novel device structures grown on high-quality bulk III-N substrates.

Despite the suitability of the AlGaN material system, a number of impediments related to the material growth exist in the path of development of such photodiodes. To enumerate:

Material Quality: Largely due to unavailability of suitable substrate for homoepitaxy, materials in the nitride system have to be grown heteroepitaxially with c-plane (0001) sapphire substrate and hexagonal SiC as the most popular substrates which suffer from a large lattice and thermal expansion coefficient mismatch. The growth of a relatively thick $Al_xGa_{1-x}N$ APD structure on GaN templates or compatible substrates introduces technological hurdles such as imperfect materials quality due to dislocations and strain and even strain-induced cracking, as well as a limitation in doping, etc.. A high dislocation density is introduced during the nucleation of the first nitride layer and they tend to thread upwards. The high dislocation density is known to be detrimental to the optical and electrical performance of the devices.

n-type doping: Although *n*-type doping for the nitrides is generally relatively easy, it is not so for the high Al content AlGaN, which is requisite for the development of deep UV APDs. It is known that as Al content surpasses ~ 40%, it becomes extremely difficult to obtain a high doping density and low resistivity. Furthermore, at high Si dopant concentrations, the films tend to crack. For front-contacted mesa geometry, the importance of the n-layer underneath is extremely high. In mesa geometry, compared to the thin (less than 1 μm) *p*-layer that the carriers have to traverse vertically, for the n-layer, the carriers have to traverse a much larger distance (hundreds of μm) horizontally. As a result, the *n*-layer has a larger effect on the overall forward resistance of the device, which in turn is of high importance because of the requirement of obtaining a high current density. Also, the high *n*-layer resistivity leads to current crowding towards the

edge of the mesa, where material quality is poor due to etch related damage leading to the potential for high leakage and premature breakdown of devices.

Active Region: For photonic device purposes, e.g. *p-i-n* APDs, the structure of the active region is of high importance. Theoretically, a wide bandgap material such as GaN exhibits the extremely low reverse leakage current due to the very low intrinsic carrier concentration of $\sim 1.9\times10^{-10}$ cm^{-3} at room temperature [67]; however, the carrier concentration in the unintentionally doped GaN on sapphire or SiC substrate is known to be $\sim 10^{16}$ cm^{-3}. In this case, a relatively large leakage current can exist in the reverse bias regime; thereby, causing the device failure before the onset of avalanche breakdown.

p-layer: In the AlGaN material system, obtaining reasonable *p*-type doping is difficult because of high activation energy of acceptors. The activation energy for p-type GaN:Mg is approximately 160 meV [68] and it increases by ~ 3 meV as Al content increases in the material system. This is a theoretical hurdle. The low free hole concentration translates into higher *p*-layer resistivity. It is also difficult to make good quality ohmic and low resistivity metallization contact to the *p*-layer.

3.3 Epitaxial Growth Development

Generally, it is found that high pressure growth is conducive to better material quality. However, particularly for AlGaN growth, at a higher pressure it is practically impossible to obtain high Al composition because of parasitic reaction. As a result, the Thomas-Swan reactors use a close spacing between wafer carriers and the process-gas showerhead. Hydrogen (H_2) or Nitrogen (N_2) was used as the carrier gas mixed with ammonia (NH_3) as the group V hydride precursor and with EpiPure^{TM} [69] trimethylgallium (TMGa) and trimethylaluminum (TMAl) as the group III alkyl

precursors. Silane (SiH_4) and bis-cyclopentadienyl magnesium (Cp_2Mg) were used as the *n*- and *p*-type dopant precursors, respectively.

3.3.1 Material Growth of GaN

For the growth of GaN on sapphire, a low-temperature buffer layer or nucleation layer is required to overcome the lattice mismatch and improve the material quality of the subsequently grown epitaxial layers. The GaN amorphous buffer layer reduces the interfacial free energy related to the lattice mismatch; thus, the development of optimized growth conditions for the buffer layer is one of key technologies that control the material quality of subsequently growing layers of GaN-based materials. A properly grown low-temperature buffer layer provides a large number of nucleation sites for the subsequent high-temperature growth, resulting in the conversion of the growth mechanism from three-dimensional (3D) islands to quasi-two-dimensional (2D) growth. It is known that the thickness of a low-temperature GaN buffer layer plays a role in terms of the overall material quality for the subsequently grown high-temperature epitaxial layers. The low-temperature buffer layer technique was investigated by Amano et al. [5] and others. [70,71,72] T. Ito, et al. has also found the optimum thickness of the AlN buffer layer to be 20 nm from the relationship between the buffer layer thickness and the crystallinity of GaN layer.[73] The relationship of the growth parameters for a buffer layer such as the growth temperature, thickness, V/III ratio, growth rate (R_g) or thermal annealing was also published.[74,75,76,77,78] However, there is no report published yet regarding the effect of a low-temperature buffer on the strain condition in the epitaxial layers and the overall material quality of subsequently grown epitaxial layers.

The optimized growth condition for a high-quality, thick GaN layer using Thomas Swan 7×2 MOCVD reactor was established by the incorporation of relatively high pressure of 500 Torr to low-temperature GaN buffer layer. The narrow line width of the peak from X-ray rocking curve represents the excellent buffer layer quality. Rocking

curves for symmetric and asymmetric scans are shown in Figure 3.1. The full-width at half-maxima (FWHM) values of (002) and (102) rocking are 260 arc-s and 340 arc-s, respectively. For further improvement of GaN, the thickness effect of low-temperature buffer layer on the crystalline quality and the strain condition of subsequently grown high-temperature GaN layers were studied. Table 3.1 summarizes the growth conditions and the results for the thickness effect study on the buffer layer. As the thickness of low-temperature GaN buffer layer increases, the line width of rocking curves slightly increases; however, the subsequently grown high-temperature GaN shows the reduction of the surface bowing and the smallest curvature value in km^{-1} at the growth time of 100 seconds for low-temperature GaN buffer layer. However, as the buffer layer thickness increases beyond its critical thickneses, the high-temperature GaN experiences the high degree of concave bowing and also FWHM values increase as shown in Figure 3.2.

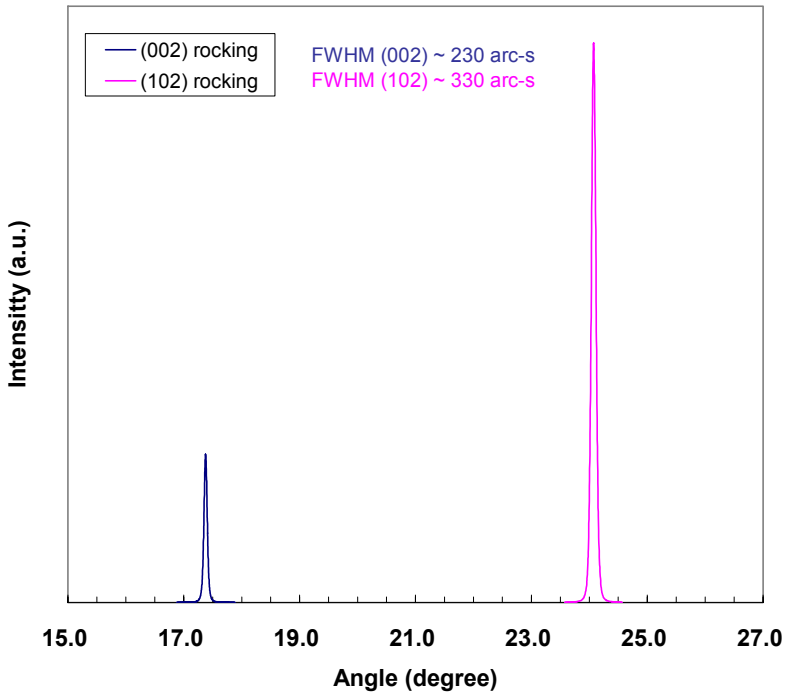

Figure 3.1: The full-width at half-maxima (FWHM) of (002) and (102) rocking for high-temperature GaN grown on sapphire substrate.

Table 3.1: Summary of growth parameter and result for GaN grown on sapphire.

Sample	Growth time for low-temperature buffer layer (sec)	FWHM (002) (arc-s)	FWHM (102) (arc-s)	Curvature (1/R) for high-temperature GaN (km^{-1})
A	80	234	331	58
B	100	259	338	45
C	120	270	338	50
D	150	274	346	53

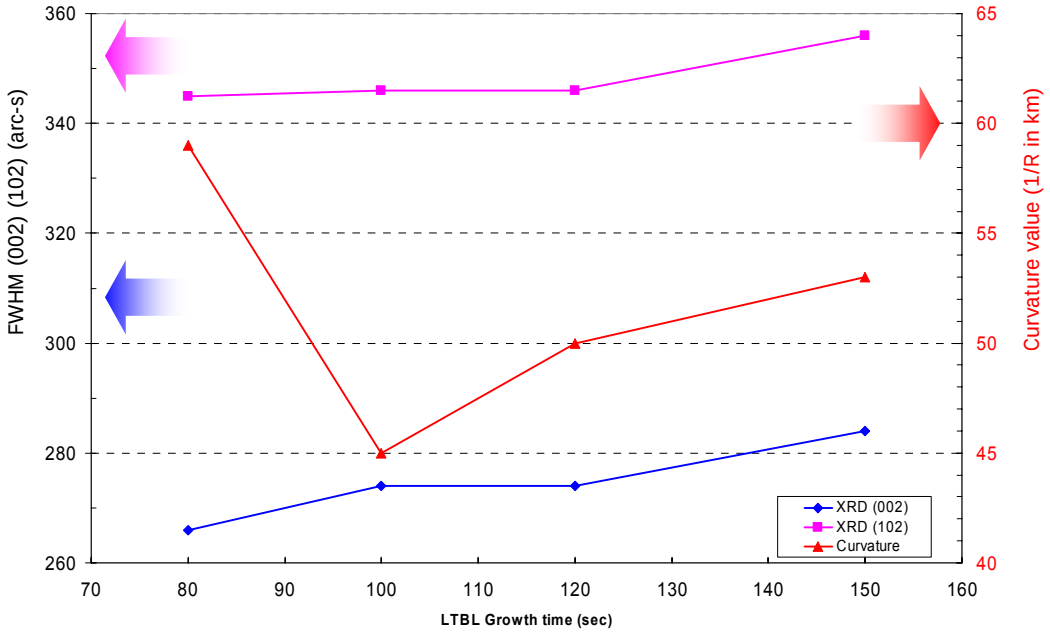

Figure 3.2: Thickness effect of low-temperature GaN buffer layer on the crystalline quality and strain condition of high-temperature GaN on sapphire.

For successful structural design of devices from epitaxial growth, the growth rate for different layers or component of the device structure is one of the parameters that first need to be established. There are several parameters such as growth temperature (T_g), NH_3 flow rate (μmol/min), TMGa (μmol/min) or growth pressure (Torr) which can affect

the growth rate of GaN. To determine the growth behavior of GaN at high temperature, the following relationship is established based on growth parameters.

$$\text{Growth rate } (R_g) = \text{Adsorption rate } (R_a) - \text{Desorption rate } (R_d) \quad (3.1)$$

In the relation (3.1), the adsorption rate should be proportional to the molar flow rate (μmol/min) of the group III precursor (TMGa); however, it could be affected by the adduct formation in the vapor phase. If the growth temperature, growth pressure, and the group V precursor (NH_3) is applied in the same fashion, the effect by the adduct formation should be constant. Unlike the growth of AlGaN or InGaN based material system, the effect of NH_3 on the growth rate is thought to be minimal in case of GaN growth. The desorption rate is a function of growth temperature, growth pressure, and the group V precursor flow rate; hence, the adsorption rate can be calculated as only a function of one parameter described above while the others are fixed. The study on the Desorption rate was carried out with the variation of NH_3 flow only.

The growth rate and the desorption rate were calculated by conducting the following experiments. During the high-temperature GaN growth, the TMGa flow rate was varied while the same growth temperature, growth pressure, and NH_3 flow rate were applied, then, the etching of GaN was followed by the variation of NH_3 flow rate under the same growth temperature and the same growth pressure. The adsorption rate was determined by calculating the summation of the growth rate and desorption rate at a fixed NH_3 condition. Then, the calculated adsorption rate can be used for the estimation of the adsorption rate at other NH_3 flow rate conditions. Finally, the calculation of the growth rate from the relationship (3.1) was performed under the different flow rate of TMGa and NH_3. The experiment was carried out at the growth pressure of 200 Torr.

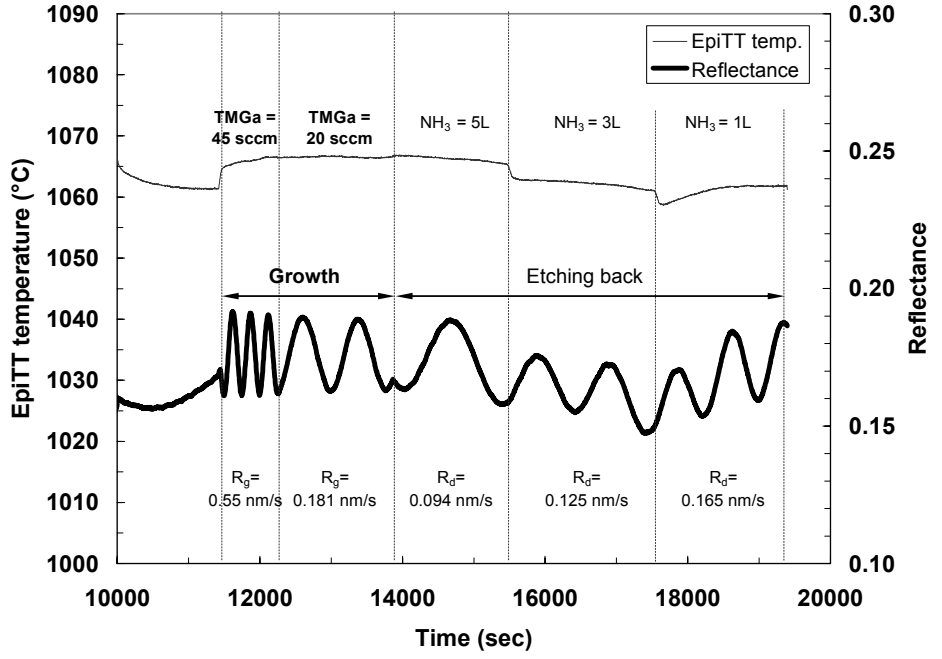

(a)

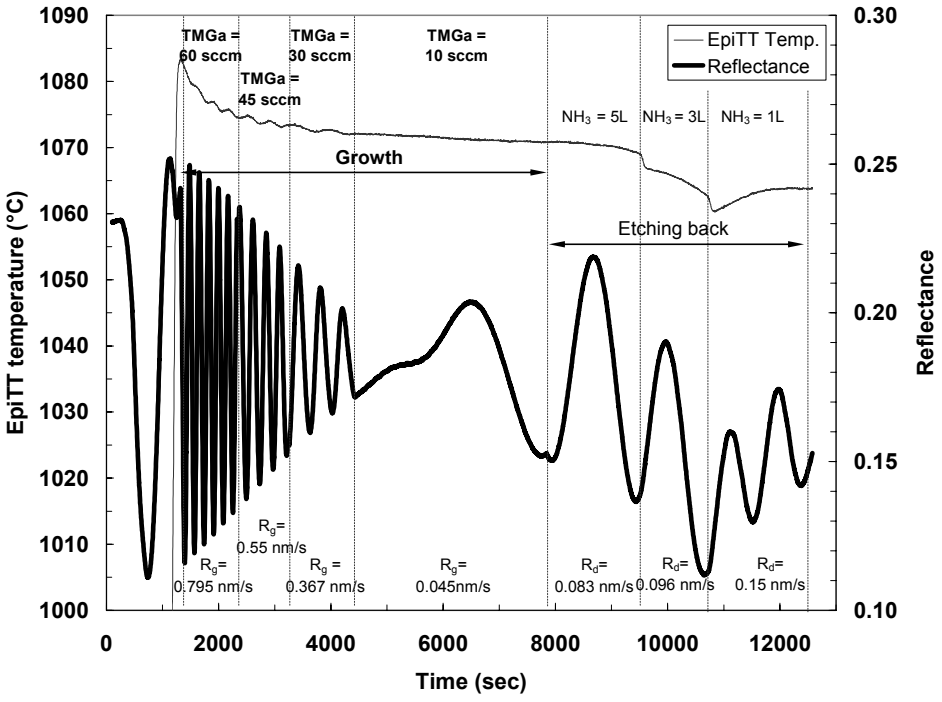

(b)

Figure 3.3: *In-situ* analysis of growth rate and desorption rate for GaN on sapphire with variation of precursor flow rates: at growth pressure of (a) 200 Torr (b) 100 Torr.

In-situ reflectance measurement during the variation of group III and group V precursor flows is shown in Figure 3.3. TMGa flow rate in the ideal molar flow rate (MRF) was varied from 258.1 μmol/min (60 sccm) to 193.6 μmol/min (45 sccm) and reduced to 86.05 μmol/min (20 sccm). For desorption rate, NH3 flow rate was decreased from 0.223 mol/min (5000 sccm) to 0.134 mol/min (3000 sccm) and lowered to 0.045 (1000 sccm) mol/min to introduce the intentional etching effect without the presence of TMGa flow. A similar experiment was also carried out at the growth pressure of 100 Torr to establish the effect of pressure on the growth rate.

Using a wavelength of 633 nm in a EpiTT® *in-situ* analysis tool by LayTec GmbH, adsorption rate, desorption rate, and growth rate were calculated. Growth rate calculations depending on the variation of the group III and group V precursor flow rate at 200 Torr and at 100 Torr are summarized in Table 3.2. Comparison of growth rate, adsorption rate, and desorption rate versus precursor flows is plotted in Figure 3.4. The GaN growth rate is linearly proportional to the TMGa flow rate. As the growth pressure decreases, the growth rate increases at the fixed NH_3 flow of 5000 sccm as shown in Figure 3.4 (a). As the growth pressure changes, the adsorption rate is also linearly proportional to the TMGa flow rate just as in the case of growth rate as plotted in Figure 3.4 (b). The desorption rate increases as the growth pressure decreases and NH_3 flow rate decreases; however, unlike the experiment at 200 Torr, there is non-linear behavior observed at 100 Torr as shown in Figure 3.4 (c).

Table 3.2: (a) Growth rate, adsorption rate and desorption rate at the growth pressure of 200 Torr for GaN on sapphire substrate. (b) Growth rate, adsorption rate and desorption rate at the growth pressure of 100 Torr for GaN on sapphire substrate.

Growth rate (NH_3 = 5000 sccm)		
TMGa (sccm)	Peak-to-peak spacing (sec)	R_g (nm/s)
60	174.9	0.771869640
45	247.9	0.544574425
20	772.6	0.174734662
Desorption rate (TMGa = 0)		
NH_3 (sccm)	Peak-to-peak spacing (sec)	R_d (nm/s)
5000	1429.6	0.094432009
3000	1010.9	0.133544366
1000	779.8	0.173121313
Adsorption rate		
TMGa (sccm)	Peak-to-peak spacing (sec)	R_a (nm/s)
60	170.9	0.866301649
45	238.3	0.639006434
20	393.5	0.269166671

(a)

Growth rate (NH_3 = 5000 sccm)		
TMGa (sccm)	Peak-to-peak spacing (sec)	R_g (nm/s)
60	170.9	0.789935635
45	238.3	0.566512799
30	393.5	0.343074968
10	2450.0	0.055102041
Desorption rate (TMGa = 0)		
NH_3 (sccm)	Peak-to-peak spacing (sec)	R_d (nm/s)
5000	1526.0	0.088466579
3000	1391.2	0.097038528
1000	849.6	0.158898305
Adsorption rate		
TMGa (sccm)	Peak-to-peak spacing (sec)	R_a (nm/s)
60	170.9	0.878402214
45	238.3	0.654979378
30	393.5	0.431541548
10	2450.0	0.143568620

(b)

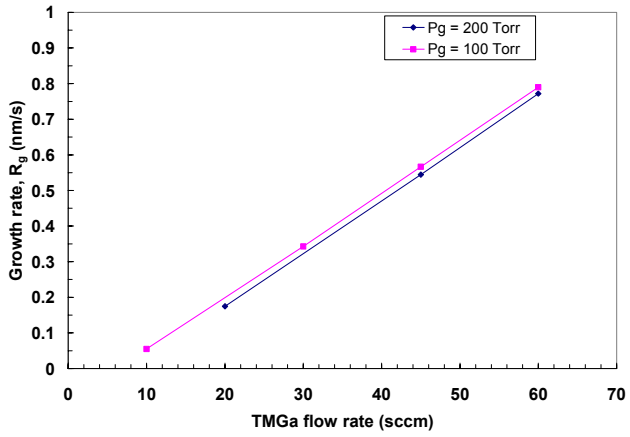

(a)

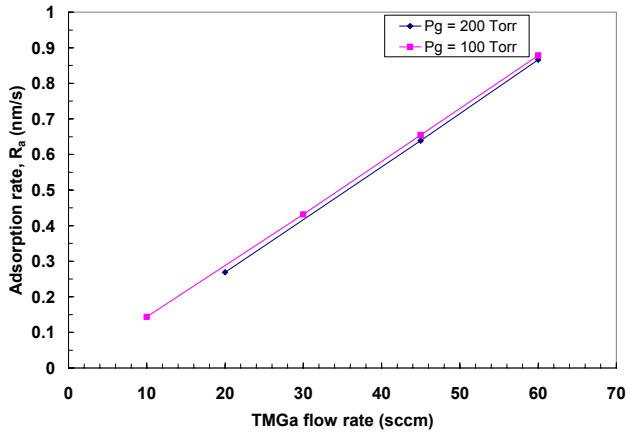

(b)

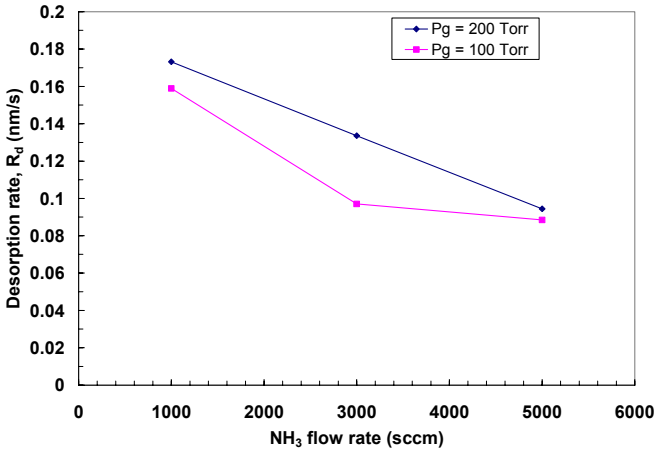

(c)

Figure 3.4: Comparison plot: (a) Growth rate TMGa flow rate at NH_3 = 5000 sccm (b) Adsorption rate versus TMGa flow rate (c) Desorption rate versus NH_3 flow rate.

One important issue regarding the growth rate calibration is the determination of an accurate growth rate. Using three of the available growth rate calibration equipments which are LayTec EpiTT system, Accent Optical Technologies RPM-2000 system, and JEOL 6400 FV SEM, growth rate calibration methods are compared. First, the EpiTT growth rate and thickness calculation utilized the *in-situ* reflectance measurement at the growth temperature. The reflectance versus growth time is obtained using the wavelength of 633 nm. This method could be affected by the thermal expansion along *c*-axis and the change of refractive index as a function of temperature. Second, the thickness calculation by the RPM-2000 system employs the *ex-situ* reflectance measurement at room-temperature. The growth rate is calculated based on the reflectance versus wavelength at room-temperature. The thickness calculation by RPM-2000 system could be affected by the dispersion relation of refractive index. Last, the thickness calculation from the cross-sectional SEM relies on the image contrast of cross-section of the epitaxial layer. In this case, the thickness measurement could be affected by blurred contrast at the interface and the calibration condition of SEM thickness measurement tool. These three tools offer the following growth rate calibrate methods.

- EpiTT calculation using n and k fitting based on Fabry-Pérot oscillation
- EpiTT calculation based on Fabry- Pérot oscillation using pre-defined n and k
- EpiTT calculation using n and k fitting based on sinusoidal wave
- EpiTT calculation based on sinusoidal wave using pre-defined n and k
- RPM2000 thickness mapping using built-in GaN materials database
- RPM2000 thickness mapping using entered n value
- SEM cross-sectional image thickness measurement

For accuracy of the *in-situ* measurement at growth temperature, the effect of thermal expansion along *c*-axis for GaN needs to be established. The lattice constants of GaN ranging from 294K to 753K were measured by M. Leszczynski, et al.[79] The thermal expansion coefficient α along the *c*-axis is linearly proportional to temperature of approximately 600K to 800K show in Figure 3.5. Assuming the linear behavior, thermal expansion along the *c*-axis is extrapolated to a higher temperature regime. Approximately 0.46% of the thermal expansion along the *c*-axis is obtained at 1300K (~1030˚C). However, the thermal expansion coefficient α tends to be higher as temperature increases; therefore, the thermal expansion along the *c*-axis at 1300K can be estimated to be approximately 0.5 ~ 0.6%. The potential inaccuracy of the EpiTT growth rate and thickness calculation at high temperature is thought to be minimal.

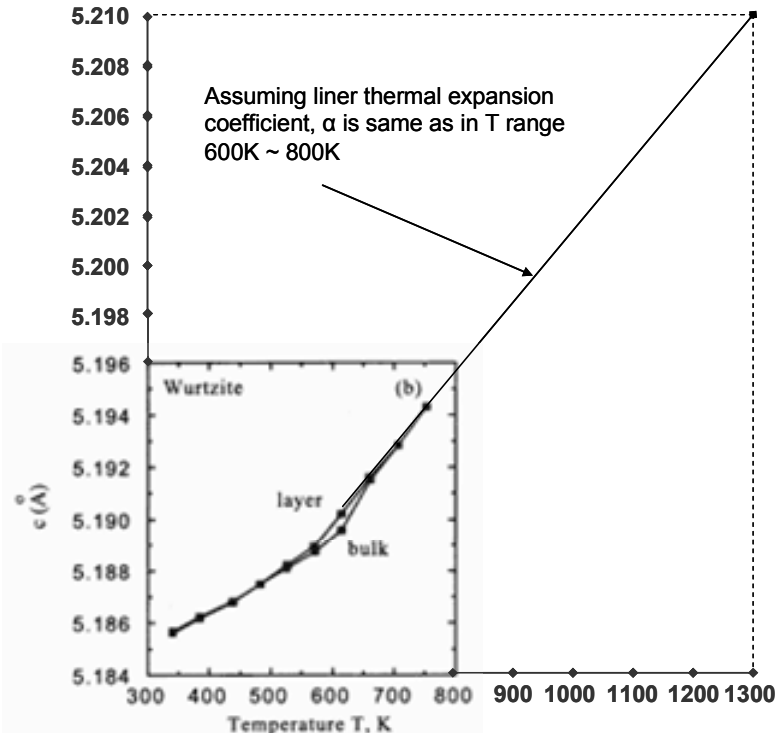

Figure 3.5: Thermal expansion along the *c*-axis versus temperature. Assuming linear thermal expansion coefficient, α is extrapolated to higher temperature based on α measured by M. Leszczynski, et al.[79]

GaN:ud on sapphire substrate (sample #: 1-0329-5) was selected to compare calculation models in the EpiTT system and RPM 2000 system. *In-situ* reflectance data for comparison of growth rate calculation measured by EpiTT during GaN growth on sapphire is shown in Figure 3.6.

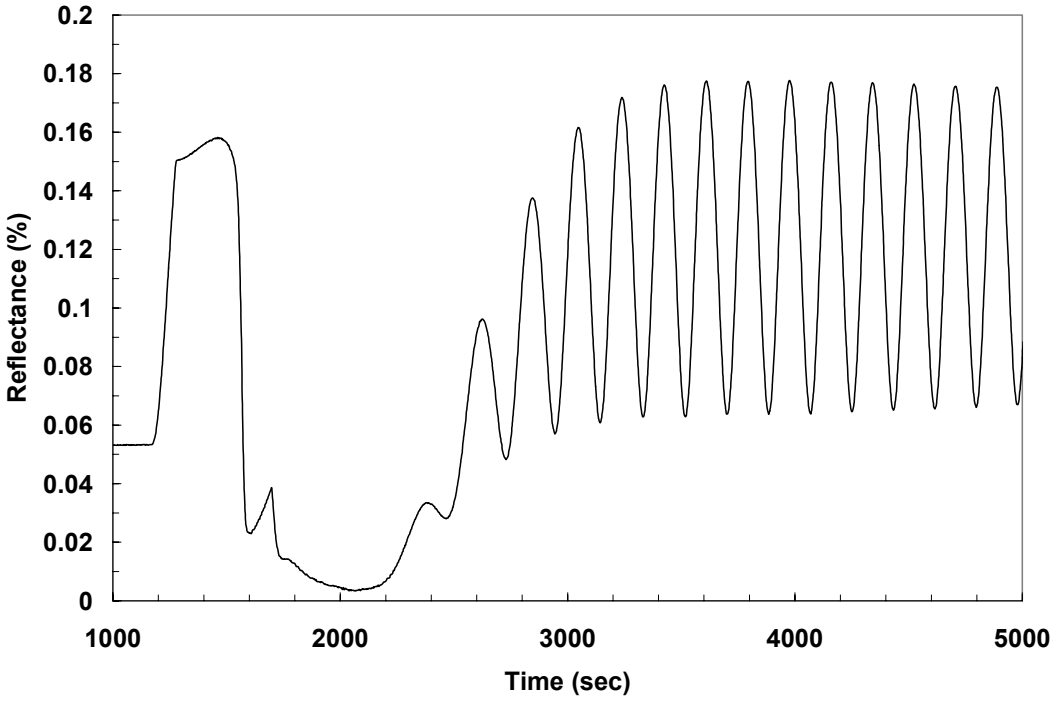

Figure 3.6: *In-situ* reflectance measurement during GaN growth on sapphire substrate using 633 nm.

Three models were employed to analyze the *in-situ* reflectance data shown in Figure 3.6 using the EpiTT growth rate and thickness calculation system. To enumerate:

- n and k fitting based on Fabry- Pérot oscillation
- n and k fitting based on sinusoidal wave
- sinusoidal wave using pre-defined n and k

n and k fitting based on the Fabry-Pérot oscillation is not suitable for less than one peak while the others are not suitable for analysis with multiple peaks. The following scheme was applied in terms of peak selection for growth rate calculation. Three different schemes for peak selection were incorporated: Multiple peaks with more than three peaks, slightly more than single peak but less than two peaks, and slightly less than single peak. Table 3.3 summarizes the comparison among each growth rate calculation method using the appropriate peak selection scheme. Approximately a 0.5% difference of calculated growth rate is observed between peak selection schemes when the Fabry-Pérot oscillation model is applied. Also, sinusoidal wave model shows approximately a 0.5% difference depending on the pre-defined refractive index value for GaN. The high error range found in the sinusoidal wave model may be attributed to the less-than-single peak selection. There is approximately 10% difference in growth rate of GaN between the Fabry-Pérot oscillation model and the sinusoidal wave model.

Table 3.3: Comparison of EpiTT growth rate calculation.

Method	Peak selection	n simulated			k simulated			R calculated		
		n	error range	error %	k	error range	error %	R (nm/s)	error range	error %
FPO using n k fittig	multiple peak	2.533	0.017	1.34%	0	0.013	N/A	0.6853	0.0026	0.76%
FPO using n k fittig	slightly > single peak	2.533	0.015	1.18%	0.002	0.015	N/A	0.6822	0.0032	0.94%
FPO using n k fittig	slightly < single peak	N/A	N/A	N/A	N/A	N/A	N/A	N/A	N/A	N/A
SIN using n k fitting	multiple peak	N/A	N/A	N/A	N/A	N/A	N/A	N/A	N/A	N/A
SIN using n k fitting	slightly < single peak	2.337			0			0.7605	15.2099	3999.97%
Method	Peak selection	n entered			k entered			R calculated		
SIN using fixed n k	slightly < single peak	2.35			0			0.7549	15.0973	3999.81%
SIN using fixed n k	slightly < single peak	2.337			0			0.7591	15.1813	3999.82%
SIN using fixed n k	slightly < single peak	2.33			0			0.7613	15.2269	4000.24%

GaN:ud on sapphire substrate (sample #: 1-0329-5) was chosen for the growth rate calculation using the Accent Optical Technologies RPM-2000 system. Two methods were compared. One is the thickness mapping based on the built-in GaN materials database and dispersion relation and the other is the thickness mapping using the pre-defined (entered) refractive index (n) value for GaN. The refractive index values of 2.35, 2.33 and 2.337 were used for comparison.

Table 3.4: Comparison of growth rate calculation by Accent Optical Technologies RPM-2000 system.

Method	Thickness (μm)	R (nm/s)
GaN database	2.162	0.655152
n=2.35 pre-defined	2.534	0.767879
n=2.34 pre-defined	2.545	0.771212
n=2.33 pre-defined	2.556	0.774545

As shown in Table 3.4, the large difference of 17% is obtained between growth rate calculated by the built-in database and by pre-defined refractive indexes. Even though there is only ~5% discrepancy in refractive index value at 633 nm which is 2.464 (database) versus e.g. 2.35 (entered), the large discrepancy shown in Table 3.4 is possibly due to a dispersion effect. The dispersion relation employed in the material database of RPM-2000 system is described in the equation 3.2

$$n_{GaN}(L \text{ in nm}) = 2.4303 - \frac{2.5633\times10^{2}}{L} + \frac{7.2209\times10^{2}}{L^{2}} + \frac{3.3459\times10^{8}}{L^{3}} - \frac{2.0063\times10^{11}}{L^{4}} + \frac{3.5694\times10^{13}}{L^{5}} \quad (3.2)$$

Based on the equation 3.2, the calculated refractive index values for GaN depending on the wavelengths are summarized in Table 3.5.

Table 3.5: Refractive index values of GaN based on dispersion relation versus wavelength from 500 nm to 700 nm.

Wavelength (nm)	n_{GaN}
500	2.555
600	2.483
633	2.464
650	2.455
700	2.431

The sample 2-0250-5 was selected to compare the growth rate calculation between the cross-sectional SEM and RPM-2000 system. The layer thickness by SEM results in 1.95 μm while RPM-2000 gives 1.94 μm with the built-in material database.

In summation, first, the EpiTT Fabry-Pérot oscillation with n, k fitting simulation, the RPM-2000 GaN material database, and the SEM thickness measurement show the similar growth rate less than 5% difference. Second, the EpiTT sinusoidal wave model with fixed refractive indexes and RPM-2000 with fixed refractive indexes show the similar growth rate; however, the differences in calculated growth rate between these two groups are up to 17%. The growth rate calculation using the EpiTT system possibly has the inaccuracy attributed to the thermal expansion of lattice along the *c*-axis, but the effect is not significant. Another possibility of adding inaccuracy to the growth rate is refractive index which is a function of temperature. The relationship between refractive index versus temperature is not known, but it might not be responsible for over 15% discrepancies. In case of the RPM-2000 system, the dispersion relation of the refractive index is not an issue if a GaN material database is used, but it may be an issue if a fixed refractive index is applied for thickness calculation. A certain degree of difference in growth rate comes from the refractive index differences used in the calculation as well as simulation and calculation. The analysis of growth rate calculation is described in Table 3.6.

Table 3.6: Comparison of growth rate calculations among EpiTT, RPM-2000, and SEM.

Sample	System	Method	R_g	Normallized R_g	Delta R_g %	n used / simulated	Delta n %
1-0329-5	EpiTT	EpioTT FPO using n k fittig selecting muti-peaks	0.6853	1.0459	4.59%	2.533	2.80%
		EpiTT FPO using n k fittig selecting > single peak	0.6822	1.0412	4.12%	2.533	2.80%
		EpiTT SIN using n k fitting selecting < single peak	0.7605	1.1607	16.07%	2.337	-5.15%
		EpiTT SIN using fixed n k selecting < single peak	0.7549	1.1522	15.22%	2.35	-4.63%
		EpiTT SIN using fixed n k selecting < single peak	0.7591	1.1586	15.86%	2.337	-5.15%
		EpiTT SIN using fixed n k selecting < single peak	0.7613	1.1619	16.19%	2.33	-5.44%
	RPM-2000	RPM2000 using GaN database	0.6552	1.0000	0.00%	2.464	0.00%
		RPM2000 using n_GaN=2.35	0.7679	1.1720	17.20%	2.35	-4.63%
		RPM2000 using n_GaN=2.34	0.7712	1.1770	17.70%	2.34	-5.03%
		RPM2000 using n_GaN=2.33	0.7745	1.1821	18.21%	2.33	-5.44%
2-0250-5	RPM-2000	RPM2000 using GaN database	0.5791	1.0000	0.00%	2.464	0.00%
	SEM	SEM cross-section	0.5821	1.0052	0.52%	N/A	N/A

The uniformity of material quality and thickness is one of the key parameters for the optimization of material quality. This is because higher uniformity directly translates into higher yield, making more material over the wafer real-estate useful for device fabrication. The thickness uniformity of thick GaN was measured using the reflectance fringe method on an Accent Optical Technologies RPM-2000 system. The reactor system is provided with three zone heaters. The heater system requires the precise tuning of power setting for better uniformity over a 2″ diameter wafer. The temperature balancing based on the blackbody calibration was carried out to determine the power distribution setting for each zone heater. The standard unintentionally doped GaN on sapphire was grown using the calibrated zone settings. The regrowth of 1 μm-thick GaN:ud on GaN/sapphire template was performed. The regrowth thickness for inner, center, and outer of the wafer from the center of the growth chamber was calculated and fine adjustments of power setting for three zone heaters were carried out. Table 3.7 shows the thickness mapping and thickness standard deviation measured by the RPM-2000 system. The thickness map of a GaN layer from the optimized growth parameters for both a low-temperature GaN buffer layer and ~ 2.3 μm-thick GaN grown at 1050˚C is shown in Figure 3.7. The edge exclusion of 2 mm was applied and it resulted in the record-low thickness standard deviation of 0.950 % for a 2″ diameter wafer, promising the potential capability of high device yield out of a single wafer.

Table 3.7: Thickness uniformity of thick GaN measured using the reflectance fringe method by Accent Optical Technologies RPM-2000 system.

1-0537-1 (GaN:ud)	Zone setting (A/B/C)	Template thickness (μm)	Total thickness (μm)	Regrowth thickness (μm)	Delta (inner-center,center-outer)
outer	79.6/74.3/85	2.296	2.296	N/A	N/A
center	79.6/74.3/85	2.306	2.306	N/A	N/A
inner	79.6/74.3/85	2.317	2.317	N/A	N/A
Std.Dev.		0.95%	0.95%		
1-0523-1 (GaN:ud)	Zone setting (A/B/C)	Template thickness (μm)	Total thickness (μm)	Regrowth thickness (μm)	Delta (inner-center,center-outer)
outer	76.6/72.3/85	2.283	3.741	1.458	
center	76.6/72.3/85	2.147	3.679	1.532	0.074
inner	76.6/72.3/85	2.030	3.615	1.585	0.053
Std.Dev.		4.00%	1.70%		
1-0522-1 (GaN:ud)	Zone setting (A/B/C)	Template thickness (μm)	Total thickness (μm)	Regrowth thickness (μm)	Delta (inner-center,center-outer)
outer	71.6/69.3/85	2.285	3.807	1.522	
center	71.6/69.3/85	2.145	3.732	1.587	0.065
inner	71.6/69.3/85	2.004	3.648	1.644	0.057
Std.Dev.		3.98%	1.91%		
1-0521-1 (GaN:ud)	Zone setting (A/B/C)	Template thickness (μm)	Total thickness (μm)	Regrowth thickness (μm)	Delta (inner-center,center-outer)
outer	51.6/49.3/85	2.299	3.306	1.007	
center	51.6/49.3/85	2.278	3.525	1.247	0.240
inner	51.6/49.3/85	2.011	3.512	1.501	0.254
Std.Dev.		4.13%	3.43%		

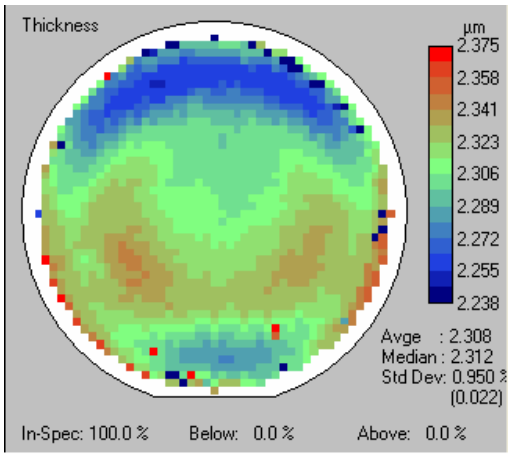

Figure 3.7: Thickness uniformity of thick GaN measured using the reflectance fringe method by Accent Optical Technologies RPM-2000 system.

3.3.2 Material Growth of AlN

For the growth of wide-bandgap, intrinsically solar-blind AlGaN APDs (i.e., devices not requiring extensive and complex filtering for Geiger-mode operation) operating in the spectral region at $\lambda \sim 280$ nm (~ 4.43 eV), the use of sapphire or bulk GaN substrates may not be practical due to the large lattice mismatch between GaN and the $Al_xGa_{1-x}N$ ($x \sim 0.4$-0.5) detector layers. It will result in very small critical thickness of the layers without cracking, but in case of AlGaN epitaxial layers on bulk AlN substrates, AlGaN films will be under compression; therefore, the growth of AlGaN *p-i-n* structures may not lead to epitaxial layer cracking and the layers possibly could exhibit low dislocation densities comparable to that of the underlying AlN substrate. Hence, high-quality, low-dislocation-density bulk AlN substrates are one of the critical elements for the development of deep UV APDs. Even though a bulk AlN could be a choice of substrate for ultimate deep UV APDs, these devices cannot be realized without a high-quality AlN buffer layer.

The growth conditions for AlN were optimized by changing growth pressure, V/III ratio, growth temperature, growth rate, and flow modulation. AlN buffer layers were grown on (0001) sapphire substrates at a low pressure of 75 Torr to minimize the homogeneous gas-phase reactions between TMAl and NH_3.[80,81] The AlN buffer layers were characterized by X-ray diffraction (XRD), atomic force microscopy (AFM), and optical transmittance.

To evaluate the effect of the V/III ratio - the ratio between group V precursors and group III precursors - on the growth of high-temperature AlN, high temperature AlN layers on sapphire under the various V/III ratios were grown. Figure 3.8 shows the *in-situ* reflectance measurement during high-temperature AlN buffer layer growth. As V/III ratio decreases from sample A to sample D, the influence of surface quality on the intensity of the reflected light during AlN growth is represented as the case of ideal growth – maxima and minima of reflectance are not changed. In the case of sample A

grown at relatively high V/III ratio, the *in-situ* reflectance shows that as the surface roughness increases, both maxima and minima decrease.

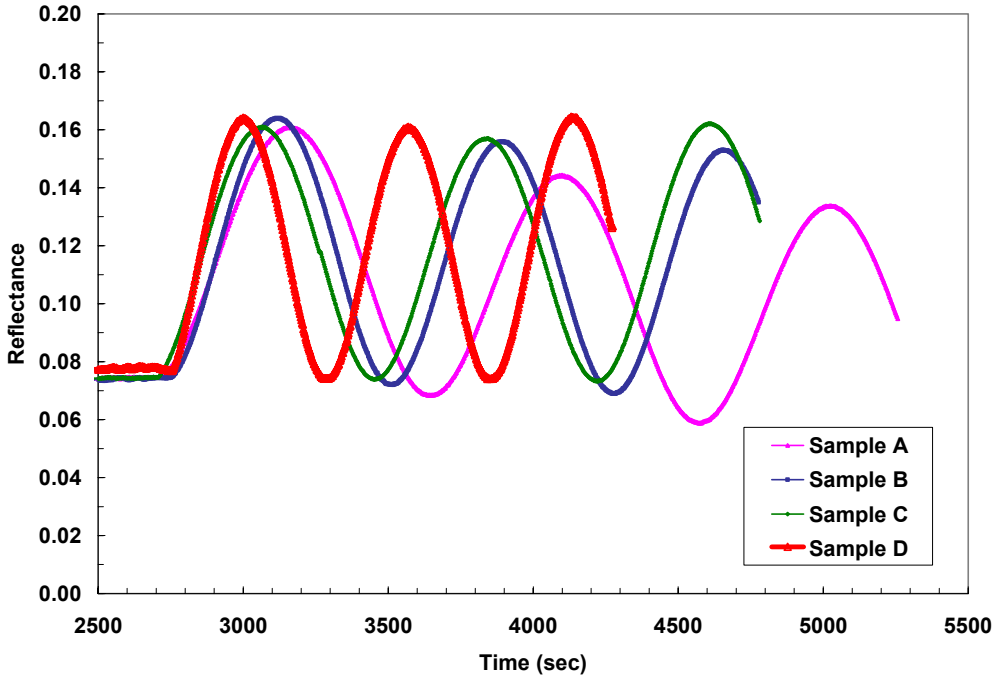

Figure 3.8: *In-situ* reflectance measurement during high-temperature AlN growth under various V/III ratios.

As shown in Figure 3.9, a high-temperature AlN layer grown at relatively high V/III ratio (sample A) reveals a "soft" transmittance cut-off, indicating that the material is absorbing below the band gap due to defects. It can be attributed to the low surface mobility of Al ad-atoms due to the excessive NH_3 flow. As the V/III ratio decreases from sample A to sample D, the optical transmittance characteristics are drastically improved, showing sinusoidal oscillations at the same overall transmittance for wavelengths below bandgap and a sharp decay at the bandgap energy. The red curve in Figure 3.9 is the transmission spectrum corresponding to the sample D which is the AlN layer grown

using optimized low V/III conditions. This spectrum exhibits a sharp cut-off, while AlN layers grown using other conditions have a "soft" cut-off.

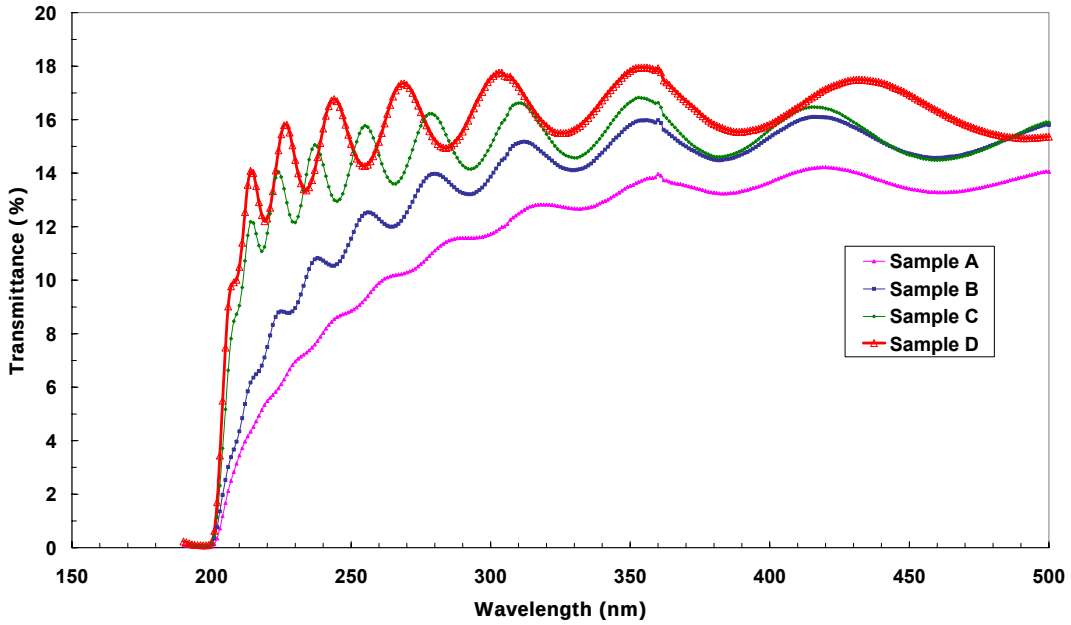

Figure 3.9: Optical transmittance of high-temperature AlN grown on sapphire substrates under various V/III ratios.

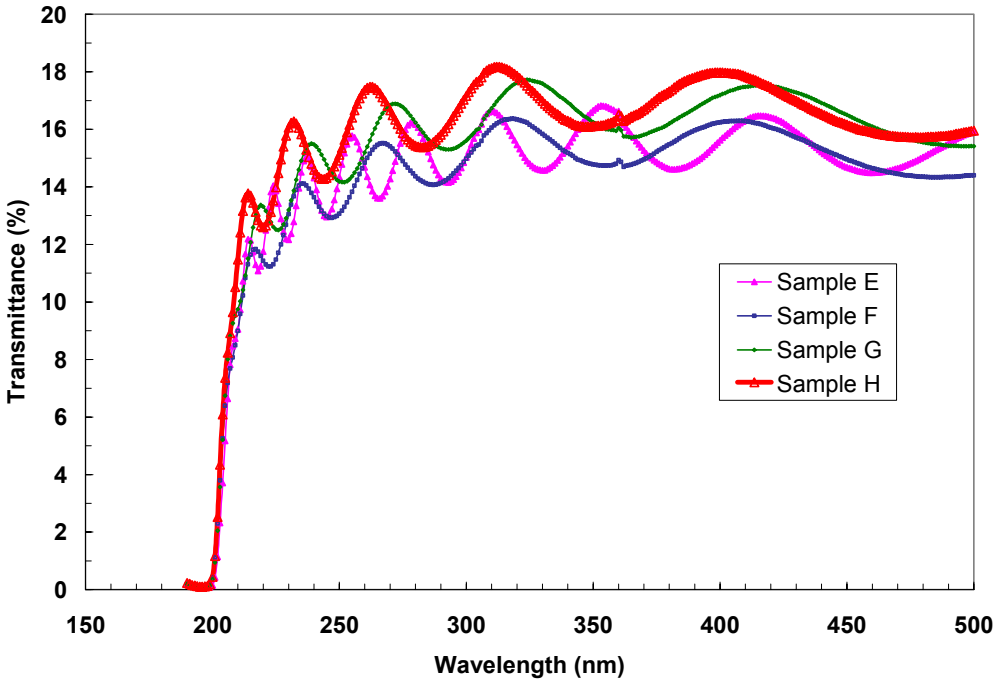

Figure 3.10: *In-situ* reflectance measurement of AlN under various growth temperatures at fixed V/III ratio.

Figure 3.10 shows optical transmittance characteristics of high-temperature AlN layers grown under the variation of growth temperatures while V/III was fixed. As growth temperature increases, the overall material quality of AlN in terms of optical transmittance is improved, indicating that higher growth temperature enhances the mobility of Al ad-atoms on the growing surface and results in two-dimensional growth mode with less defect density in the epitaxial layer.

The microscopic surface morphology of these AlN samples was characterized by AFM. AFM images under the *z*-height of 50 nm in Figure 3.11 shows the effect of V/III ration on the growth mode of AlN. As seen in sample A, AlN grown at a relatively high V/III ratio reveals metal-like islands introduced by 3-D dominated growth behavior. These islands can be attributed to the limited mobility of Al ad-atoms on the surface due

to high NH_3 overpressure. As the V/III ratio decreases from sample A to sample D, 3-D islands begin to disappear while two dimensional growth mode begins to appear. RMS rough values are 13.144 nm, 13.667 nm, and 0.892 nm for sample A, B, and C, respectively. The sample D grown with the lowest V/III ratio shows the RMS roughness value of 0.489 nm per 5×5 μm^2 scan. 1×1 μm^2 scan shown in Figure 3.12 reveals two-dimensional atomic steps on the surface with a RMS roughness value of 0.207 nm.

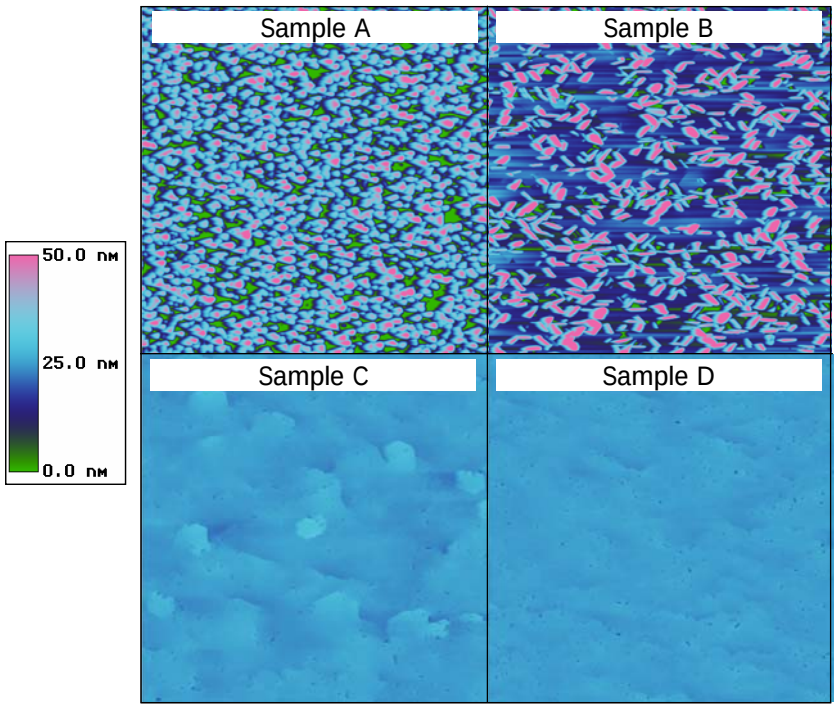

Figure 3.11: AFM microscopic surface morphology of high-temperature AlN on sapphire substrates with variation of V/III ratio; 5×5 μm^2 scan.

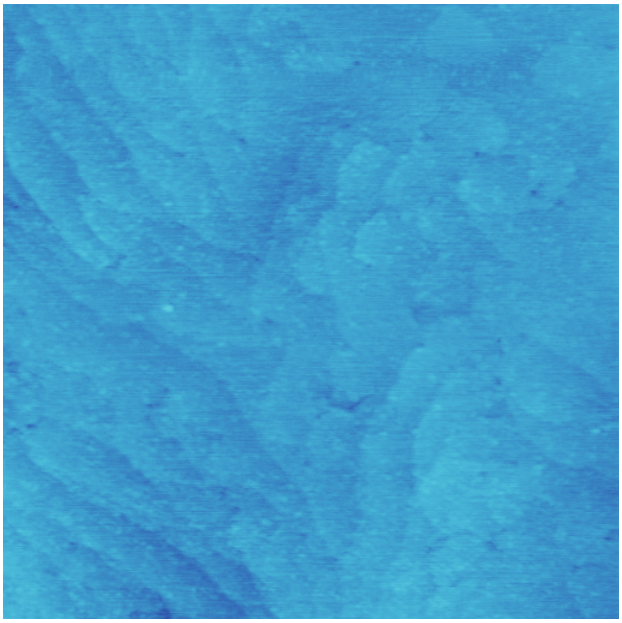

Figure 3.12: AFM microscopic surface morphology of high-temperature AlN grown with optimized conditions on a sapphire substrate showing two-dimensional atomic steps; 1×1 μm^2 scan.

The thickness of a low-temperature AlN buffer layer plays a role in terms of the overall material quality for the subsequently grown high-temperature AlN or AlGaN epitaxial layers. As shown in Figure 3.13, the low-temperature AlN was grown to be 11 nm, 18 nm and 23 nm for sample I, sample J, and sample K, respectively. As seen in shown in Figure 3.14(a), sample I with a relatively thin 11 nm-thick low-temperature AlN reveals a very rough surface, indicating that the thin AlN does not act as a good buffer layer for subsequent high-temperature growth. The influence of surface quality on the intensity of the reflected light for AlN is appeared as the following two cases: (1) ideal growth - detector reflectance is not changed during the growth or (2) surface roughening – both of the peaks and valleys of reflectance intensity decreases. For sample I, with thin low-temperature AlN buffer layer, the *in-situ* reflectance measurement shows the indication of surface roughening. The relatively thick low-temperature AlN buffer

layer also causes a slightly serrated morphology as seen in Figure 3.14(c). There is an optimum thickness for low-temperature AlN that enables it to yield the atomically smooth surface of high-temperature AlN. The *in-situ* reflectance measurement for sample J and sample K exhibit the ideal growth behavior. Both the maxima and minima of reflectance are maintained at the same intensity level throughout the epitaxy. The *in-situ* curvature measurement during the growth of low-temperature AlN shows the decrease in concave bowing. During the heat-up to AlN growth at high-temperature, the wafer shows the characteristic strain increase. As a low-temperature AlN becomes thicker, thus, the wafer experiences less strain during the growth of high-temperature AlN.

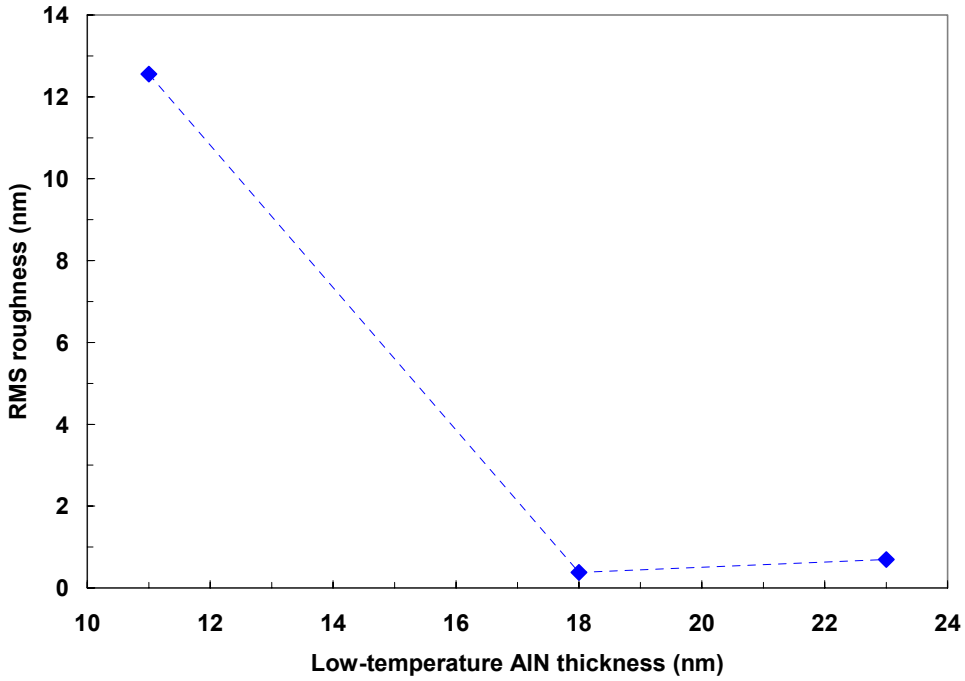

Figure 3.13: Effect of low-temperature AlN thickness on RMS roughness value of AFM microscopic surface; 5×5 μm^2 scan.

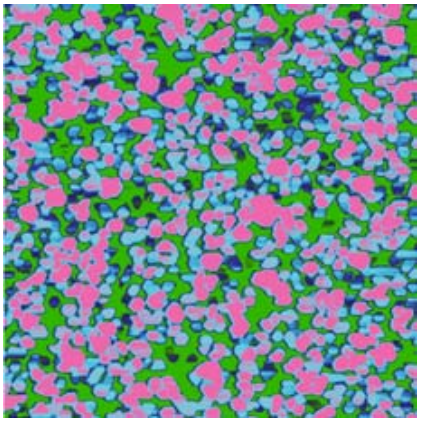

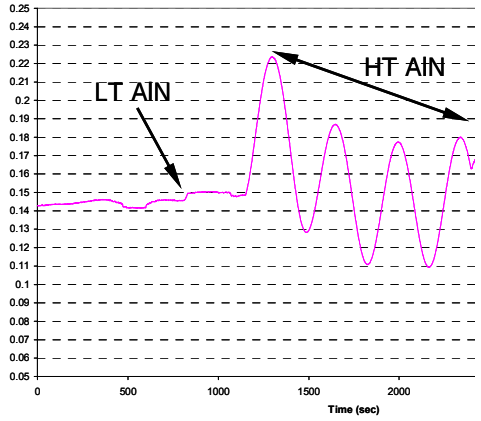

(a)

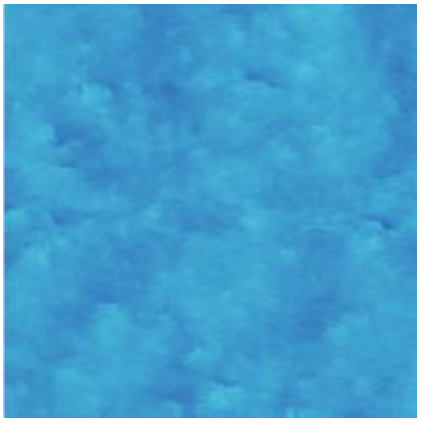

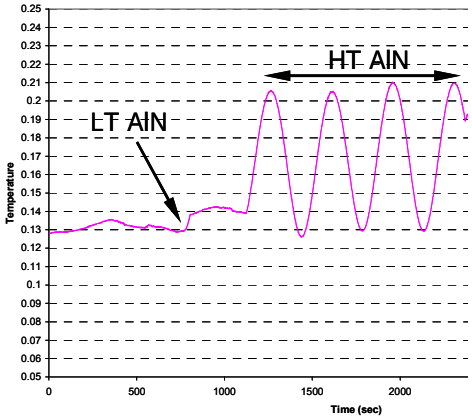

(b)

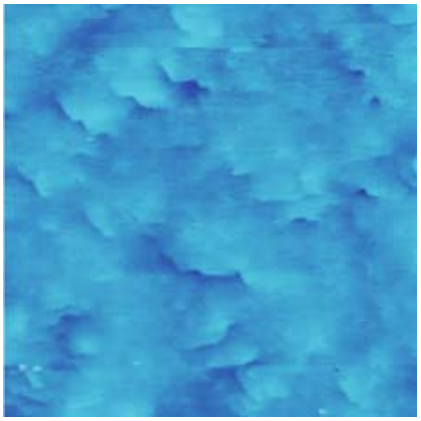

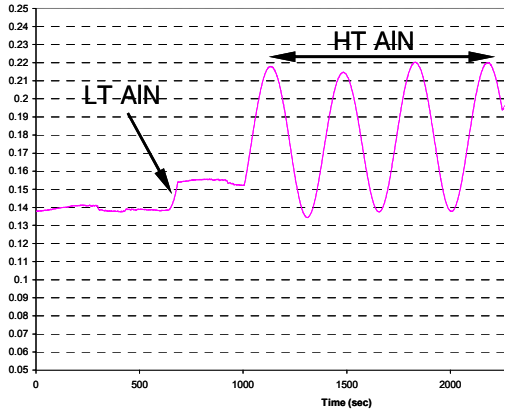

(c)

Figure 3.14: AFM microscopic surface morphology (5×5 μm^2 scan) of high-temperature (HT) AlN under various low-temperature (LT) AlN thicknesses: (a) 11 nm, (b) 18 nm, (c) 23 nm.

3.3.3 Material Growth High-Quality $Al_xGa_{1-x}N$

AlGaN-based wide-bandgap APDs are excellent candidates for short-wavelength photodetection in the UV spectral region of $\lambda < 290$ nm. In order to achieve intrinsically solar-blind APDs, the use of wider-bandgap material than GaN is required. A variety of material quality criteria are needed for growth of AlGaN-based APDs. First, the material quality must be good and the dislocation density has to be low; hence, the excessive leakage current can be minimized and the carriers can get swept across the depletion region. Second, for in mesa geometry of APD devices, the *n*-layer must be capable of effectively spreading the current between the electrode and the device active region because the device series resistance depends largely on the resistivity of the *n*-layer. Third, for the purpose of fabrication, the p-type layer can be thin - as a result, a low-resistivity p-type layer may not be a major requirement, but the capability to grow *p*-type AlGaN is required for the formation of *p-n* junction.

However, the growth of $Al_xGa_{1-x}N$ APD structures on III-N bulk substrates introduces additional technological challenges such as imperfect materials quality accompanied by more stringent growth condition of Al-containing epitaxial materials or dislocations, strain and even strain-induced cracking for the growth on bulk GaN substrates. To achieve high material quality of $Al_xGa_{1-x}N$, various growth parameters and schemes were studied. Also, to prevent the initiation and propagation of cracks, several strain management structures were investigated between a substrate and AlGaN epitaxial layers. The detail of these growth techniques will be discussed in the following chapter.

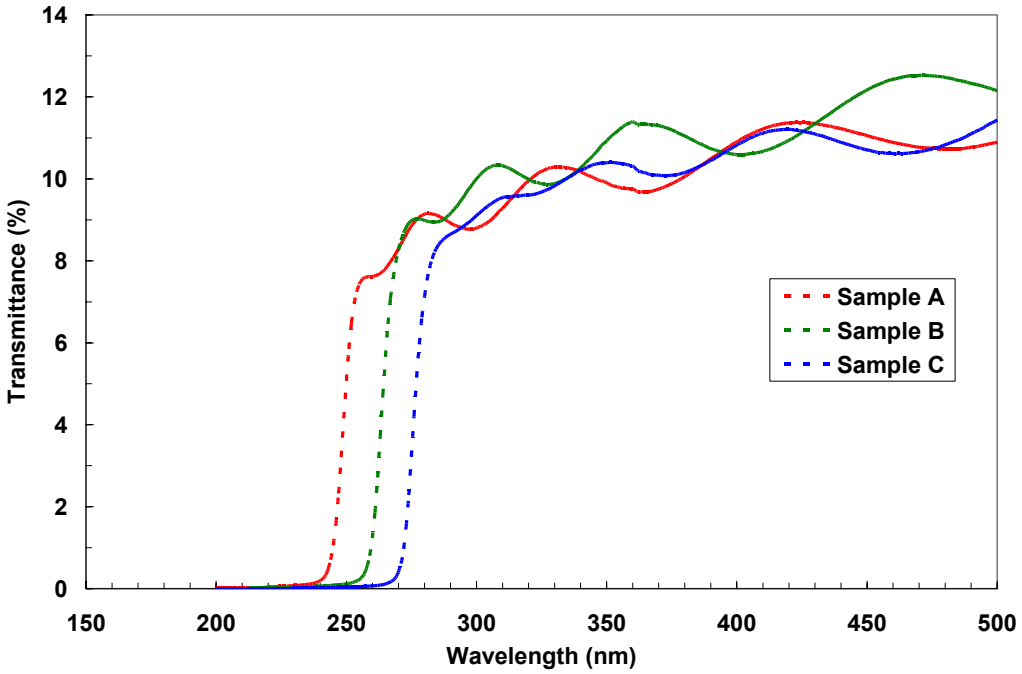

Figure 3.15: Optical transmittance spectra of AlGaN at different compositions.

The development of high Al-content AlGaN layers with demonstrated optical and electrical characteristics as well as high uniformity and reproducibility is one of the key elements for AlGaN-based APDs. For the fabrication of flip-chip array APDs, the *n*-layer should have cut-off wavelengths shorter than the peak absorption wavelength in the depletion region. The optical transmittance spectra of the relatively thin 260 nm-thick AlGaN layers grown are shown in Figure 3.15. Sharp transmittance cut-offs are obtained under various AlGaN layers. The cut-off wavelengths for sample A, sample B, and sample C are 249 nm (Al ~ 54%), 264 nm (Al ~ 45%), and 275 nm (Al ~ 38%), respectively. [49]

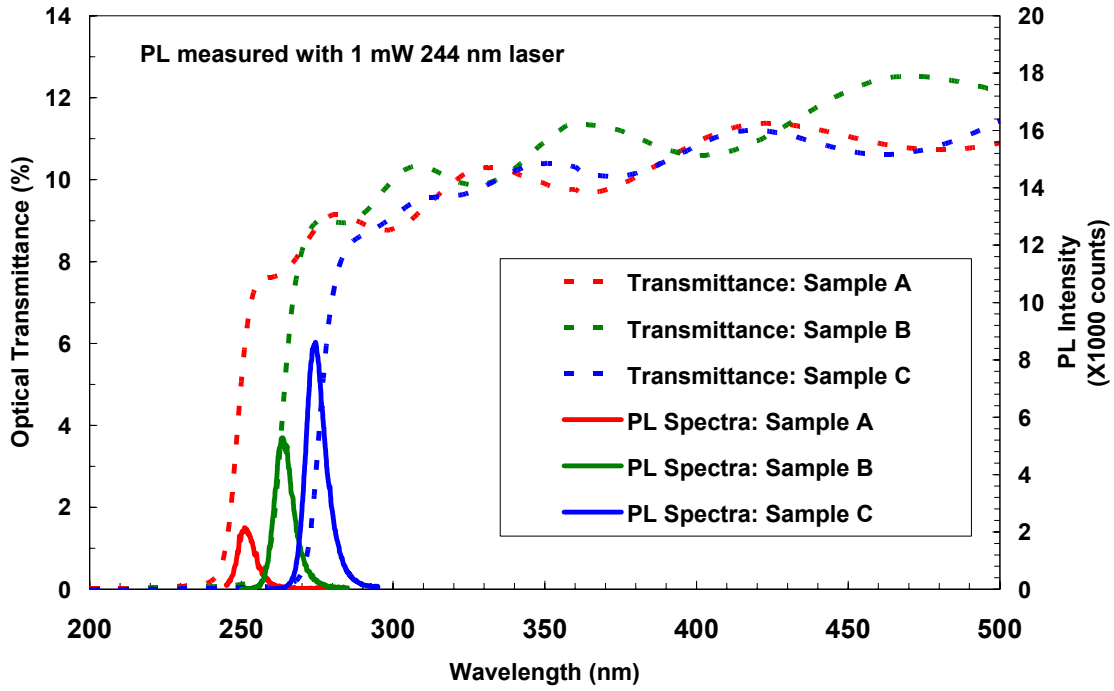

Figure 3.16: AlGaN Photoluminescence (PL) data alongside optical transmittance data.

Room temperature PL measurements on these same samples were performed by Dr. Charles Collins at AFRL using a Coherent Innova Tech 90C FreD frequency doubled Ar-ion laser. The detection optics consisted of Specs 1404 double spectrometer and Products for research PMT. The PL data is plotted along with the transmittance data in Figure 3.16. The narrow FWHM (~ 8 nm) room-temperature PL is obtained with a PL peak wavelength as short as 253 nm. Also notable is the fact that the transmittance cut-off aligns very well with PL peak wavelength establishing that the PL is from band-edge and also indicating the absence of near bandgap optically active defect states. For sample A, the apparent slight discrepancy between the PL peak and transmittance cut-off is observed. This can probably be attributed to the fact that the emission wavelength is very close to the pumping wavelength and the filter in detection optics in the PL system cuts off near this wavelength region. There is also a slight shift found in sample C, but in this

case, some blue shift could be originated from the fact that the pumping power of the laser is strong enough to pump carriers higher than the bandgap energy.

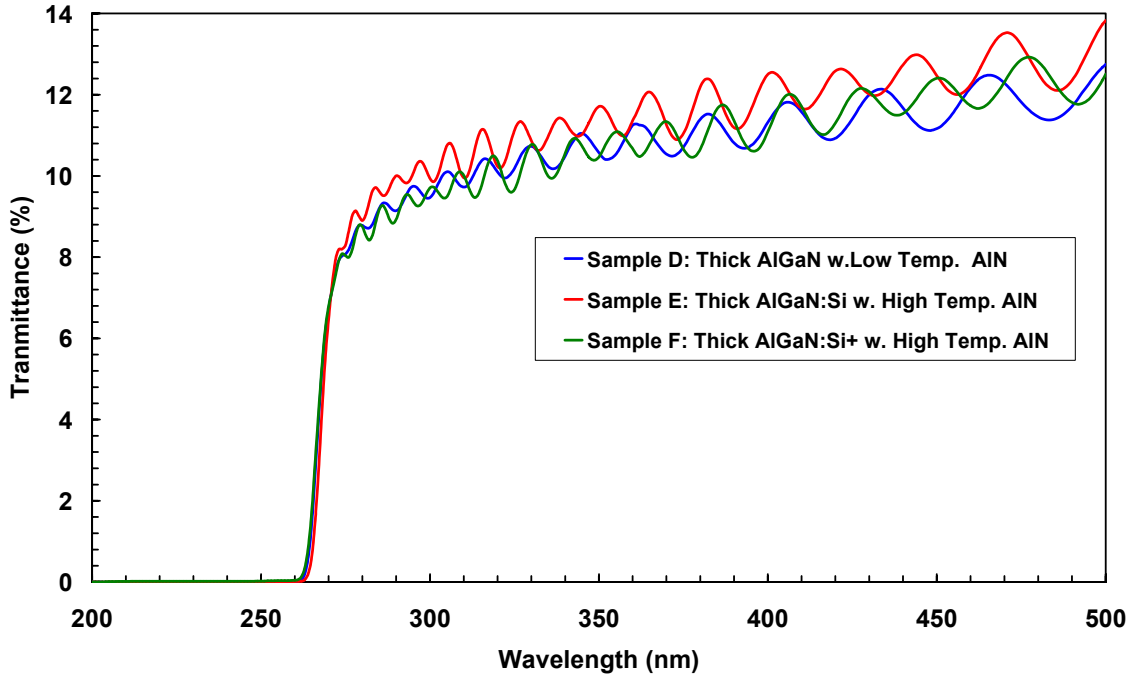

Figure 3.17: Optical transmittance spectra from 1.2 µm-thick AlGaN epitaxial layers grown under different conditions.

After growth of these thin calibration samples, the growth of a 1.2 µm-thick AlGaN layer was attempted. The crack-free growth of a thick *n*-type AlGaN:Si layer is essential to the growth of APDs because the threading dislocations generated at the nucleation layer tend to be annihilated as material grows thicker. Thick AlGaN layers with transmittance cut-off wavelengths of 268 nm on high and low temperature AlN buffer layers and also under highly Si-doped conditions were successfully grown. Also notable is the fact that with variation of nucleation layer and doping conditions, the Al

content in the alloy was found to be very stable and reproducible which is evident from the optical transmittance spectra shown in Figure 3.17.

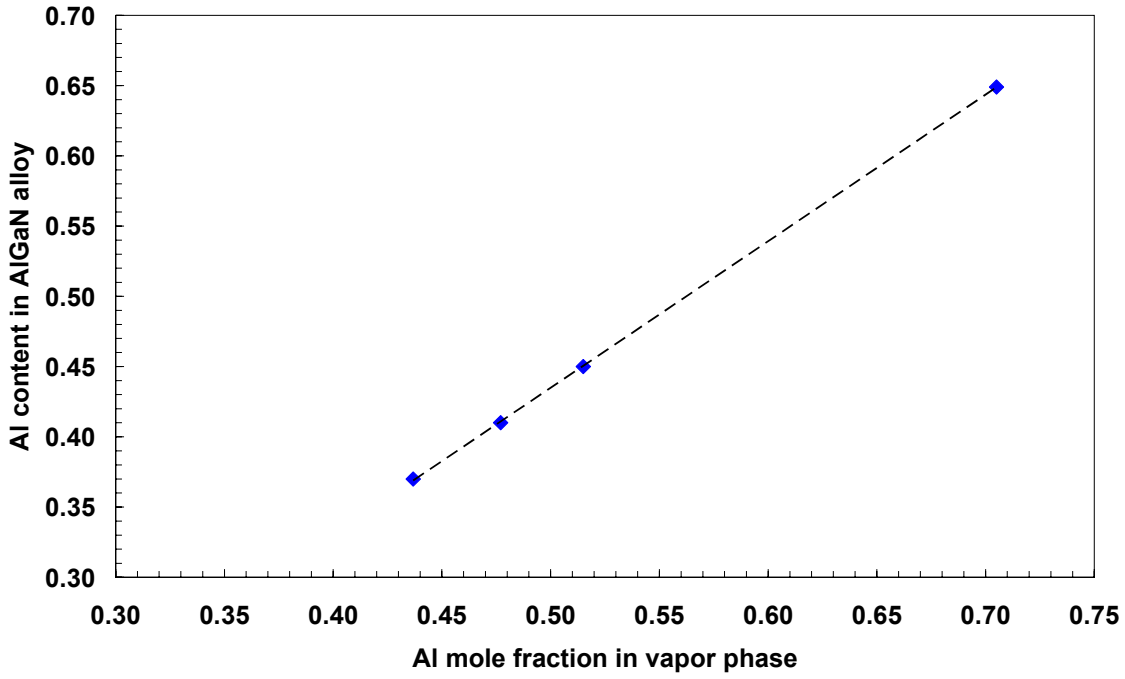

Figure 3.18: Al content in AlGaN alloy versus Al mole fraction in vapor phase while total group-III mole fraction is kept constant.

The stability and reproducibility of AlGaN growth conditions are additionally proven from the correlation of Al and Ga molar flows with growth rate and alloy composition. A series of AlGaN runs were performed with various Al to Ga molar flow ratios keeping the total group-III molar flow constant. The growth rate was found to not change with varying Al to Ga ratios and the Al content in the AlGaN alloy was found to be linear to a good approximation, indicating that adduct formation is minimized. The plot of Al content in AlGaN alloy versus Al mole fraction in the vapor phase is shown in Figure 3.18.

Table 3.8 summarizes the growth parameters for a series of AlGaN samples with the variation of TMAl and TMGa flows. The relationship between the total group III molar flow and Ga bubbling/incorporation efficiency for AlGaN growth at 75 Torr is also shown in Figure 3.19. The linear trend line is plotted together. R^2 is found to be ~ 1. There is a good linear approximation between the total group III molar flow and Ga incorporation/bubbling efficiency, indicating that Ga desorption is a dominant factor while the adduct formation or deposition on the showerhead does not play a significant role. The assumption that only Ga experiences the desorption while Al incorporation in the solid phase is approximated to be 100% can also be validated from the ratio of total group III molar flow rate versus growth rate (R_g) in Table 3.8.

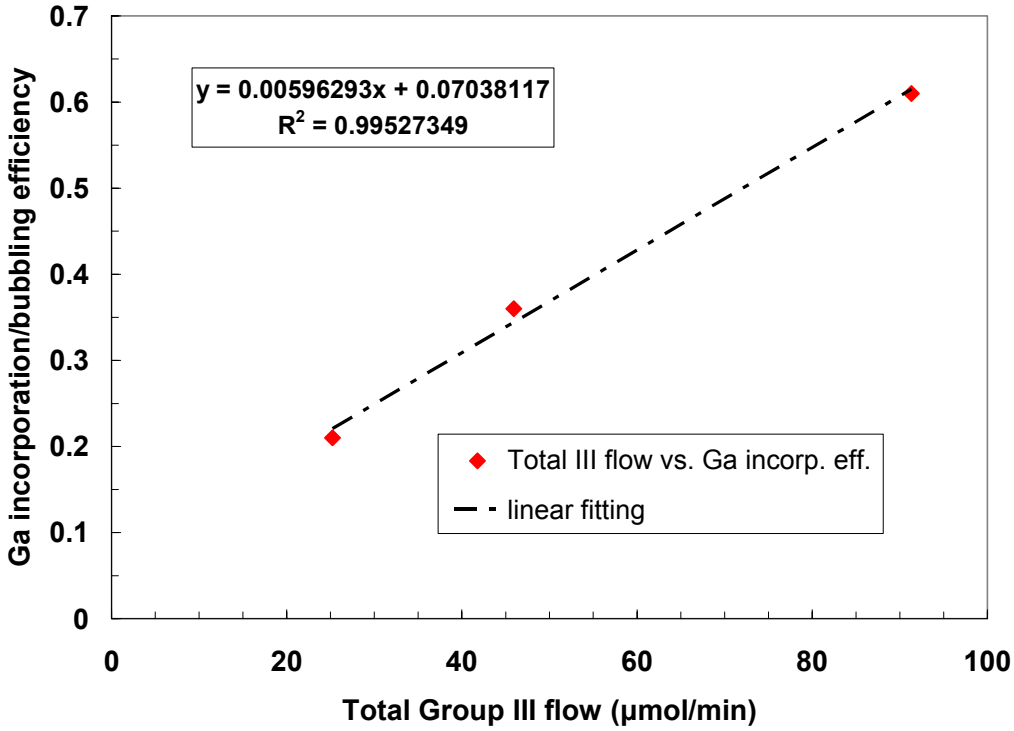

Figure 3.19: Ga incorporation/bubbling efficiency versus total group III molar flow in AlGaN growth.

Table 3.8: Summary of growth parameters for AlGaN layers under the variation of total group III molar flow rate.

Ga incorp. efficiency	Total III flow (μmol/min)	R_g (nm/s)	Total III flow/R_g	Total III flow/Ga incorp.
0.61	91.32	0.186	491	150
0.36	45.94	0.095	484	128
0.21	25.22	0.052	485	120

One of the important aspects of deep-UV APDs is the ability to obtain high *n*-type doping in the high Al content AlGaN alloy. The high doping density is essential because otherwise, the spreading resistance in the *n*-contact layer becomes too high and causes ohmic heating. Based on growth optimizations, a low resistivity AlGaN:Si with transmittance 50% cut-off at 267 nm was obtained. The resistivity map measured using a Lehighton contactless resistivity probe is shown in Figure 3.20. The average resistivity for a 1.2 μm-thick AlGaN epitaxial layer is found to be 1187 Ω/square with the standard deviation of 195 Ω/square. The transmittance spectra for these AlGaN samples are found in Figure 3.17. Hall effect measurements on $Al_xGa_{1-x}N$:Si ($x \sim 0.5$) using Ti or V/Al/Ti/Au metal contact from bottom to top exhibit the free carrier concentration of $n \sim 2.4\times10^{18}$ cm^{-3} with a mobility (μ) of over 50 $cm^2/V\cdot s$ and bulk resistivity (ρ) as low as 5×10^{-2} Ω-cm. An AFM image of a typical $Al_xGa_{1-x}N$:Si ($x \sim 0.5$) in 5×5 μm^2 with z-height of 20 nm is shown in Figure 3.21.

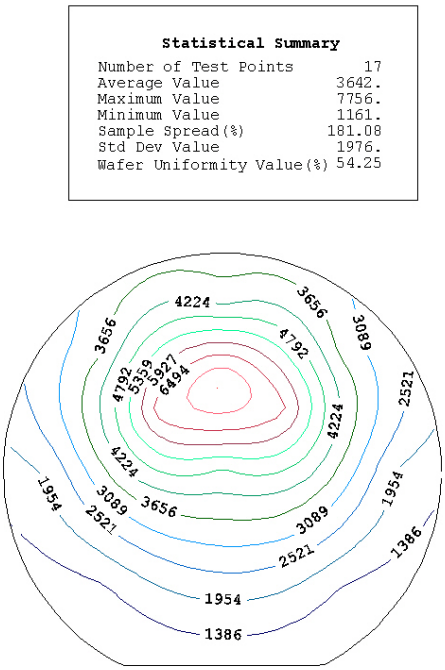

(a)

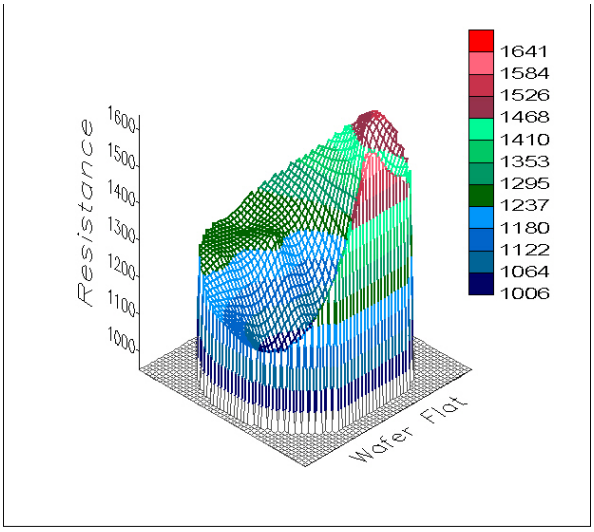

(b)

Figure 3.20: Resistivity map of AlGaN:Si epitaxial layer; transmittance 50% cut-off at 267 nm: (a) Contour map (b) 3D surface map.

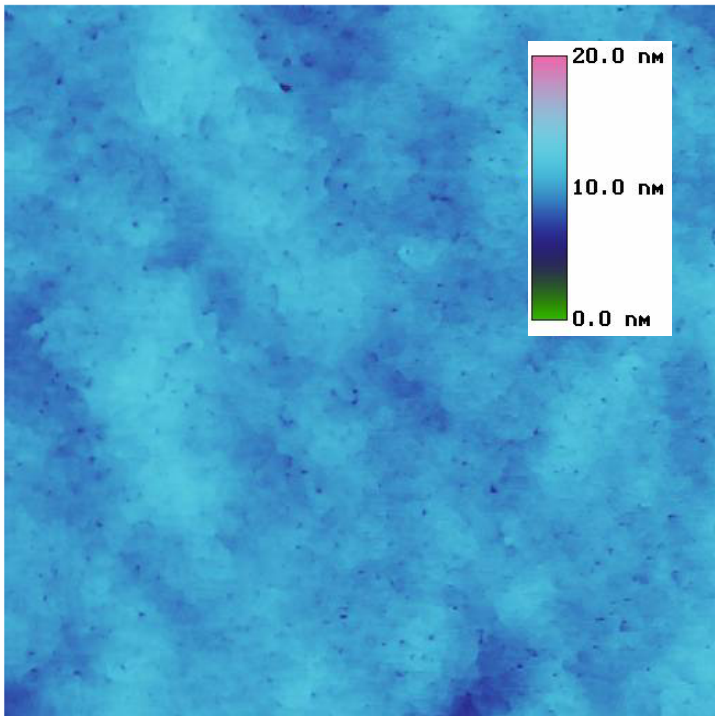

Figure 3.21: AFM image of a typical $Al_xGa_{1-x}N$:Si ($x \sim 0.5$) in 5×5 μm^2 with z-height of 20 nm.

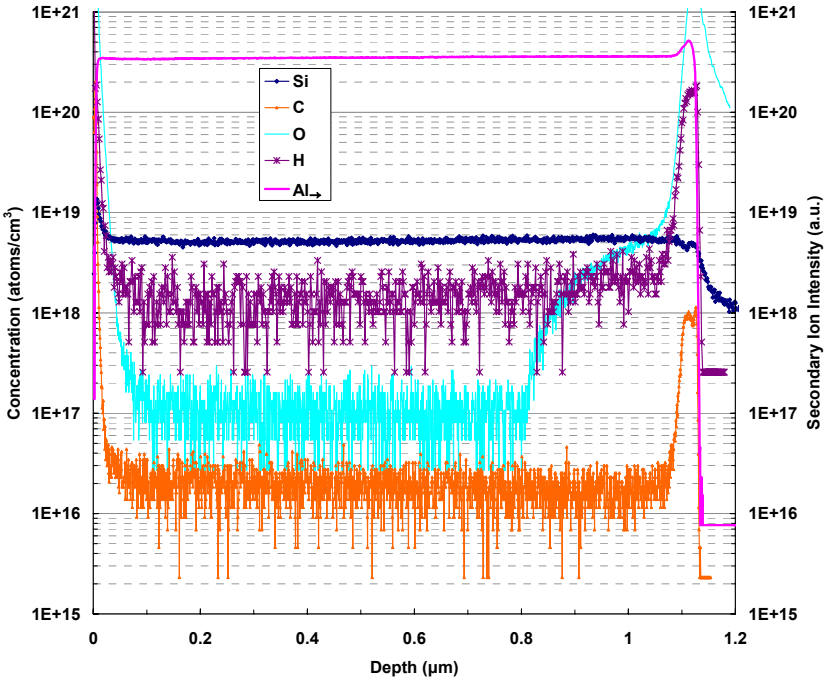

(a)

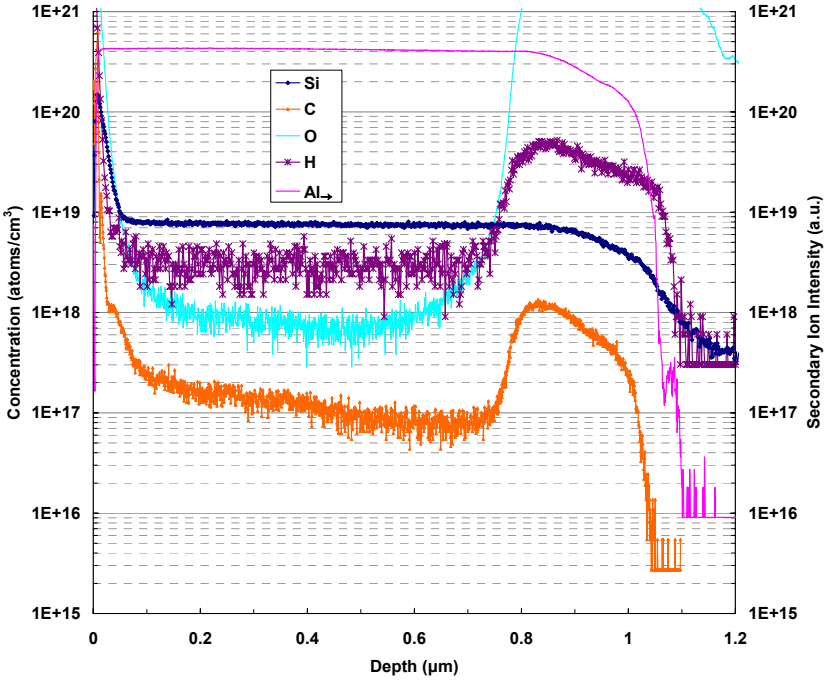

(b)

Figure 3.22: SIMS analysis of $Al_xGa_{1-x}N$ ($x \sim 0.45$) layers grown at different temperatures: (a) relatively high temperature (b) relatively low temperature.

The impurity level in the AlGaN epitaxial layer can be used as a verification tool for MOCVD reactor, growth chamber, and precursor sources. A high-aluminum content AlGaN layer is one of the good candidates. Figure 3.22 shows impurity levels of $Al_xGa_{1-x}N$:Si (Al ~ 0.45) measured by secondary ion mass spectroscopy (SIMS). Samples are grown at two different temperatures. The sample grown at a relatively high temperature reveals low levels of carbon (low 10^{16}) and oxygen (low 10^{17}) incorporation, verifying low levels of impurities in the epitaxial layer. Impurity levels of the sample grown at a relatively low temperature are higher. This is considered to be a result of the relatively low growth temperature. Impurity incorporation could also depend on growth temperature as well as aluminum composition, assuming that the same condition of growth chamber and precursors are employed in the growth.

As a continuing study of impurity incorporation, the impurity incorporation behavior depending on growth temperature has been investigated. The aluminum composition in AlGaN alloy is selected at Al ~ 0.45 to make the structure sensitive enough to impurities such as oxygen, and temperature is changed in the same growth. Figure 3.23 shows impurity levels of an $Al_xGa_{1-x}N$:Si (x_{Al} ~ 0.45) structure, consisting of three different growth temperatures ($T_1 > T_2 > T_3$) measured by SIMS. All AlGaN layers grown at the three different temperatures exhibit low levels of carbon (mid ~ high 10^{16}) and oxygen (low 10^{17}) independent of growth temperatures. For oxygen, the impurity level does not increase with decreasing growth temperature within the temperature of interest for the experiment. Carbon incorporation appears to be slightly reduced with increasing temperature. The high impurity concentration shown in the initial growth of the epitaxial layer at T_1 is considered to be artifact introduced by the roughened surface after extended sputtering during the SIMS measurement.

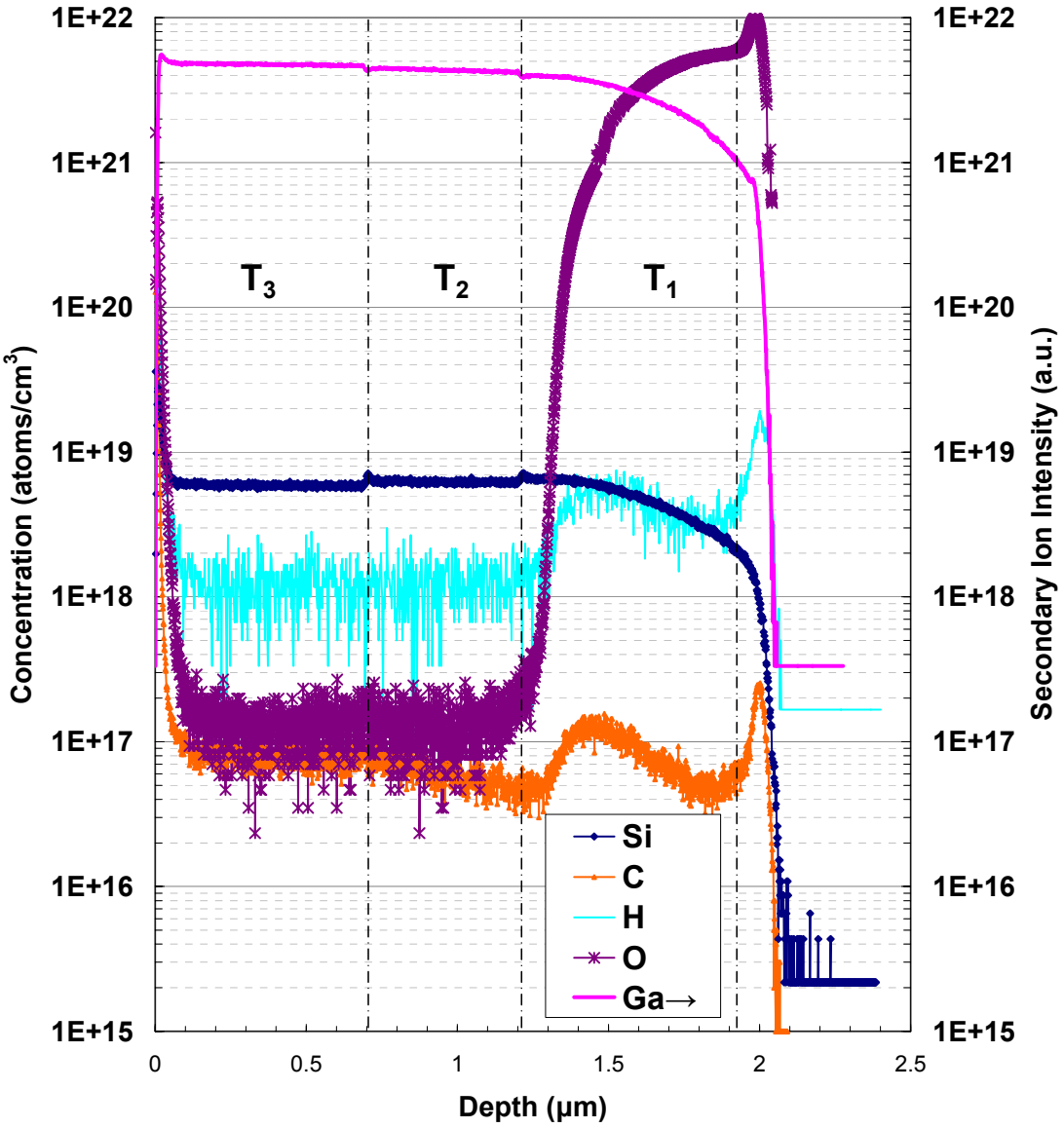

Figure 3.23: SIMS analysis of $Al_xGa_{1-x}N$:Si (x_{Al} ~ 0.45) layers grown at three different temperatures ($T_1 > T_2 > T_3$).

The heteroepitaxy of group III-N materials on substrates with large lattice and thermal mismatch introduces low device performance uniformity and yield, which makes photodetector array impossible. The device performance is also limited by material defects. The uniformity of material quality and thickness is one of the key elements to ensure the realization of APD array and Geiger-mode detectors. This is because higher uniformity with low defect density directly translates into higher yield making more material for device fabrication. As shown in Figure 3.24, the growth optimization of high Al-content $Al_xGa_{1-x}N$ ($x > 0.5$) on AlN indicates excellent uniformity of high Al-content AlGaN material. Multiple scans of the transmittance spectra reveal the uniformity of Al composition over 2″ diameter substrate with the sharp transmittance 50% cut-off. The difference in cut-off wavelengths is only about 5 nm. This can be translated into the fact that AlGaN material does not absorb below the energy band gap and the band diagram of the material has a small number of defect or impurity related states in-between the two band-edges.

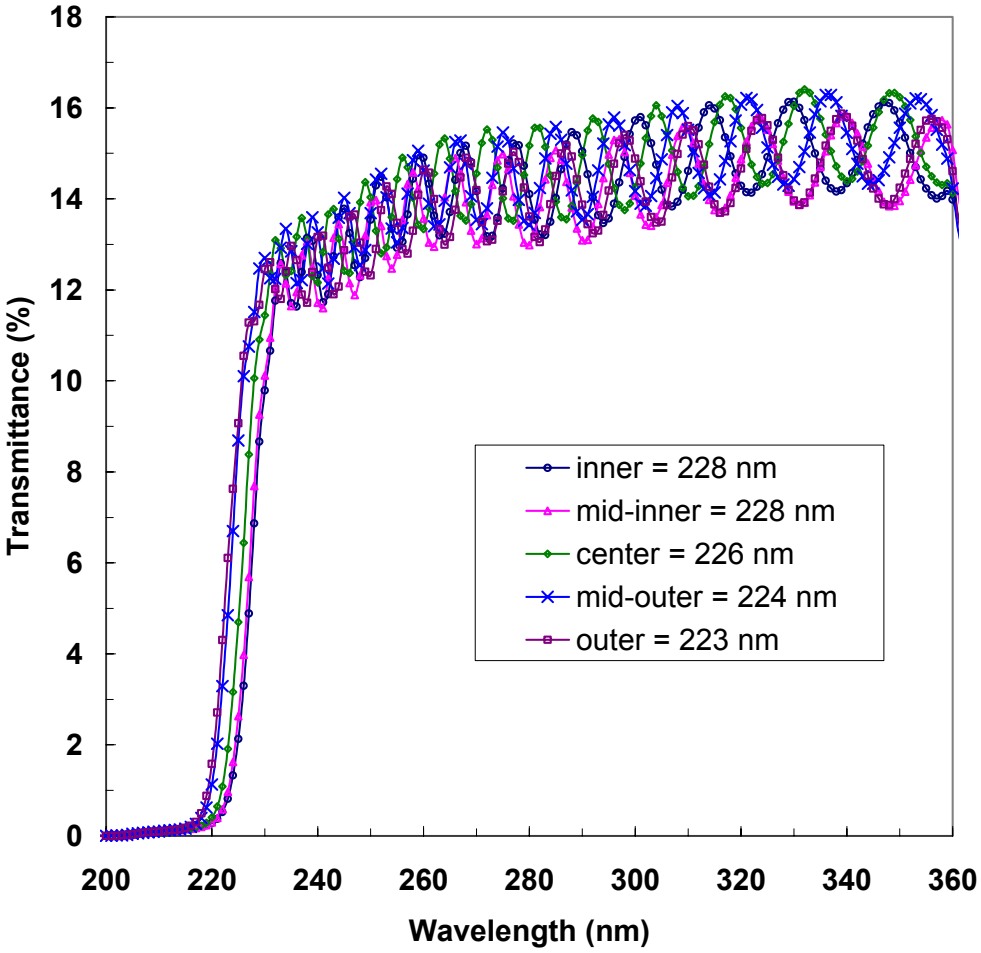

Figure 3.24: Optical transmittance spectra of high Al-content AlGaN targeted for deep UV APDs.

The incorporation of a bulk AlN substrate is suitable for the development of ultimate deep UV APDs with $Al_xGa_{1-x}N$ ($x > 0.3$). The growth of AlGaN epitaxial layers on a bulk AlN substrate offers the following technological advantages. First, AlGaN layers are less prone to crack formations inherited from in-plane compressive strain with respect to the substrate. Second, the substrate band edge is transparent to deep UV spectral regime. Last, having a UV transparent substrate enables both front and back illumination device geometry; however, the quality and size of bulk AlN substrates are still in development. On the other hand, AlGaN layers grown on a bulk GaN substrate experience in-plane tensile strain with respect to the substrate. For the growth of $Al_xGa_{1-x}N$ on GaN templates, crack formations can be expected due to in-plane tensile strain of the epitaxial layer on the template when it passes its critical thickness; therefore, the development of strain management engineering in designing epitaxial structures is inevitable. In addition, the substrate is not UV transparent; therefore, back illumination can not be realized. There is absorption in *p*-layer for front illuminating device geometry. However, the growth of relatively low Al-content $Al_xGa_{1-x}N$ ($x < 0.2$) on bulk GaN substrates can utilize the matured substrate technology with a low defect density of less than 10^6 cm^{-2}. For the realization of these APD devices, growth parameters such as NH_3 flow rate, temperature, aluminum composition, pressure, and growth rate were investigated to overcome more stringent growth conditions for AlGaN on GaN. GaN layer templates on sapphire substrates were employed.

The microscopic morphology as measured by atomic force microscopy (AFM) is compared. The microscopic morphology change of $Al_xGa_{1-x}N$ ($x = 0.2 \sim 0.35$) depending on growth parameters was investigated. Figure 3.25 shows the change of surface morphology in an AlGaN layer as the NH_3 flow rate is changed. The total group III molar flow rate is maintained at approximately 80 μmol/min. With a high NH_3 flow rate, a wavy undulated surface is formed possibly due to limited group III ad-atom mobility on the growing surface. As the NH_3 flow rate decreases from 223.1 mmol/min to 11.2

mmol/min, the surface waviness is reduced and RMS (root mean square) roughness is also decreased. The RMS roughness values are 0.564 and 0.317 nm for NH_3 flow rate of 223.1 mmol/min to 11.2 mmol/min, respectively. Even with relatively smooth surfaces, pits are still observed at the vicinity of merging point of surface waviness. This might be related to pre-existing defect originating from interface between epitaxial layer and sapphire substrate combined with tensile strain of the epitaxial layers. Those defects can be removed by employing high-quality bulk III-Nitride substrates. Figure 3.26 shows surface morphology (1×1 μm^2 scan at z-height of 20 nm) change of AlGaN layers as thickness of AlGaN increases. The layers were grown at the same nominal growth conditions including same molar flow rate of precursors and temperature. Interestingly, for thin layers, aluminum composition becomes higher than thicker layers even with same precursor flow rates and then aluminum composition becomes stabilized. Also, the very wavy surface morphology is observed with higher aluminum composition. This phenomenon becomes more distinctive at relatively higher pressures, for example 200 Torr as in Figure 3.26. When the growth pressure is lower than 75 Torr, the compositional and morphology variation, depending on the thickness of AlGaN layer, becomes negligible. The effect of growth rate on $Al_xGa_{1-x}N$ ($x \sim 0.2$) morphology was studied at the growth pressure of 75 Torr. The growth rate was varied from 0.09 nm/s to 0.32 nm/s. As shown in Figure 3.27, the surface waviness as well as merging points disappear and clear atomic steps are visible at the growth rate of 0.21 nm/s.

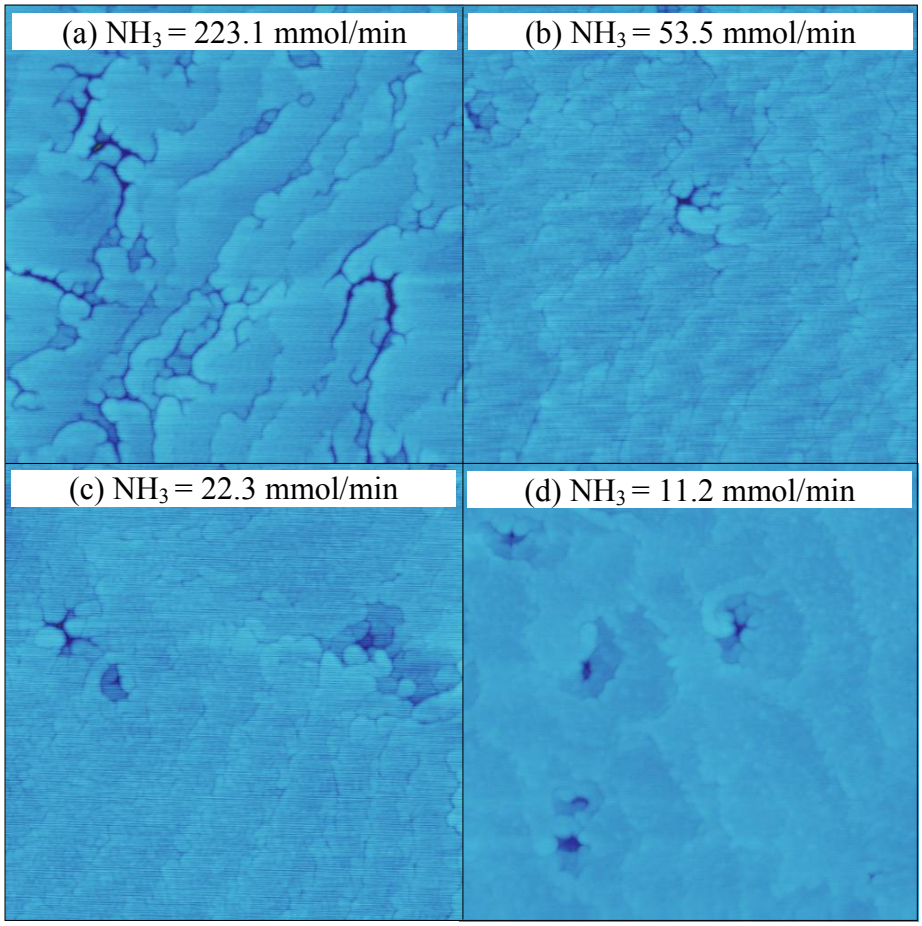

Figure 3.25: Change of microscopic surface morphology (1×1 μm^2 scan with z-height of 20 nm) of AlGaN epitaxial layers with variation of NH3 flow rate.

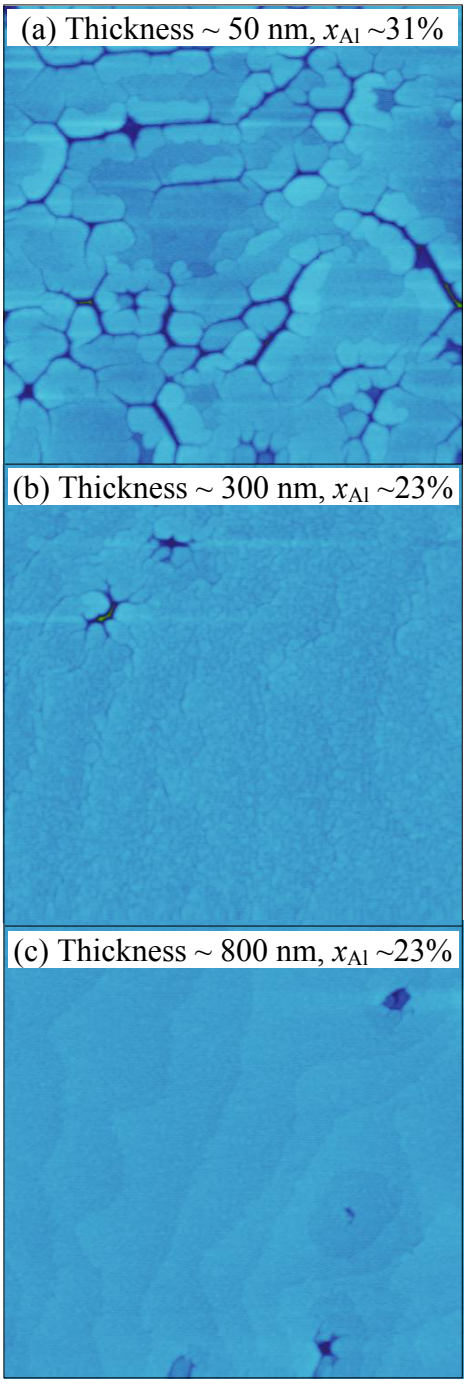

Figure 3.26: Change of microscopic surface morphology (1×1 μm^2 scan) and Al content in AlGaN epitaxial layers with variation of layer thickness.

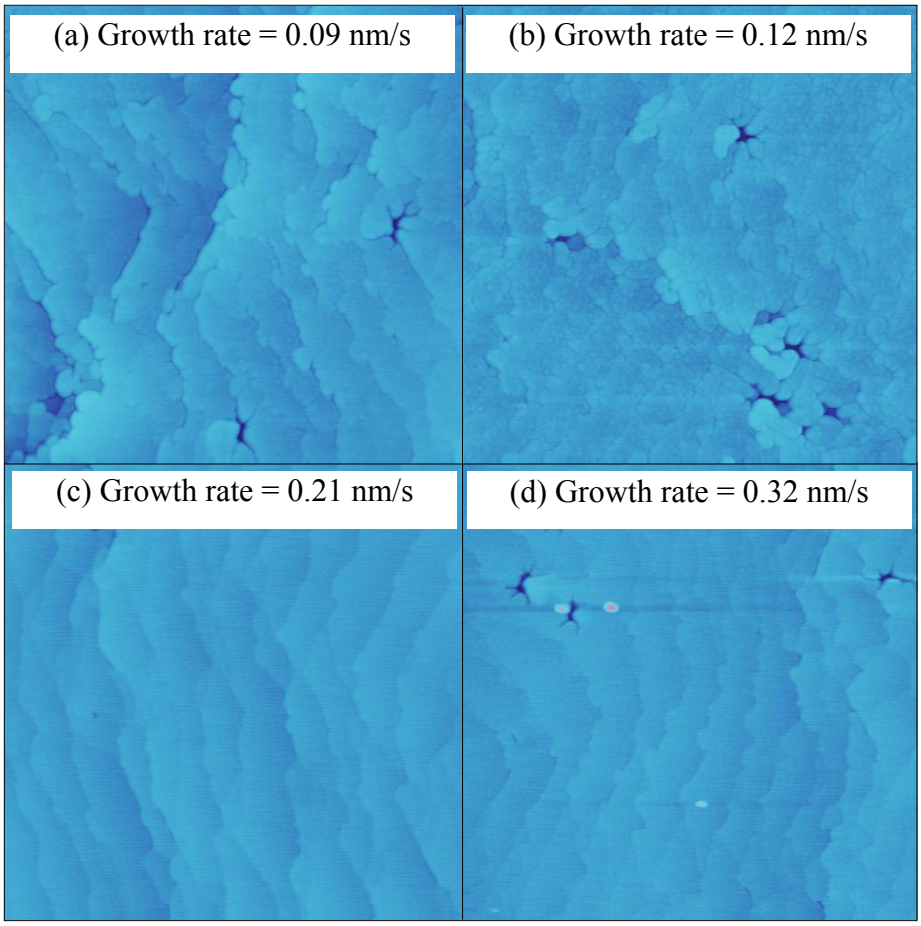

Figure 3.27: Change of microscopic surface morphology (1×1 μm^2 scan) with variation of growth rate.

3.3.4 Strain Management Engineered Epitaxy

During the heteroepitaxy, strain between epitaxial layers or strain induced by the lack of native lattice-matching bulk substrate is unavoidable. Strain plays a significant role in terms of surface morphology, especially for growth of ternary or quaternary alloys such as AlGaN or InAlGaN. Due to in-plane tensile strain for the growth of AlGaN on GaN, the surface morphology is more prone to create a wavy undulated surface feature. The strain-induced cracking is introduced to relieve the strain energy when the thickness of the growing layer goes beyond its critical thickness. The thick AlGaN on GaN was grown to study the effect of strain on the surface morphology. The macroscopic and microscopic morphology determined by Nomarski optical microscope and AFM, respectively, shows two distinctive features on the surface. As shown in Figure 3.28, the Nomarski optical microscope images under the magnification of 500 and 1000 reveal the formation of a crack network on the surface. The detailed analysis of surface morphology by AFM was carried out on the area with the crack network. When the critical thickness is reached, cracks start to propagate to relieve the strain energy and then the continued epitaxial growth makes the difference in surface morphology more significant depending on the region (e.g. crack-free area versus neighboring area adjacent to crack). The surface image taken by a built-in optical microscope is shown together with AFM images in Figure 3.29. AFM surface morphology at neighboring areas of the cracks exhibits a smooth surface with two-dimensional atomic steps while surface morphologies at areas away from the cracks displays awavy, rough surface with micro-pits. As the size of area surrounded by the crack network increases, the surface waviness becomes distinctive and strain-induced pits are observed. RMS roughness values increase with the increase in the size of area determined by the crack network.

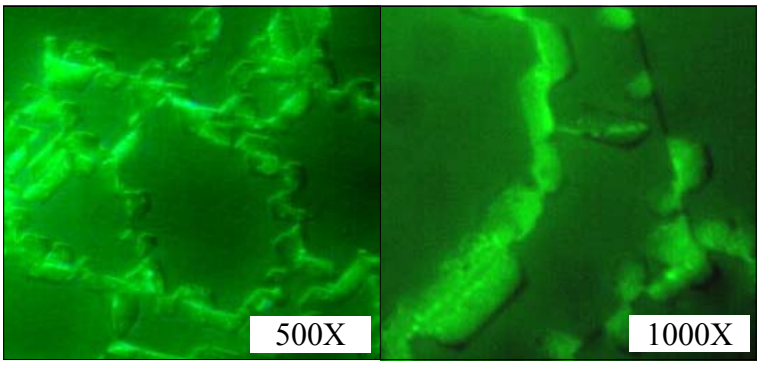

Figure 3.28: Nomarski optical microscope images of AlGaN with crack network.

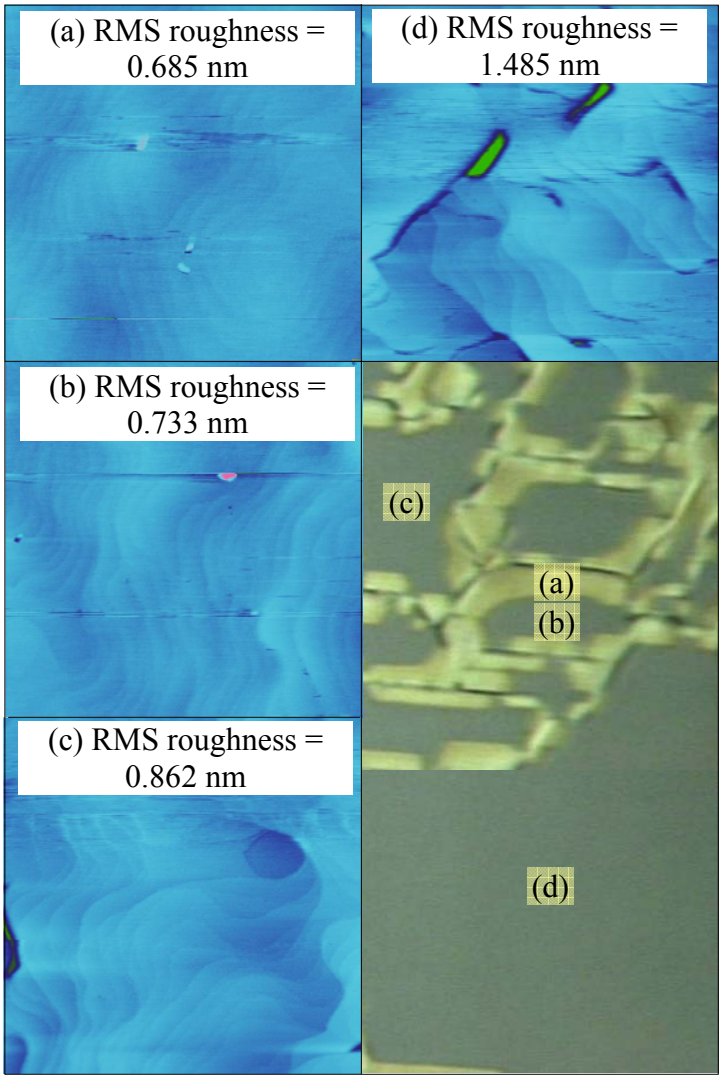

Figure 3.29: AFM microscopic surface morphology of thick AlGaN with crack network.

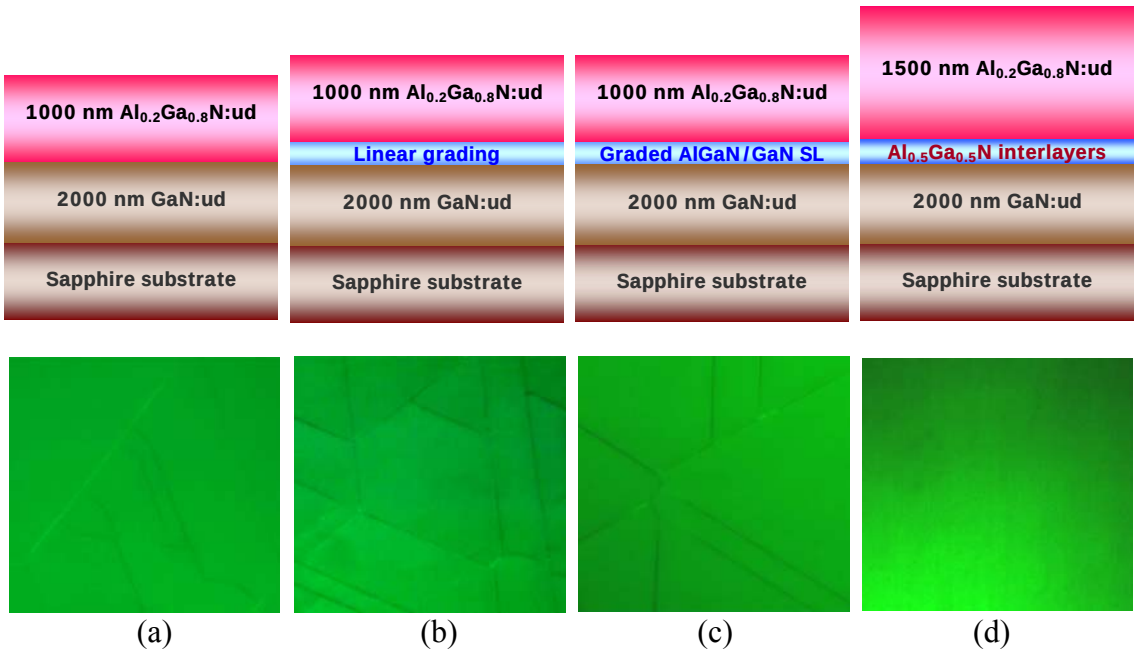

Figure 3.30: Schematic diagram of $Al_{0.2}Ga_{0.8}N$ layers on various strain management design on GaN/sapphire template shown with Nomarski optical microscope images.

The crack-free growth of thick $Al_xGa_{1-x}N$ on a bulk GaN substrate was studied by employing various strain management layers such as $Al_xGa_{1-x}N$ ($x > 0.5$) interlayers, graded $Al_xGa_{1-x}N$/GaN superlattice ($x = 0.05$, 0.1, and 0.15), or AlN/GaN multiple short-period superlattice structures to create a less strained platform for $Al_xGa_{1-x}N$ growth with higher Al-content. For approaches shown in Figures 3.30(a) – (c), the *in-situ* curvature measurement showed an increase in curve distance, indicating that the AlGaN layer experiences concave bowing as the growth proceeds and which results in the formation of cracks on the surface. The growth temperature, thickness, and Al content for interlayers were also studied. $Al_xGa_{1-x}N$ ($x > 0.5$) interlayers with graded $Al_xGa_{1-x}N$ ($0.0 \leq x \leq 0.1$) layers in between enabled the crack-free growth of 1.5 µm-thick $Al_xGa_{1-x}N$ ($x \sim 0.2$) on the GaN/sapphire template shown in Figure 3.30(d). As shown in Figure 3.31, the radius of curvature in km^{-1} during the growth of $Al_xGa_{1-x}N$ ($x \sim 0.2$) with $Al_xGa_{1-x}N$ ($x > 0.5$)

interlayers on GaN showed the increase of only ~ 15 km^{-1}, indicating less bowing for interlayer scheme. AlN/GaN multiple short-period superlattic structures resulted in the increase of radius of curvature over 40 km^{-1} for ~ 700 nm growth of $Al_xGa_{1-x}N$ (x ~ 0.2) and the surface relaxation induced by formation of cracks was observed afterwards. The *in-situ* reflectance spectra reveals the ideal growth mode having constant intensities for both maxima and minima throughout the time of growth of 1.5 μm-thick $Al_xGa_{1-x}N$ (x~0.2).

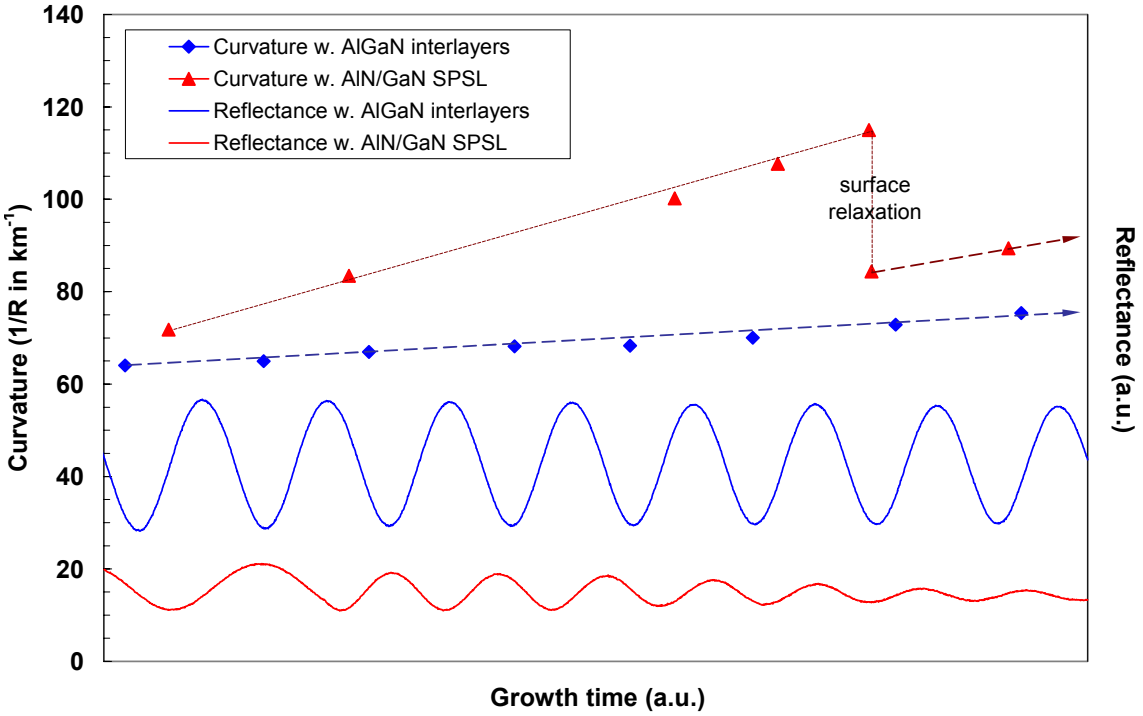

Figure 3.31: *In-situ* reflectance spectra during the growth of $Al_{0.2}Ga_{0.8}N$ on $Al_xGa_{1-x}N$ (x > 0.5) interlayers as strain management layer.

3.3.5 Nitride *p*-type Doping

In the AlGaN/GaN material system, obtaining a reasonable *p*-type doping is difficult due to the high activation energy for p-type dopant. The activation energy for p-type GaN:Mg is approximately 160 meV [68] and it increases by ~ 3 meV as the Al content increases in the material system. For the development of GaN and AlGaN-based UV APDs, the *p*-type doping behavior, depending on various growth conditions, such as growth pressure, growth rate, temperature or V/III ratio, was investigated. From the optimized growth conditions, *p*-type GaN:Mg results in ~ 1×10^{18} cm^{-3} with the mobility (μ_h) of ~ 13 $cm^2/V\cdot s$ from the room-temperature Hall effect measurement. The photoluminescence characteristics of *p*-type GaN:Mg with different doping levels are shown in Figure 3.32.

SIMS depth profiling for the sample shows that the carbon and oxygen impurity levels are well controlled (very low near detection limit) and Mg incorporation into the GaN solid is $4\times10^{19}cm^{-3}$, indicating that ~ 2.5% of the Mg incorporated into GaN is activated as a *p*-type dopant. A transmission line measurement (TLM) study, employing Pd/Au or Ni/Au metallization scheme and no specific high doping scheme contact layer, shows that the specific contact resistance, r_c, of the sample shows 3×10^{-3} $\Omega\cdot cm^2$. The measurement also shows even without the contact layer, the contact of the sample exhibits good ohmic behavior.

The temperature-variable Hall-effect measurement was carried out using the Hall measurement system in Phillips Lumileds Lighting. The activation energy of GaN:Mg *p*-doping was calculated. Figure 3.33 shows the variable-temperature Hall data of the GaN:Mg layer: (a) shows temperature (1000/T) vs. free-carrier concentration plot and (b) shows temperature (T) vs. mobility plot. At 300K, the sample exhibits free hole concentration (p) of ~ 1.36×10^{18} cm^{-3} with mobility (μ_h) ~ 3.39 $cm^2/V\cdot s$. The resistivity of the layer (ρ) is 0.73 $\Omega\cdot cm$. From the gradient of temperature (1000/T) versus free-

carrier concentration plot, ~170 meV of activation energy is obtained, which is close to the value reported for GaN:Mg activation for *p*-type doping.[68]

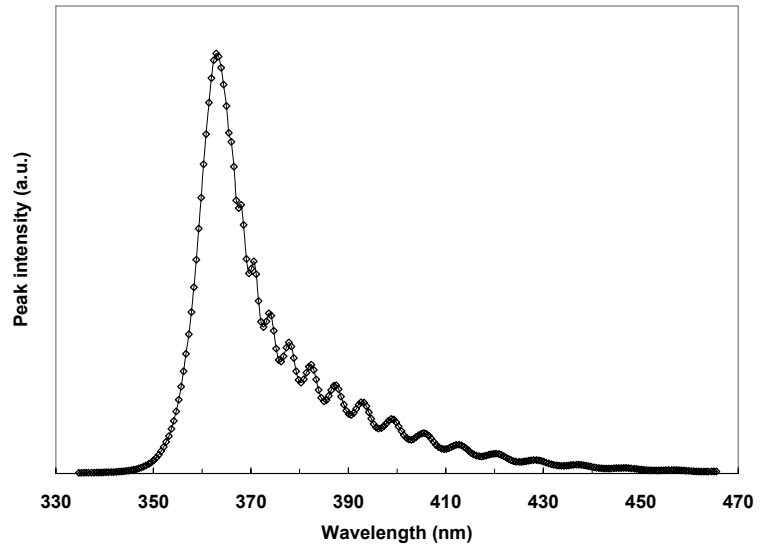

(a)

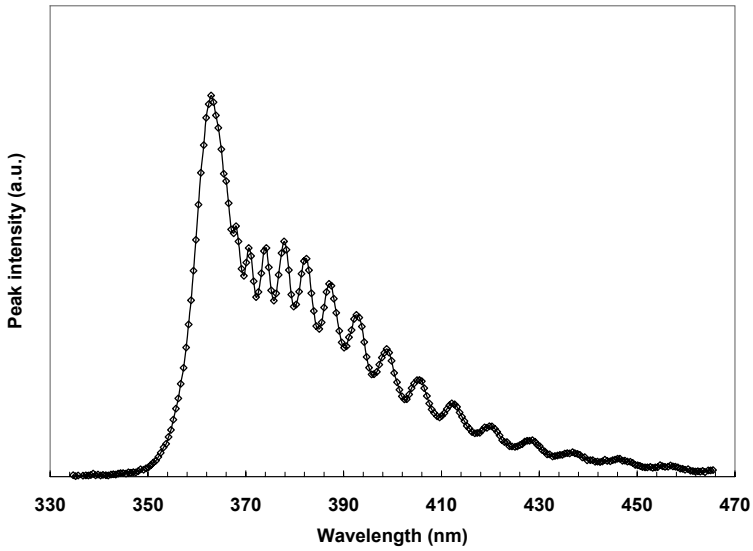

(b)

Figure 3.32: Photoluminescence characteristics of *p*-type GaN:Mg samples: (a) before activation (b) after activation.

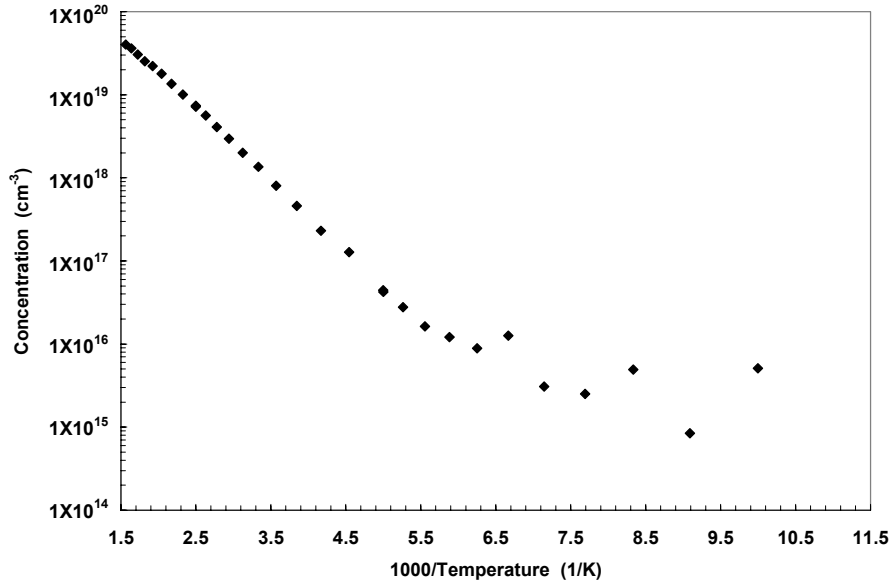

(a)

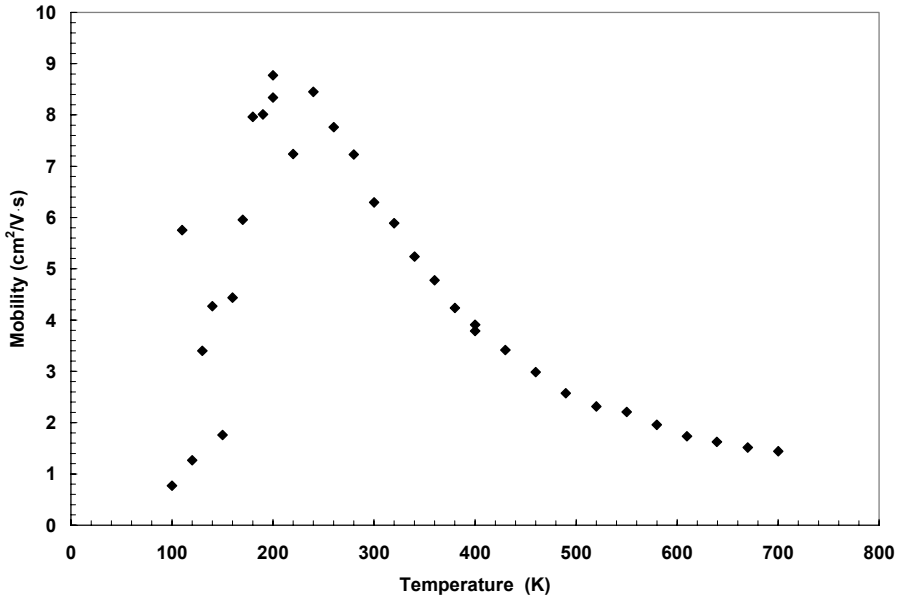

(b)

Figure 3.33: Variable-temperature Hall data of GaN:Mg layer (1μm-thick): (a) temperature (1000/T) vs. free-carrier concentration (b) temperature (T) vs. mobility.

For *p*-type doping for $Al_xGa_{1-x}N$ (x~0.2), we studied growth parameters such as NH_3 flow rate, growth temperature, and aluminum composition, pressure, and growth rate. Multiple sets of *p*-$Al_xGa_{1-x}N$:Mg samples were grown under various growth conditions for the Hall-effect measurement. A heavily doped thin *p*-GaN:Mg^{++} contact layer was introduced to achieve the excellent ohmic behavior of samples. Figure 3.34 shows the microscopic surface morphology of *p*-type $Al_xGa_{1-x}N$:Mg (x~0.2) grown at optimized growth parameters, revealing atomic steps from two-dimensional growth mode. The electrical properties of the *p*-AlGaN:Mg^{+} layer obtained by a 300K Hall-effect measurement are summarized in Table 3.9.

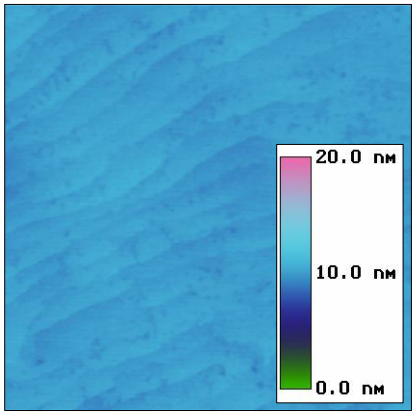

Figure 3.34: Microscopic surface morphology by AFM of *p*-type $Al_xGa_{1-x}N$:Mg ($x \sim 0.2$) grown on GaN on sapphire template (1×1 μm^2 scan).

Table 3.9: Electrical properties of *p*-$Al_xGa_{1-x}N$:Mg^{+} ($x_{Al} \sim 0.2$) layer by 300K Hall effect measurement.

Growth pressure (Torr)	75
x_{Al}	~ 0.2
Bulk [Ω·cm]	9.1
p [cm^{-3}]	1.6×10^{17}
μ [cm^2/V·s]	4.4

The *p*-type AlGaN:Mg layers with higher Al-content (x_{Al} of 0.05 ~ 0.5) grown on AlN on sapphire templates for AlGaN APDs on bulk AlN substrates were also calibrated. Growth parameters such as precursor flow rates (Cp_2Mg and TMGa), growth rate, or V/III ratio were investigated. Multiple sets of *p*-$Al_xGa_{1-x}N$:Mg samples were grown under various growth conditions for the Hall-effect measurement. The epitaxial structures consist of *p*-GaN:Mg^{++} contact layer (20 nm), *p*-AlGaN:Mg^{+} layer (250 ~ 500 nm), AlGaN:ud layer, and AlN buffer layers on sapphire substrates. *p*-GaN:Mg^{++} contact layer was introduced to achieve the excellent ohmic behavior of the sample for Hall-effect measurement. It was also verified that 20 ~ 30 nm *p*-GaN:Mg^{++} contact layer does not affect the bulk resistance of a thick conducting *p*-AlGaN:Mg^{+} layer with low Al composition. Table 3.10 shows the electrical properties of *p*-AlGaN:Mg^{+} layers obtained by 300K Hall effect measurements. *p*-AlGaN:Mg^{+} layers grown on GaN on sapphire templates are also shown together as comparison. As x_{Al} increases, the resistance increases and the mobility decreases, as expected. For free hole concentration, as x_{Al} increases, free carrier concentration decreases in general, even though sample C (x_{Al} ~ 0.4) has slightly higher concentration than Sample B (x_{Al} ~ 0.1). The unexpected trend of free carrier concentration will be investigated using a temperature-variable Hall-effect measurement. The calibration for *p*-type $Al_xGa_{1-x}N$:Mg with x_{Al} of 0.05 ~ 0.5 is to achieve *p*-type doping with transparency to UV as high as possible. Figure 3.35 shows the optical transmittance spectra of *p*-$Al_xGa_{1-x}N$:Mg^{+} (x_{Al} ~ 0.4) layers with different *p*-type precursor flow rates ($R_1 > R_2 > R_3$) on AlN template/sapphire substrates. Two points per each sample around the center of the wafer were measured. The transmittance decreases slightly by *p*-GaN:Mg^{++} contact layer, but the bottom edge of overall transmittance cut-off occurs at 265 nm, which can allow the peak UV absorption at the solar-blind spectral region of ~ 280 nm for *p*-type $Al_xGa_{1-x}N$:Mg layer.

Table 3.10: Electrical properties of *p*-AlGaN:Mg^{+} layers obtained by 300K Hall effect measurement.

Sample #	x_{Al}	Pressure [Torr]	R_g [nm/s]	Bulk [Ω·cm]	p [cm^{-3}]	μ [cm^2/V·s]
A	0.05	200	0.496	1.8	4.6×10^{17}	7.8
B	0.1	200	0.306	3.2	2.9×10^{17}	5.0
C	0.4	75	0.127	8.9	3.2×10^{17}	2.2
D	0.5	75	0.135	39.5	1.3×10^{17}	1.3

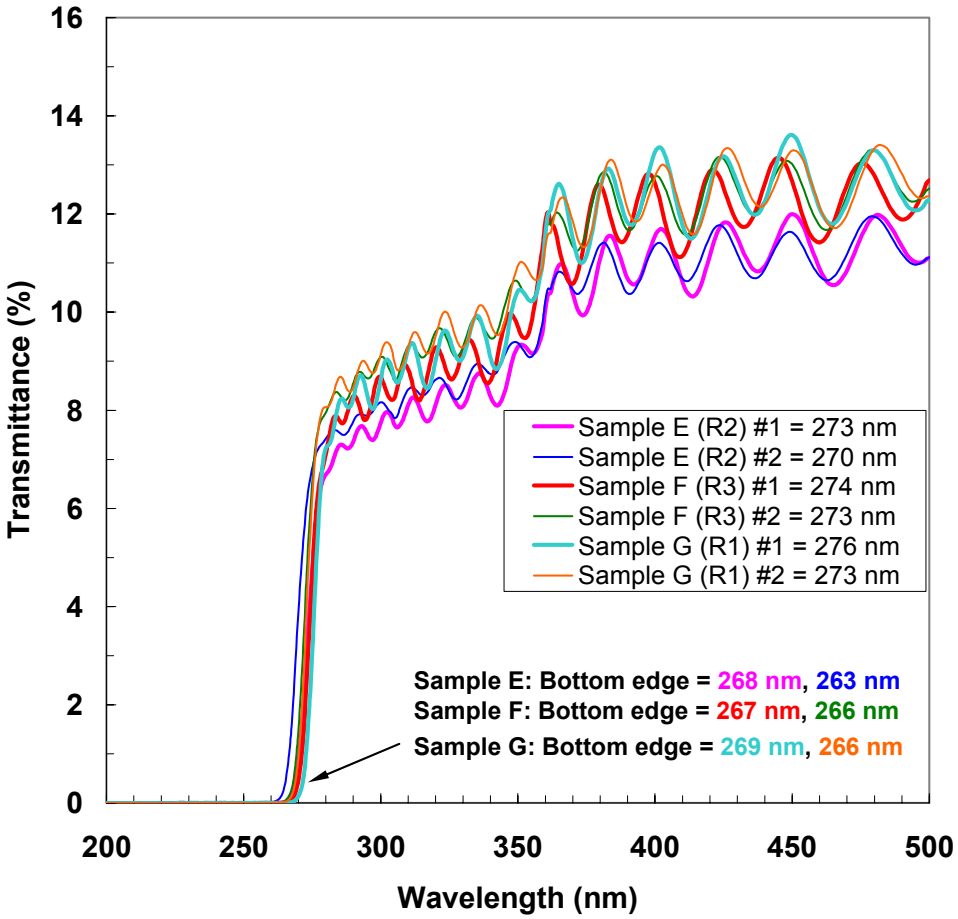

Figure 3.35: Optical transmittance spectra of *p*-$Al_xGa_{1-x}N$:Mg^{+} (x_{Al}~0.4) layer grown on AlN template/sapphire substrate under various Cp_2Mg flow rates.

For low Al composition samples ($x_{Al} \leq 0.1$), 300K Hall shows $p \sim 4.3\times10^{17}$ with $\mu_h \sim 5.95$ for $x_{Al} \sim 0.05$ from the temperature variable Hall measurement (performed by Phillipd Lumileds Lighting). Free carrier concentration vs. reciprocal temperature (1000/T) shows the typical Arrhenius equation relation (as temperature increases, the free carrier concentration increases exponentially). From the gradient of the plot, the ionization activation energy, E_a of 195 meV is obtained, as shown in Figure 3.36, which is close to the previously reported value.

Such contact layer or some other defect-related transport might be suspected to play a role in the measurement, since the layer of interest with high Al composition may have very limited conductivities. To avoid the effect of p-GaN:Mg^{++} contact layers, the p-GaN:Mg^{++} contact layer for the area not covered by metal contacts was removed. This was done by ICP etching of the contact layer by using Pd/Au metal pad as an etch mask so that the removal of the p-GaN:Mg^{++} layer without sacrificing ohmic contact for the measurement was possible. The result of temperature-variable Hall measurement will be reported in the future.

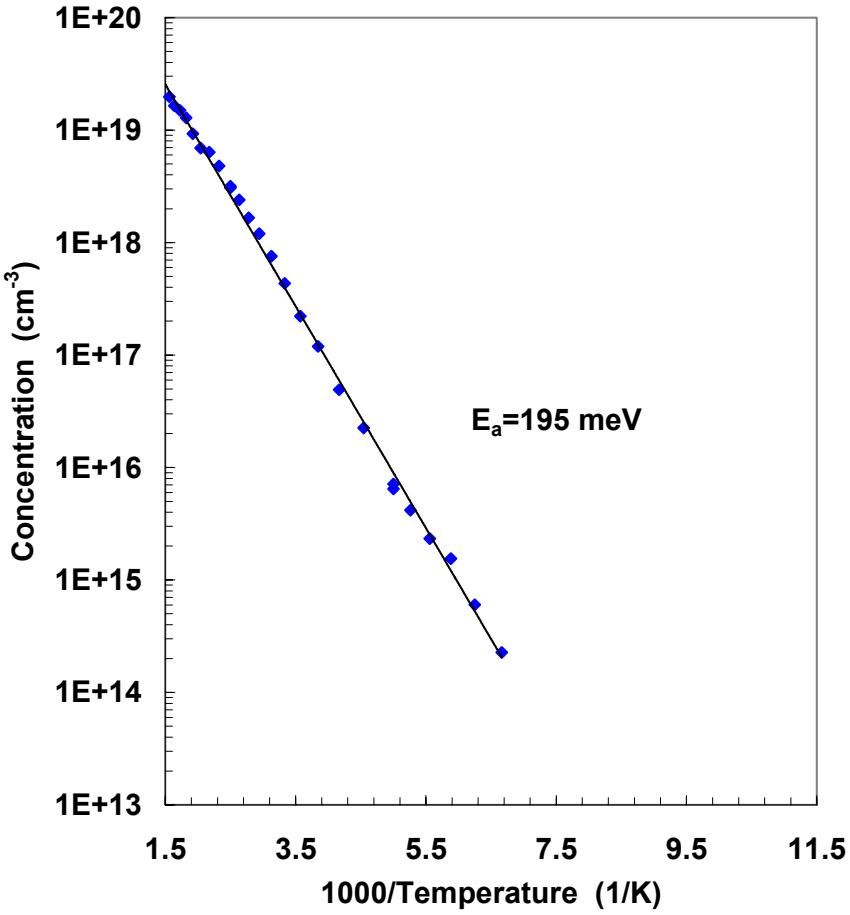

Figure 3.36: Free carrier concentration change taken by temperature-variable Hall measurement from p-$Al_xGa_{1-x}N$:Mg^+ ($x_{Al} \sim 0.05$) layer.

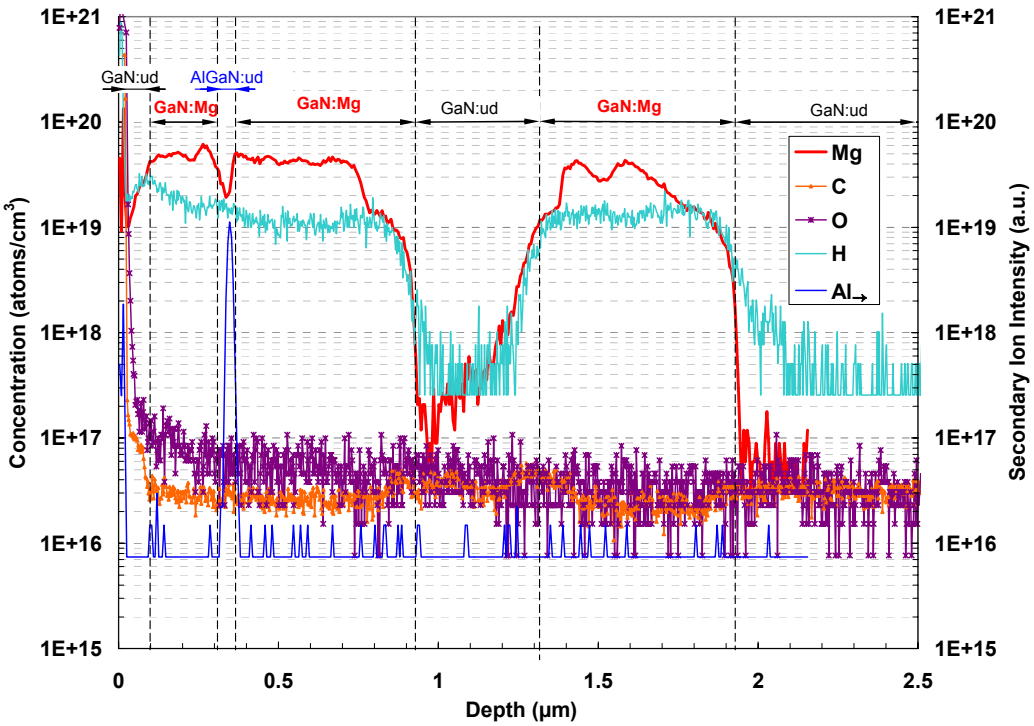

Figure 3.37: SIMS profile of the sample consisting of GaN:Mg and GaN:ud layers for Mg memory effect and diffusion study.

p-type AlGaN:Mg layers for UV APDs are relatively thin (< 100 nm) in comparison to other device structures. Hence, AlGaN:Mg layers in APDs can have several technical challenges. First, there is low free carrier concentration due to the high ionization activation energy of Mg and second, there is less than the estimated *p*-type dopant incorporation; therefore, lower free hole carrier concentration is introduced by the delayed Mg incorporation into the lattice due to the memory effect and Mg diffusion into the active region. The SIMS profile of Mg concentration shows grading up in the thin *p*-GaN layer (~100 nm) as epitaxial growth proceeds even though the same precursor input of all the group III (TMGa and TMAl), group V (NH_3), and *p*-type dopant (Cp_2Mg) during the growth of *p*-AlGaN:Mg were applied. To study the Mg behavior in the lattice

during the epitaxial growth, SIMS and Hall measurement analysis were carried out. The structure was designed and grown for SIMS analysis to study the memory effect and diffusion of Mg, consisting of, in the order of growth sequence, GaN:ud, *p*-GaN:Mg (*p*-layer #1), GaN:ud, , *p*-GaN:Mg (*p*-layer #2), AlGaN:ud, , *p*-GaN:Mg (*p*-layer #3), and GaN:ud. Figure 3.37 shows the depth profiling of the structure. To trace the origin of Mg grading-up observed in other device structures, several Mg doped layers were grown with an undoped maker layer. In comparing *p*-layer #1 with *p*-layer #2, the layers exhibit similar "slow turn-on" behavior after Mg precursor starts flowing. If the diffusion effect dominates the Mg profile (sharp profile for initial growth and diffuse out along the concentration gradient), the layers have different profiles, with *p*-layer #1 displaying longer tail than *p*-layer #2. The origin of "slow turn-on" behavior is considered to be dominated by the memory effect of the Mg precursor. The slow turn-on effect spans over 1 μm under the current reactor system and growth condition, suggesting that the Mg incorporation and free carrier concentration of *p*-type layer in the actual device structures may not be equivalent to those of relatively thick calibration samples with optimized growth conditions (> 0.5 μm). Also, for the *p*-layer #1, slow turn-off was observed, which can be interpreted as reverse process of slow turn-on induced by the memory effect; hence, Mg grading for *p*-GaN:Mg observed in Figure 3.37 can be originated from memory effect – Mg incorporation into the lattice is delayed during the thin layer of *p*-layer growth. To investigate the effect of slow delayed incorporation of Mg on electrical property of the *p*-type layer, Hall-effect measurement of *p*-GaN:Mg samples with different thicknesses (0.1 μm and 1 μm) are compared. The thinner sample (0.1 μm) shows lower free hole concentration by the factor of two – $\sim 5\times10^{17}$ cm^{-3} for 0.1 μm sample while $\sim 1\times10^{18}$ cm^{-3} for 1 μm sample, which is considered to be due to insufficient Mg incorporation during thin layer growth due to the memory effect.

The growth calibration and characterization for $Al_{0.25}Ga_{0.75}N$/GaN short-period superlattice (SPSL) for the use of *p*-type hole injection layer of UV APDs was carried out

to utilize the potential improvement of (1) carrier concentration by lowering Mg acceptor ionization activation energy (reported to be approximately 58 meV [82]) and (2) current spreading in *p*-type $Al_xGa_{1-x}N$:Mg/GaN:Mg SPSLs. As SPSL grows thicker, there can be "thickness chirping" which means the thickness and period of the SPSL changes as the number of layers increase during the growth. Figure 3.38 shows cross-sectional scanning transmission electron microscopy (STEM) high angle annular dark field (HAADF) images of the SPSLs from different locations of SPSL stacks. The results show none of the thickness variations from bottom to top of the wafer, demonstrating well-established growth conditions. TEM analysis of 300-period $Al_{0.25}Ga_{0.75}N$/GaN SPSLs exhibits approximately 1.5 nm and 3.2 nm of $Al_{0.25}Ga_{0.75}N$ and GaN layer thickness, respectively, which are very close to those determined by XRD.

The layer thicknesses are well matched to the estimated thicknesses. HAADF intensity profiles from four heights of the SPSL stacks are plotted together with offset in Figure 3.39. The oscillations in the graph represent the 0001 fringes. No noticeable changes in the thicknesses and intensities of AlGaN and GaN layer are observed in the profiles from bottom to top of the stack, indicating that the interface quality and compositions of the superlattices maintain the same periodicity as the number of stacks increase.

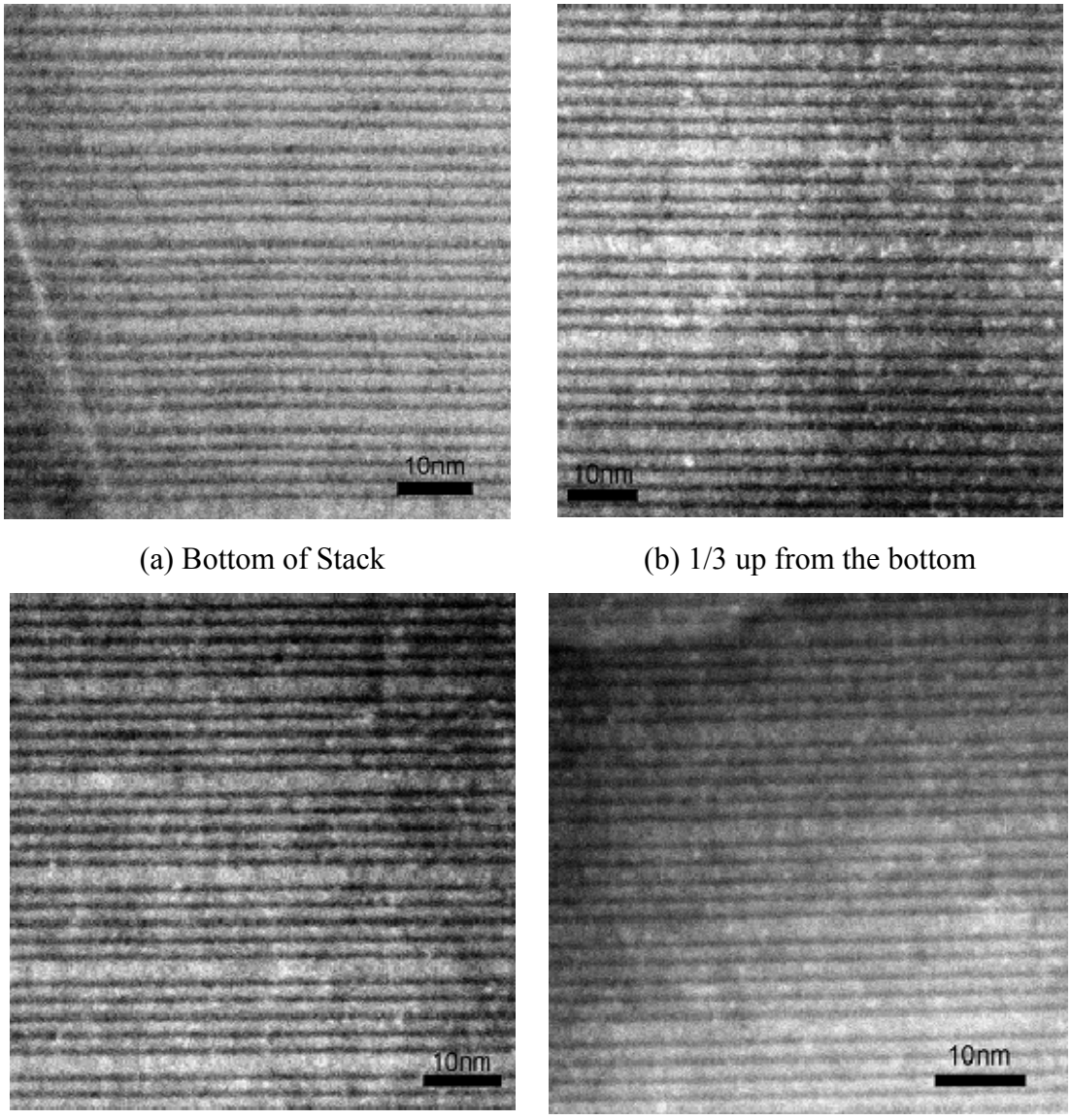

(a) Bottom of Stack

(b) 1/3 up from the bottom

(c) 2/3 up from the bottom

(d) Top of Stack

Figure 3.38: Cross-sectional scanning transmission electron microscopy high angle annular dark field (HAADF) images of the 300-period SPSLs having ~ 1.5 nm and ~ 3.2 nm of $Al_{0.25}Ga_{0.75}N$ and GaN layers from different locations of SL stacks.

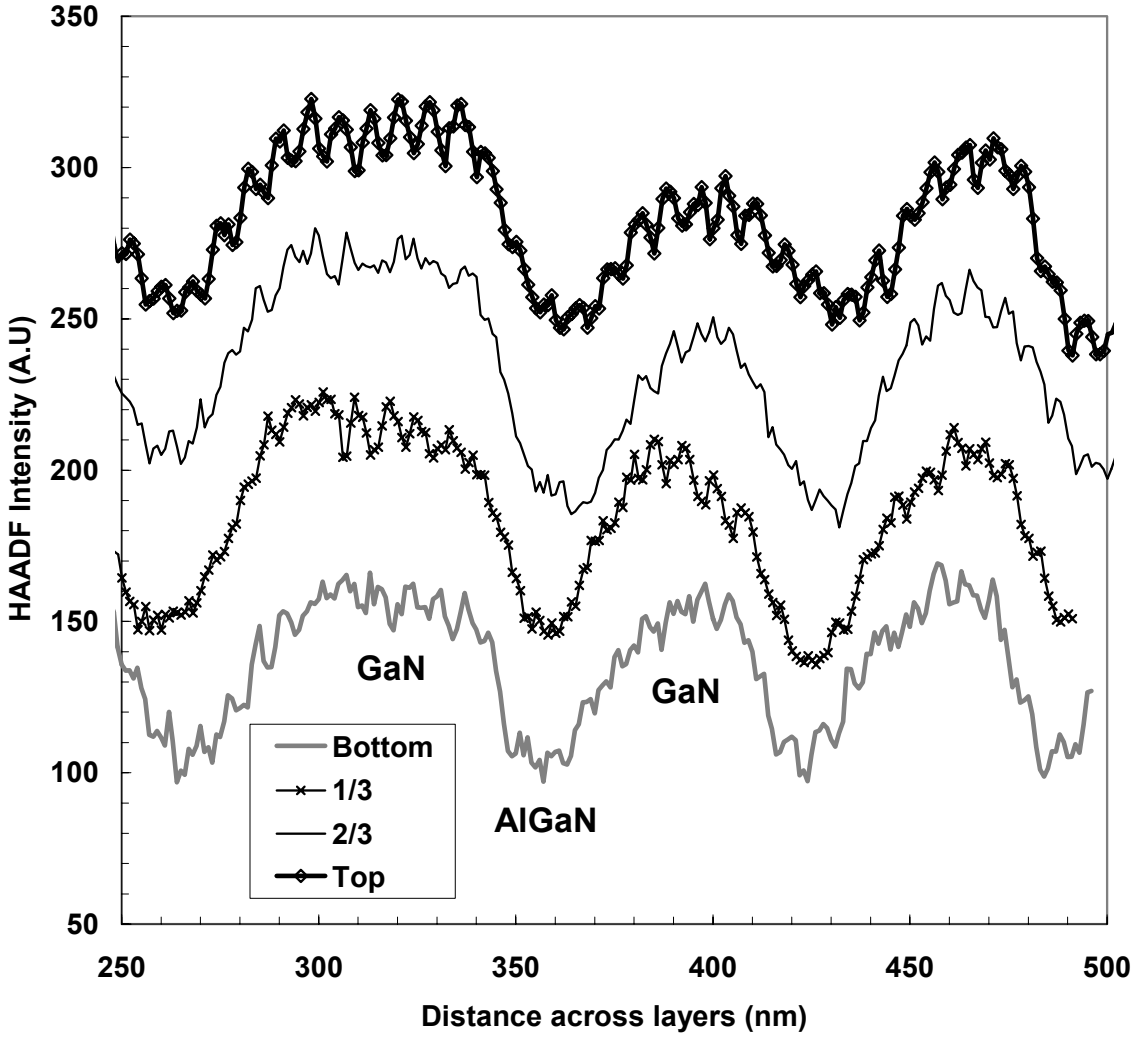

Figure 3.39: High angle annular dark field (HAADF) intensity profile of the 300-period SPSLs from different locations of SL stacks.

3.4 GaN *p-i-n* APD on bulk GaN substrates

Using the epitaxial material development discussed earlier in this chapter, high performance GaN *p-i-n* APDs were grown and fabricated. To minimize the dislocation density in the device structure which has hampered the realization of GaN APDs, the low dislocation density (~10^5-10^6 cm^{-2}) *n*-type bulk GaN substrates that were grown by hydride vapor phase epitaxy (HVPE) was used as a substrate. The low dislocation density in the devices enables low reverse-bias dark current densities, high sensitivities and high optical gains in the ultraviolet (UV) spectral region prior to avalanche breakdown for 30 μm-diameter-mesa photodiodes. The growth conditions for epitaxial layers were optimized, to achieve the improved crystalline and the structural quality, by altering the growth parameters. GaN *p-i-n* APD structures consist of a 2.5 μm-thick *n*-type GaN:Si layer, followed by a 0.3 μm-thick, unintentionally doped (estimated $n = 5\times10^{16}$ cm^{-3}) GaN *i*-type drift region, and topped with a 0.1 μm-thick *p*-type GaN:Mg layer and 0.02 μm-thick *p*-type heavily doped GaN:Mg^{++} contact layer as shown in Table 3.11. The electrical properties of the GaN:Mg^{+} layer, including the free-hole concentration, mobility, and electrical resistivity, were measured for GaN films produced under various growth conditions.[83] The 300 K free-hole concentration in the *p*-layer was estimated to be p~1×10^{18} cm^{-3} as determined by Hall-effect measurements carried out for *p*-GaN:Mg^{+} layers grown on undoped GaN/sapphire substrates with the same growth conditions as were applied to the UV APD structures grown on GaN substrates.

Table 3.11: Composition, doping, and thickness of the layers of a GaN APD.

Layer	Composition	Thickness (μm)	Doping (cm^{-3})
p-contact	GaN:Mg^{++}	0.02	[Mg] = ~2×10^{20}
p-layer	GaN:Mg^{+}	0.1	$p = 1\times10^{18}$
i-layer	GaN:ud	0.3	$n = 5\times10^{16}$
n-layer	GaN:Si^{+}	2.5	$n = 5\times10^{18}$
Substrate	bulk GaN	~ 450	n ~ 5×10^{18}

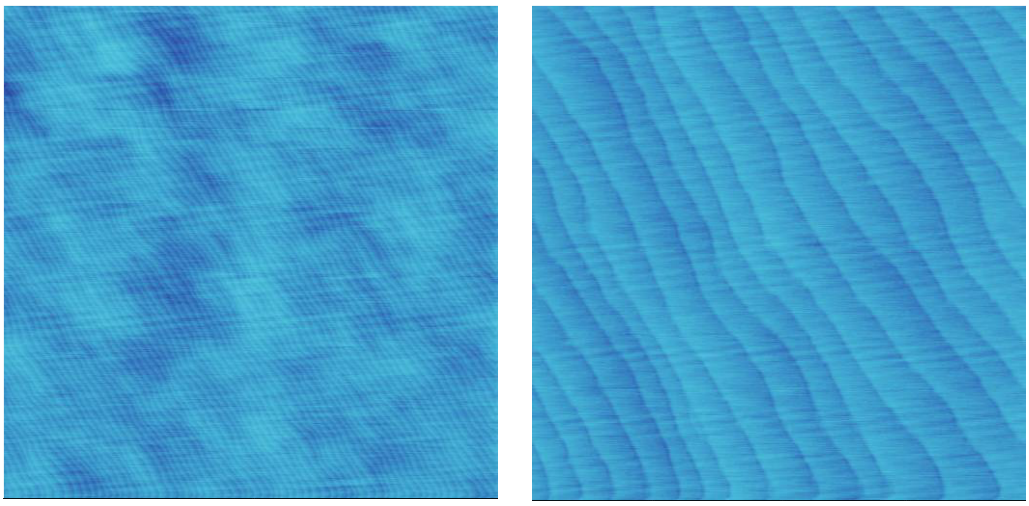

(a) (b)

Figure 3.40: Microscopic surface morphology of a GaN *p-i-n* avalanche photodiode structure on a bulk (0001) GaN substrate measured by AFM.

X-ray diffraction (XRD) rocking curve and atomic force microscopy (AFM) analyses were employed to characterize the properties of the epitaxial structures as well as the GaN substrates prior to growth. Figure 3.40 shows the AFM image of the surface of a GaN UVAPD wafer, with 5×5 μm^2 and 1×1 μm^2 scan and z-height scale of 10 nm, revealing atomic steps on the surface with no visible nano-pits and RMS roughness values of 0.29 nm and 0.22 nm for 5×5 μm^2 and 1×1 μm^2 scans, respectively. The linewidth of the XRD rocking curve of the epitaxial layer nearly replicates the linewidth of the GaN substrate.

The devices were processed into 30 μm- and 50 μm-diameter circular mesas by inductively coupled plasma (ICP) etching using a Cl_2/He carrier gas mixture. A scanning electron microscope (SEM) image of a fabricated 30μm-diameter mesa device without a contact probe pad is shown in Figure 3.41. After mesa definition, a SiO_2 passivation layer was applied to the devices using plasma-enhanced chemical vapor deposition. Ti/Al/Ti/Au and Pd/Au Ohmic contacts were evaporated on the *n*-layer and *p*-layer,

respectively, and annealed at 600˚C in a N_2 ambient. The width of the ring-shaped *p*-contact metal is 5 μm. No attempt to taper the mesa-wall edge profile was made.

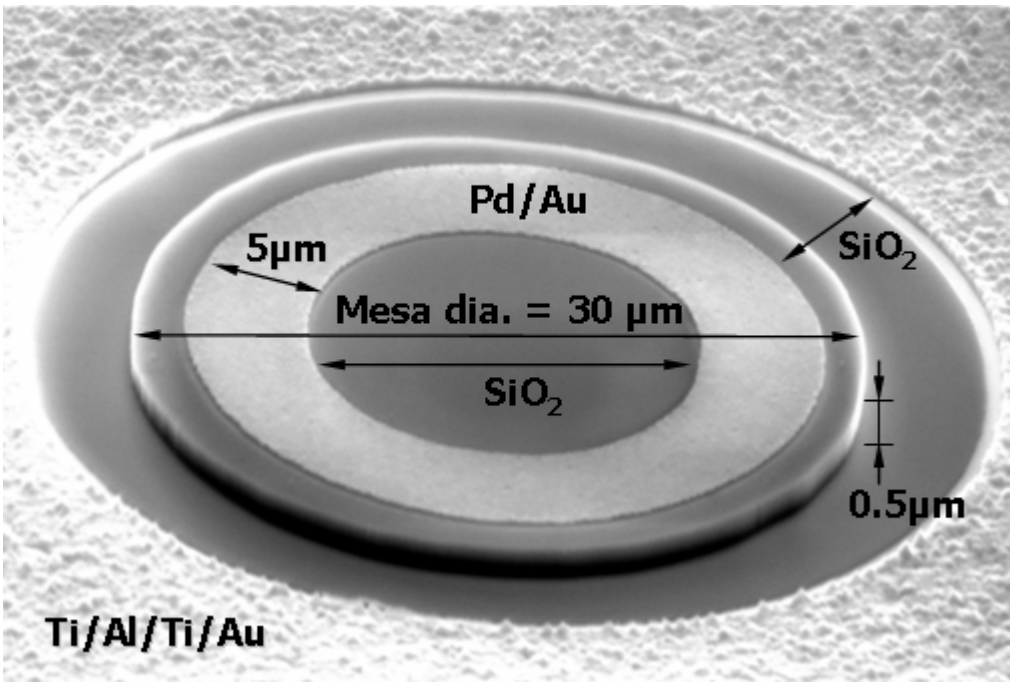

Figure 3.41: SEM image of a fabricated 30μm-diameter GaN *p-i-n* APD device.

Typically, the reverse-bias breakdown voltage, V_{BR}, of the 30 μm-diameter devices was between 80 V and 90 V, as measured on a probe station by an Agilent Model 4156C Semiconductor Parameter Analyzer. Figure 3.42 shows the reverse-bias current-voltage (*I-V*) characteristics of a 30 μm-diameter mesa device measured in the dark at room temperature (300 K), showing a testing-system-limited low-reverse-voltage ($|V_R| <$ 60 V) dark current and current density of $I_R = 5\times10^{-14}$ A and $J_R = 7.0\times10^{-9}$ A/cm^2, respectively, and values of $I_R = 2\times10^{-11}$ A and $J_R = 2.8\times10^{-6}$ A/cm^2 at $V_R \sim$ -82 V, just before breakdown ($V_{BR} \sim$ -83 V). To confirm avalanche breakdown, the temperature-dependent reverse-bias *I-V* characteristics were measured. The magnitude of the reverse-bias breakdown voltage, $|V_{BR}|$, showed a clear positive increase with an increase in

temperature. For temperatures of 313 K, 333 K and 353 K, the corresponding values of $|V_{BR}|$ were 86 V, 87 V and 88 V respectively as shown in Figure 3.43. From this, we can estimate the temperature coefficient of the breakdown voltage to be ~0.05 V/K. The positive temperature dependence of the magnitude of the breakdown voltage confirms that the abrupt increase in reverse current is predominantly due to avalanche effects, and not by premature junction breakdown due to microplasmas or mesa-sidewall leakage paths. In addition, GaN APDs rolled into consistent breakdown voltage with the same leakage current characteristics at room temperature for 40 times when multiple reverse-bias *I-V* scans were applied.

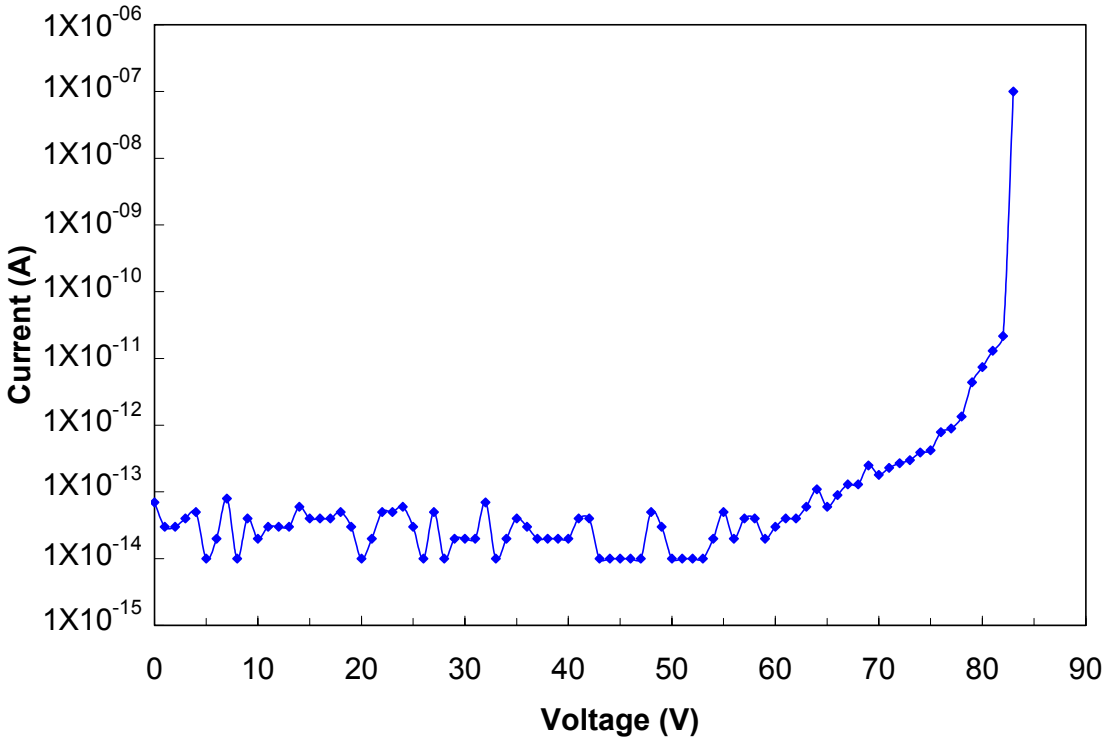

Figure 3.42: Reverse-bias dark-current characteristics of a GaN APD having a circular mesa of 30 μm diameter, showing a low dark current and current density of 2×10^{-11} A and 3.5×10^{-6} A/cm^2 respectively, at a reverse bias ~ 82 V.

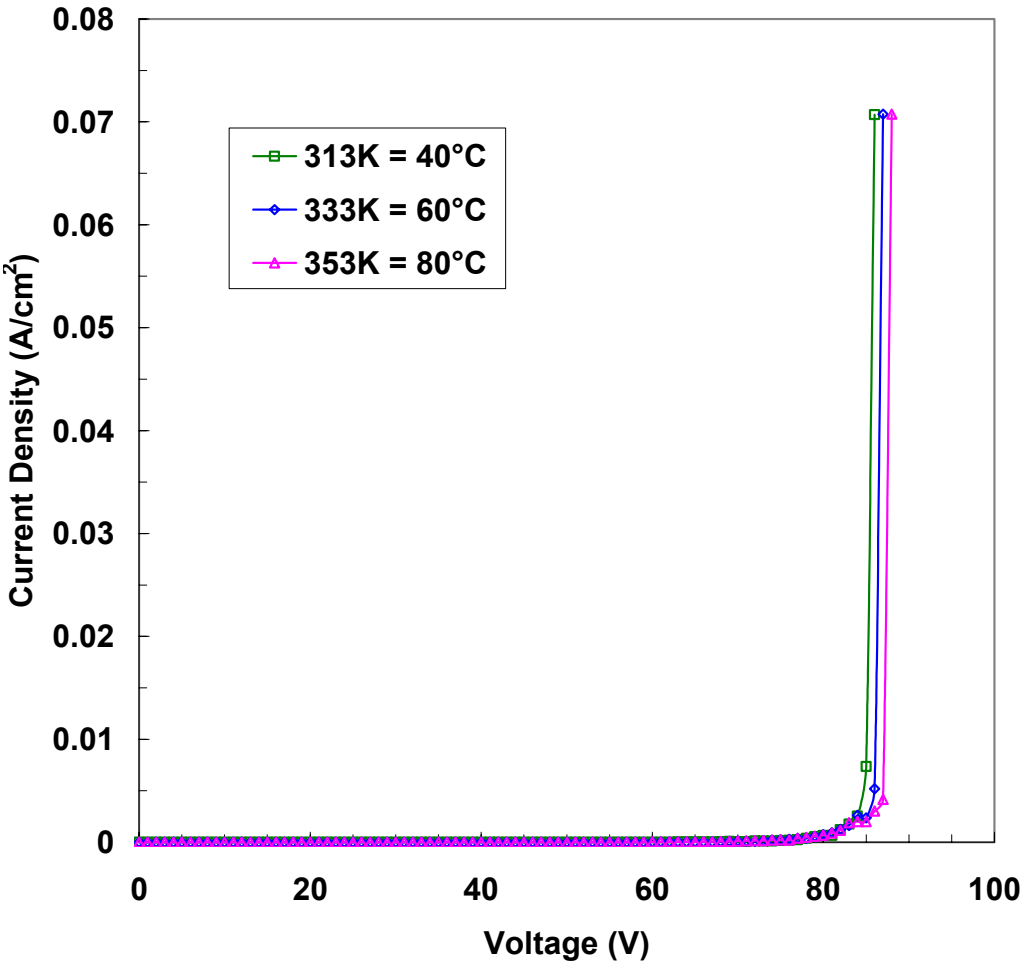

Figure 3.43: Temperature-dependent reverse-bias *I-V* characteristics measured at 313 K, 333 K, and 353 K.

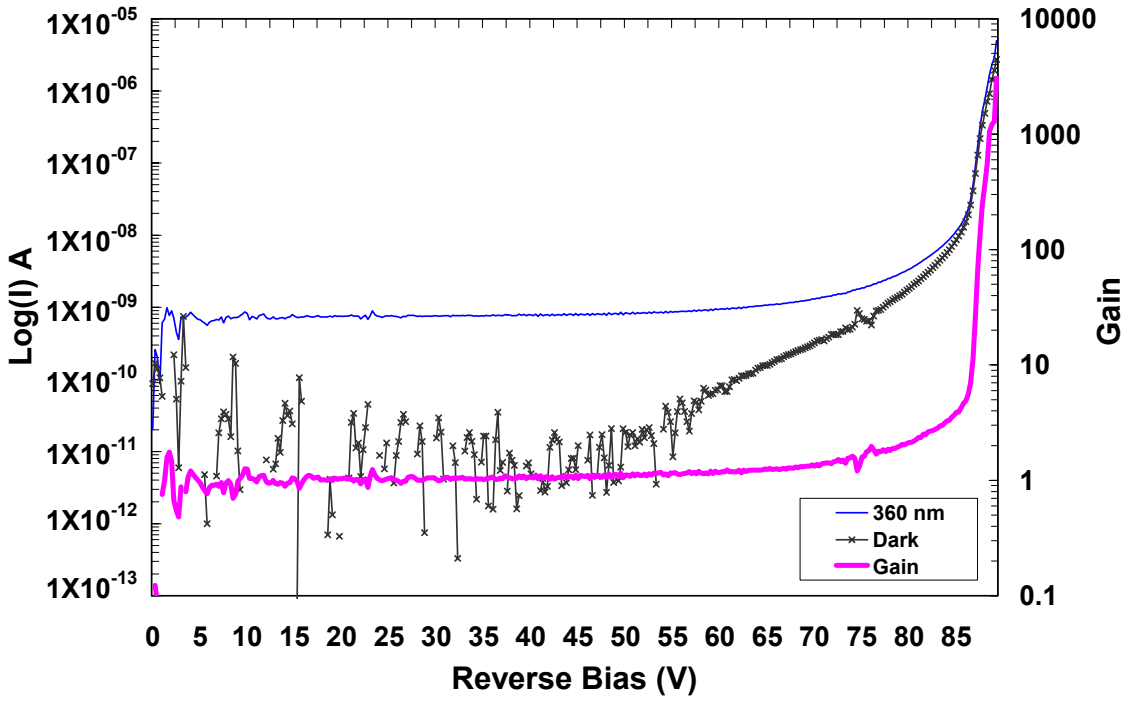

Figure 3.44: Reverse-bias *I-V* characteristics of a GaN APD having a mesa diameter of 50 µm. The dark current, photocurrent, and avalanche gain (*M*) are plotted versus reverse bias voltage. The diode shows gain in excess of $M \sim 10$ at the onset of avalanche breakdown (-86.5 V, electric field of ~2.8 MV/cm), reaching a maximum avalanche gain of ~ 3,000.

Figure 3.44 shows a comparison of the photocurrent and dark-current characteristics at room-temperature for a 50 µm-diameter mesa UV APD measured by Dr. Chuck Collins at the U.S. Army Research Laboratory. No microplasma or edge breakdown emission was visually observed and many of the tested devices rolled into breakdown consistently (for over 40 scans) over all wavelengths (280 nm ~ 365 nm) tested, suggesting that no microplasmas were formed. Hence, edge gain and microplasma-related gain are not considered in the calculation of the avalanche gain for these devices. The data in Figure 3.44 were obtained using a UV lamp-monochromator combination operating at a peak emission wavelength of ~ 360 nm and a spectral width

of ~ 3 nm. The avalanche gain (M) is taken as the difference between the reverse-biased photocurrent and dark current, divided by the difference between the low-bias photocurrent and low-bias dark current. The low-bias currents are taken from the flat portion of the *I-V* curves for reverse voltages less than 60 V. In this low-applied-bias regime ($|V_R| < 60$ V), the difference between the photocurrent and dark current can be approximated as the photocurrent since the dark current is significantly lower. The photocurrent is almost constant without soft breakdown for the low-reverse-bias regime, and used as the normalization factor for calculating avalanche gain, i.e., as the unity-gain photocurrent. The device exhibits an avalanche gain of over ~ 10 at the onset of breakdown of V_{BR} = -86.5 V (electric field ~2.8 MV/cm), reaching a maximum avalanche gain of ~ 3,000. The measured reverse-bias photocurrent gain is considered to be originated from the avalanche multiplication of photogenerated carriers in the drift region. Achieved in 2006, this was the highest true avalanche gain achieved for photodiodes based on the GaN material system. The very high avalanche gain for large-area GaN UVAPD is partially attributable to the low defect density of the material; however, the fact that these devices exhibited stable avalanche breakdown in spite of the relatively sharp vertical sidewalls suggests that the low plasma-induced etch damage of the mesa, and the high-quality dielectric passivation also played a role.

The growth of GaN *p-i-n* APDs on bulk GaN substrates with contact probe pads based on further epitaxial optimization was performed for a Geiger mode demonstration. The processing and measurement work was done in Dr. Shyh-Chiang Shen's laboratory at Georgia Institute of Technology. The SEM image of a fabricated GaN *p-i-n* APD device with contact probe pads and schematic illustration of fabricated device structure are shown in Figure 3.45. The record-high true avalanche gain of > 10^4 was achieved from a relatively large 50 μm mesa diameter device. Reverse-bias *I-V* characteristics are shown in Fiure 4.46. The yield of working devices out of a processed wafer turned out to be over 90% and devices demonstrated the repeatable stable operation.

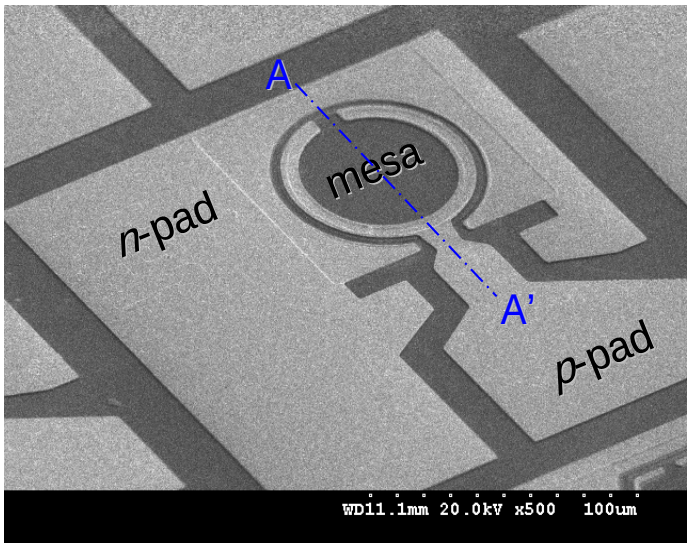

(a)

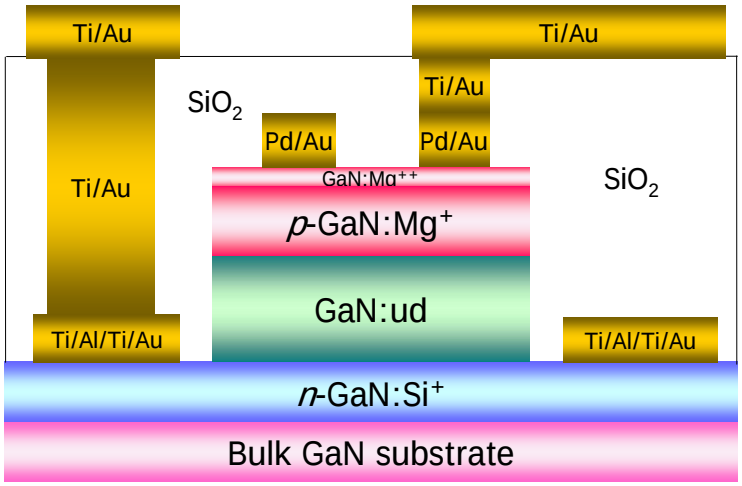

(b)

Figure 3.45: (a) SEM image of a fabricated GaN *p-i-n* APD device with contact probe pad (b) Schematic drawing of a fabricated device structure via section A-A'.

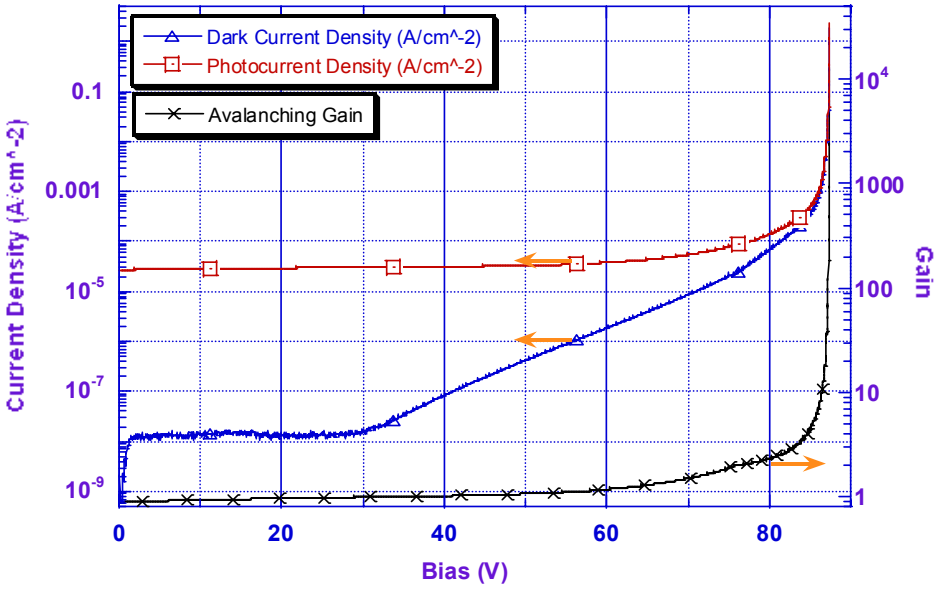

(a)

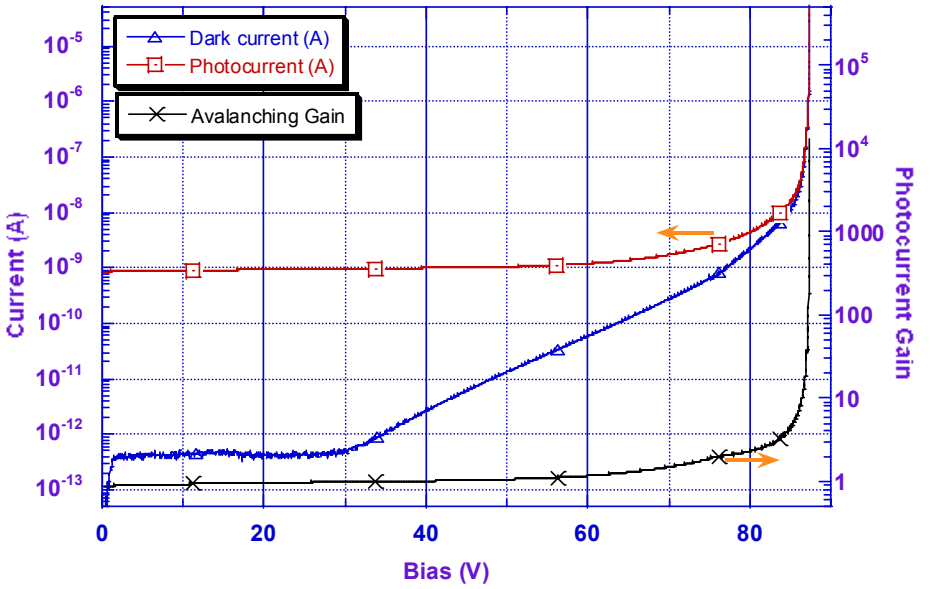

(b)

Figure 3.46: Reverse-bias *I-V* characteristics of a 50 µm mesa diameter GaN *p-i-n* APD with contact probe pad. The dark current, photocurrent, and avalanche gain (*M*) are plotted versus reverse bias voltage: (a) current density (A/cm^2) (b) current (A).

3.5 AlGaN *p-i-n* APD on bulk GaN substrates

In order to achieve intrinsically solar-blind APDs, the use of wider-bandgap material than GaN is required; but the growth of AlGaN APD structures on bulk GaN substrates introduces additional technological challenges such as imperfects materials quality accompanied by more stringent growth conditions of Al-containing epitaxial materials. The $Al_xGa_{1-x}N$ growth may introduce dislocations and strain and even strain-induced cracking. Also, $Al_xGa_{1-x}N$ has limited doping efficiency for *p*-type doping. Using the epitaxial material development and *p*-doping study, the first $Al_xGa_{1-x}N$ ($x \sim 0.05$) *p-i-n* APDs were grown and fabricated based on the standard processing techniques.

As mentioned before, the development of a low-resistivity AlGaN:Si layer is important for UV APDs because the high *n*-layer resistivity can lead to current crowding towards the edge of the mesa, causing the potential premature breakdown of devices. In order to serve this purpose, the Si-doping study for $Al_xGa_{1-x}N$ ($x \sim 0.05$) was carried out. The composition of an AlGaN layer was determined by triple axis X-ray rocking curve, as shown in Figure 3.47. A 300K Hall-effect measurement on $Al_{0.05}Ga_{0.95}N:Si^+$ on thick GaN layer shows a mobility of ~ 96 $cm^2/V{\cdot}s$ and $[n] \sim 1.8\times10^{19}\ cm^{-3}$. Figure 3.48 shows the average resistivity of 109.2 Ω/□ and a standard deviation of 2.0. This low and uniform resistivity may be interpreted as uniformity of carrier concentration, mobility and material quality. Hall-effect measurement data are summarized in Table 3.12

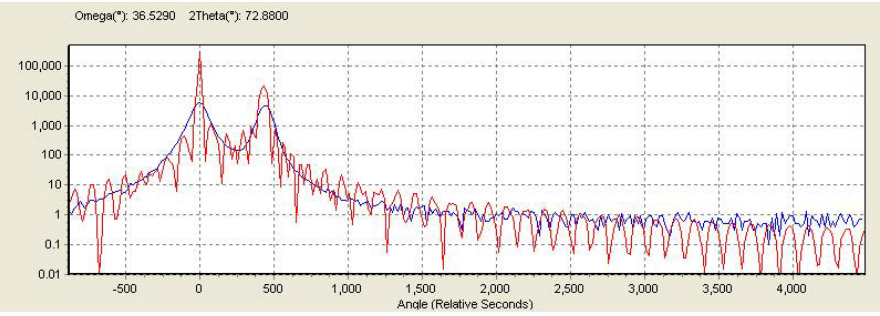

Figure 3.47: Triple axis rocking curve (blue) and dynamic XRD simulation fitting (red) of 360 μm $Al_{0.055}Ga_{0.945}N$ on GaN/sapphire template.

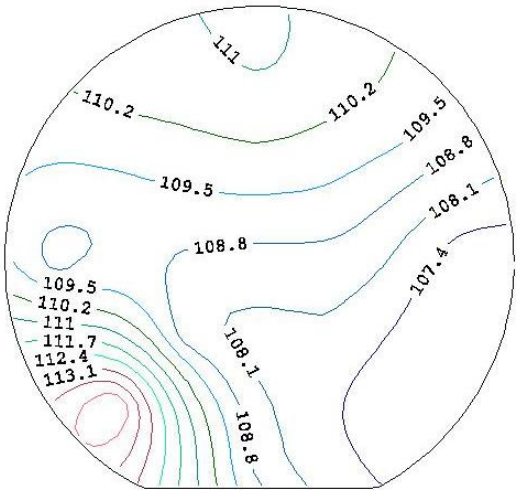

Figure 3.48: Resistivity map of $Al_{0.5}Ga_{0.95}N:Si^{+}$ layer on thick undoped GaN layer.

Table 3.12: Summary of room temperature Hall-effect data of $AlGaN:Si^{+}$ layer on thick GaN/sapphire template.

Description	$AlGaN:Si^{+}$
Temperature	AMB
Thickness	0.40 μm
Symmetry	1.60
Sheet R	9.15×10^{1} Ω /square
Bulk R	3.66×10^{-3} Ω-cm
Sheet Hall Coefficient	-8.78×10^{-1} m^2/C
Bulk Hall Coefficient	-3.51×10^{-7} m^3/C
Sheet N	$-7.11e\times10^{14}$ cm^{-2}
Bulk N	-1.78×10^{19} cm^{-3}
Mobility	9.60×10^{1} $cm^2/V\cdot s$

The epitaxial structure for AlGaN APD on bulk GaN substrates consists of an *n*-type $Al_{0.05}Ga_{0.95}N:Si$ layer, followed by an unintentionally doped $Al_{0.05}Ga_{0.95}N$ drift region (0.25 μm, $n < 5\times10^{16}$ cm^{-3}), a *p*-type $Al_{0.05}Ga_{0.95}N:Mg$ layer, and topped with *p*-type $GaN:Mg^{++}$ (heavily Mg-doped) contact layer. The free carrier concentrations and mobilities in the *p*-type and *n*-type $Al_xGa_{1-x}N$ ($x = \sim 0.05$) layers were calibrated to be $p =$

~ 5×10^{17} cm^{-3} and n = ~3×10^{18} cm^{-3} with μ_e = ~ 200 $cm^2/V\cdot s$, respectively. Improved crystalline and structural quality for $Al_xGa_{1-x}N$ (x~0.05) epitaxial layers were achieved by employing optimum growth parameters on low-dislocation-density (< 1×10^6 cm^{-2}) bulk GaN substrates in order to minimize the defect density in epitaxially grown materials. A graded layer from unintentionally doped GaN to $Al_xGa_{1-x}N$ (x = 0.05) was inserted as a strain management layer for the crack-free growth of AlGaN *p-i-n* structures on GaN substrates. Figure 3.49 shows the AFM images of the surface of an $Al_{0.05}Ga_{0.95}N$ UV APD wafer revealing atomic steps on the surface with no visible nano-pits. Root-mean square (RMS) surface roughness values are approximately 0.17 nm and 0.19 nm for 1×1 μm^2 scans and 5×5 μm^2 scans, respectively.

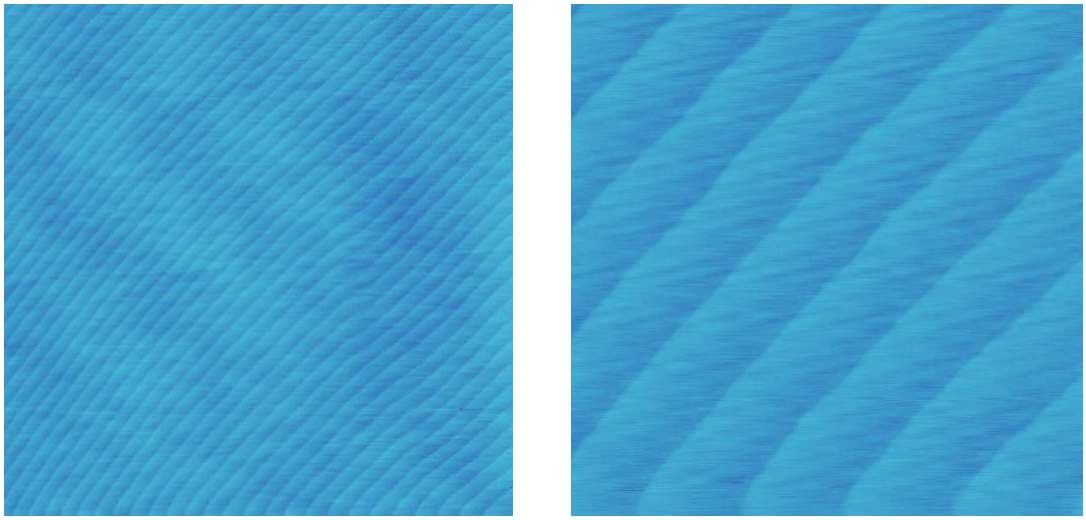

(a) (b)

Figure 3.49: AFM microscopic surface morphology of an $Al_{0.05}Ga_{0.95}N$ ultraviolet APD wafer grown on a bulk GaN substrate: (a) 5×5 μm^2 scan (b) 1×1 μm^2 scan with z-height scale of 10 nm.

The devices were fabricated into 30 μm- and 50 μm-diameter circular mesas by low-damage inductively coupled plasma (ICP) etching using a Cl_2/He carrier gas mixture.

After mesa definition, a SiO_2 passivation layer was applied to the devices using plasma-enhanced chemical vapor deposition (PECVD). The width of the dot-shaped p-contact metal is 12 μm. The complete device structure is schematically shown in Figure 3.50. The forward *I-V* characteristics and low reverse bias voltage (up to -100 V) *I-V* characteristics were measured using an Agilent HP4156C precision semiconductor parameter analyzer.

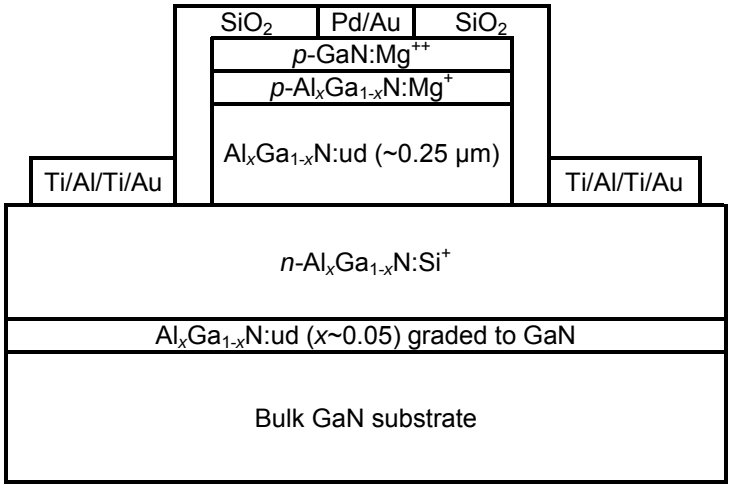

Figure 3.50: Schematic diagram of the $Al_{0.05}Ga_{0.95}N$ APD mesa-geometry device structure grown on a bulk GaN substrate.

Figure 3.51 shows a comparison of the photocurrent and dark-current characteristics at 300 K for a 30 μm-diameter mesa AlGaN UVAPD as well as the reverse-bias *I-V* characteristics near avalanche breakdown above 80 V. No microplasmas or side-wall breakdown luminescence was visually observed. The photocurrent was obtained using a UV lamp emitting at an average intensity of 4,500 $\mu W/cm^2$ with a peak emission wavelength of ~254 nm. The avalanche gain (*M*) is taken as the difference between the reverse-biased photocurrent and dark current, divided by the difference

between the low-bias photocurrent and low-bias dark current. The photocurrent increases with bias. The reference unity gain photocurrent was set at a reverse voltage of 70 V, which is a "conservative" approach in estimating avalanche gain. The avalanche gain reaches a maximum value of ~50 at a voltage of 86.75 V.

Bias-dependent spectral response of a photocurrent was also measured and is shown in Figure 3.52. For the spectral response measurement, a Keithley 4200 semiconductor characterization system, an Oriel xenon lamp, a Cornerstone 260 monochromator/chopper system, a Perkin Elmer 7265 DSP lock-in amplifier were used for optical wavelength selection and modulation, and photocurrent measurement. The photocurrent at zero-bias exhibits a peak absorption at 350 nm (~3.5 eV) equivalent to the bandgap of $Al_{0.05}Ga_{0.95}N$. This peak absorption wavelength is shorter than that of comparable GaN *p-i-n* APDs on free-standing GaN substrate by ~15 nm. The spectral response of GaN APDs on a free-standing substrate can be found in the following literature.[84] The absorption cut-off is found at 370 nm, which is ~10 nm shorter than those of comparable GaN *p-i-n* APDs. Therefore, by employing AlGaN structures, the long peak wavelength and cut-off were shifted toward the deeper UV spectral region. This also suggests that $Al_xGa_{1-x}N$ with $x > 0.4$ is required to achieve intrinsic (filter-free) solar-blind UV APDs. The peak absorption wavelength is slightly shifted to ~ 360 nm possibly due to the Franz-Keldysh effect [85 , 86] as the reverse bias increases. Photocurrent decreases as wavelength becomes shorter, indicating reduced carrier collection efficiency. The photocurrent, however, is still substantial near ~280nm. Red-shift behavior of voltage dependent spectral response of the AlGaN APDs is similar to that of the GaN APDs. [84]

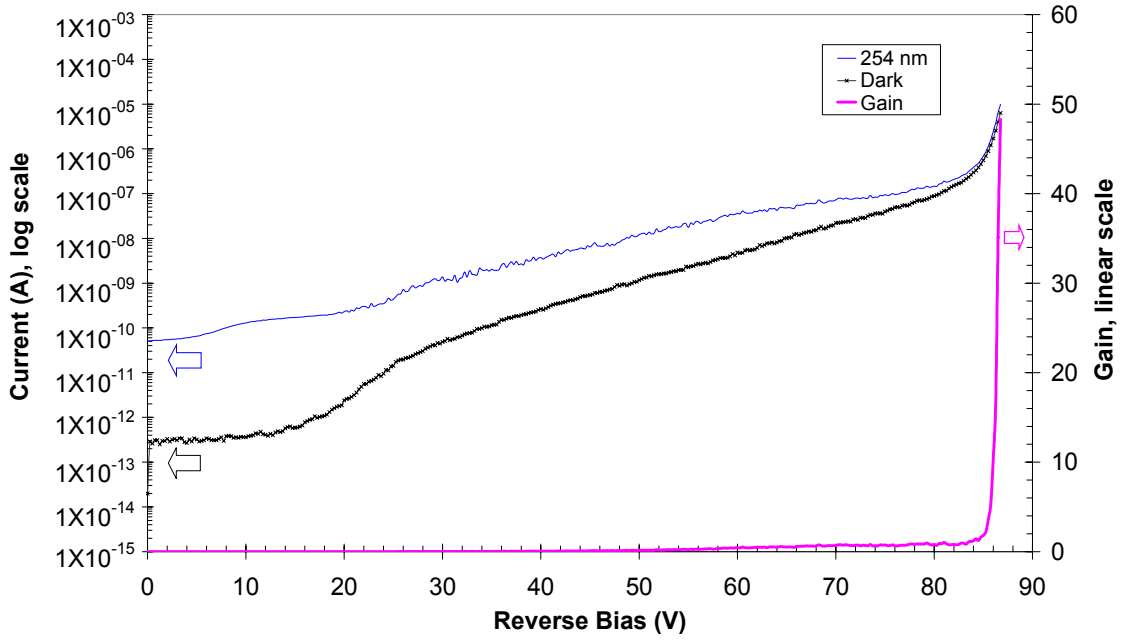

(a)

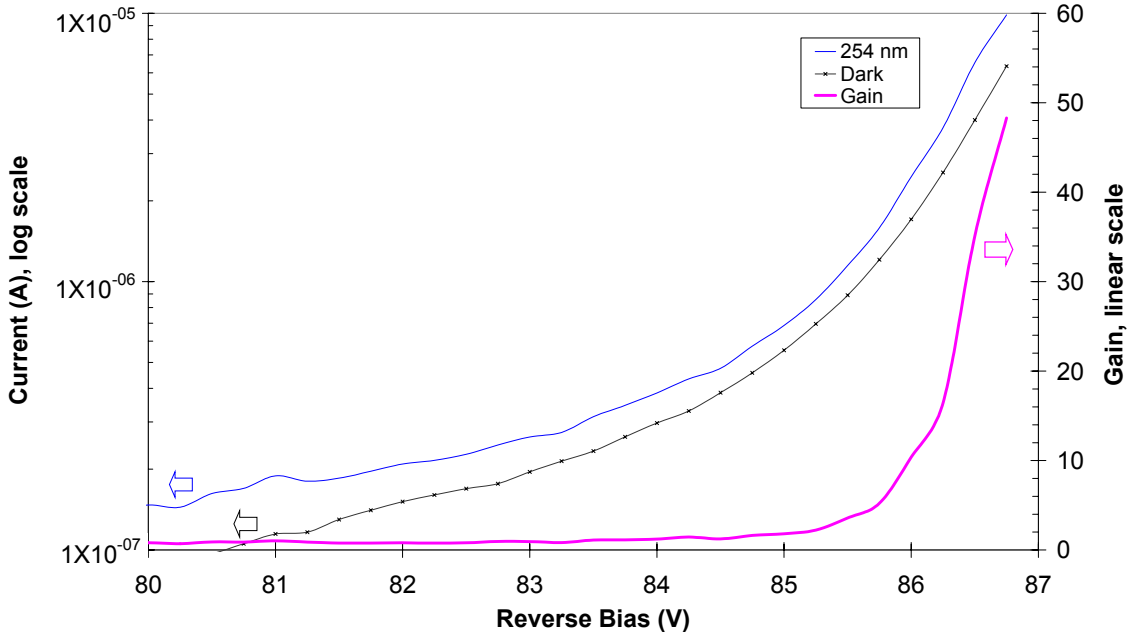

(b)

Figure 3.51: (a) Reverse-bias *I-V* characteristics of an $Al_{0.05}Ga_{0.95}N$ UV APD having a mesa diameter of 30 μm (b) Reverse-bias *I-V* characteristics near avalanche breakdown above 80 V.

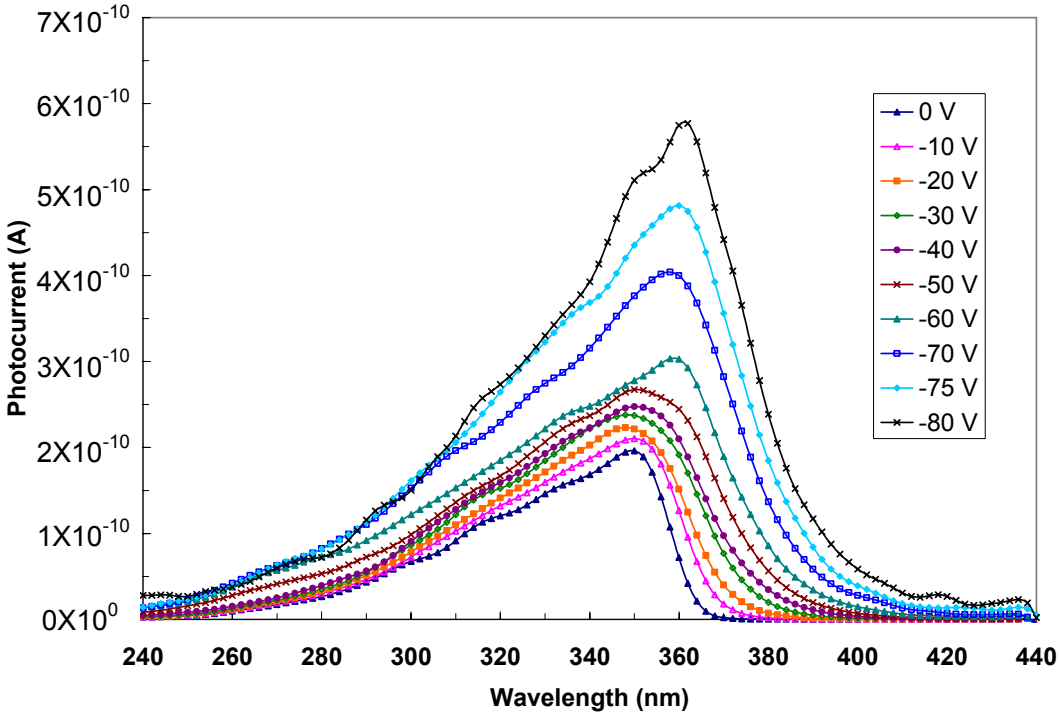

(a)

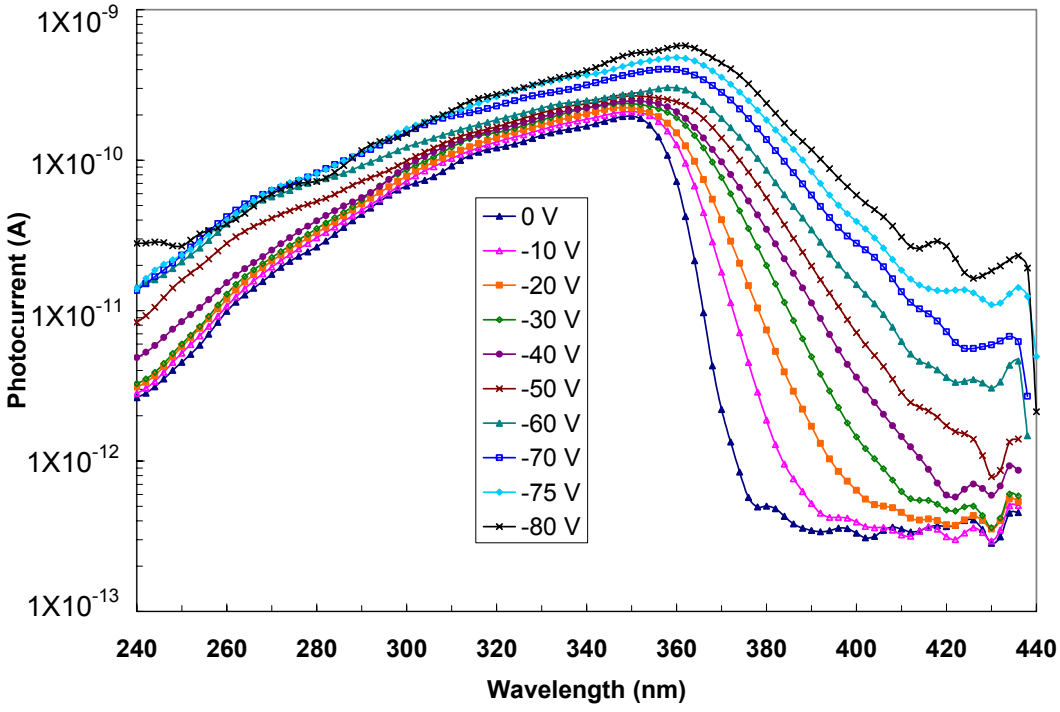

(b)

Figure 3.52: Voltage-dependent spectral response of photocurrent for an $Al_{0.05}Ga_{0.95}N$ UV APD measured at room-temperature; (a) linear scale (b) log scale.

CHAPTER 4

DEVELOPMENT OF NITRIDE POWER RECTIFIERS

4.1 Introduction

There has been increasing research interest in the use of wide-bandgap semiconductors such as GaN or SiC, for applications in high-power and high-temperature electronic devices, e.g., *p-i-n* rectifiers, heterojunction bipolar transistors (HBTs), and heterojunction field-effect transistors (HFETs) [87,88] for the past years due to their superior physical and electronic properties such as high thermal stability, large chemical bond strength, large direct energy bandgap, and high electric field strength. [88] Wide-bandgap semiconductors have great potential to replace silicon, which is currently the dominant semiconductor material for high-power switching applications and also InGaP/GaAs materials for high-performance HBTs. SiC high-power switching device performance has drastically improved recently due to the intense research on SiC growth and processing technologies.[89,90] GaN devices are predicted to out-perform Si and SiC devices for power applications [88]. Consequently, group III-nitride materials are receiving more and more attention for high-power electronic applications owing to their unique and promising material properties. Recently, various groups have demonstrated III-V nitride-based power devices.[91,92,93,94] III-N *p-i-n* rectifiers are expected to offer high-power operation for many applications, including power switching. Nitride-based *p-i-n* devices are of interest as well for the basic element in the development of nitride DC-to-DC power converters. In addition to the improved performance at high-power, these devices should also be capable of operation at high temperatures and in a high-radiation environment such as space.

4.2 Advantages of Nitride *p-i-n* Rectifiers

The primary advantage of employing *p-i-n* rectifiers as power devices is the benefit from the low resistance during the "On-state" operation and high breakdown voltage. Thus, the device can sustain a high current density under forward bias with low power losses [95,96] - one of the main critical aspects for many high-power device applications. To realize the high-performance and reliable nitride power rectifiers, the nitride material quality plays an indispensable role. Currently, the lack of a convenient large-area lattice-matched substrate creates many problems in the epitaxial growth of high-quality III-Nitrides. Most of the epitaxial growth of III-Nitrides have been performed on basal plane (*c*-plane) sapphire substrates (α-Al_2O_3) because it has a hexagonal wurtzite crystal structure that is the same as the thermodynamically stable structure of GaN, is inexpensive, and has a high thermal stability. However, there is about 10% lattice mismatch between the III-Nitrides epitaxial layers and the sapphire substrates. In this study, the development of a GaN *p-i-n* rectifier structure grown on lattice-less-mismatched (SiC) or lattice-matched (GaN) and thermally compatible substrate materials was performed to greatly improve the device performance characteristics. The research activities include new device structure designs, the epitaxial growth by metalorganic chemical vapor deposition, device fabrication, and characterization of the devices.

4.3 Development of Full-Vertical *p-i-n* Rectifiers

4.3.1 Motivation

GaN-based materials can be grown on either sapphire substrates or SiC substrates. The growth of GaN-based materials on SiC substrates offers several advantages over the growth on sapphire substrates. GaN on SiC has a reduced degree of lattice mismatch;

thereby, resulting in a lower defect density in the epitaxial GaN-based layers. Also, SiC substrates have higher thermal conductivity than sapphire substrates (3.7~4.9 $Wcm^{-1}K^{-1}$. for 4H- and 6H-SiC, respectively vs. 0.27 $Wcm^{-1}K^{-1}$ for sapphire); hence, SiC provides better thermal management for device operation. The advances in SiC substrate manufacturing technologies over past decades allow them to be used in a variety of high-power electronic devices.[23] For the growth of GaN on a SiC substrate, AlN grown at high temperature has been shown to be a suitable buffer layer. This is because SiC-AlN has a relatively small *a*-axis lattice mismatch of approximately 1% [24]; however, one of the problems of using AlN as a buffer layer is that it is an insulator having a large ionization activation energy of ~320 meV for Si donors [97] as well as a large energy bandgap of 6.2 eV.

In a conventional III-N rectifier design that utilizes sapphire substrates or an insulating AlN buffer layer on SiC substrates, mesa-defined top *p*- and *n*-contact structures are the inevitable choice, accompanying a deep etch step for device fabrication and resulting in a non-uniform electric-field distribution in the device. As a result, when a GaN-based device is grown on a SiC substrate with a conventional AlN buffer layer, a full-vertical device configuration [98], which has the back-side *n*-ohmic contact to the bottom of the SiC substrate and front-side *p*-ohmic contact on top of the epitaxial structures, cannot be realized; therefore, with an AlN buffer and a device mesa structure, the excess leakage current through sidewall damage by deep dry etching and a certain degree of current crowding are unavoidable.

As one of the alternative approaches, a low Al-composition AlGaN (up to an Al-mole fraction ~0.15), which can be directly grown on SiC substrates with reasonably conductive characteristics has been studied; however, the phase separation with the fluctuation of Al content and three-dimensional GaN island morphology have been observed.[99,100,101,102,103] The difference in the surface mobility between Al and

Ga atoms on the growing surface, which is one of the crucial parameters in AlGaN growth, has also been published.[104]

4.3.2 Development of AlGaN:Si Conducting Buffer Layer

The conventional growth technique used for growing GaN on SiC substrates requires a 100 ~ 200 nm-thick high-temperature grown AlN buffer layer.[24] An AlN layer of this thickness introduces significant resistance to a vertical-geometry device. As a result, mesa definition for a thick *p*-*i*-*n* GaN epitaxial rectifier structure requires deep dry etching for device fabrication; thereby, current crowding at the bottom of the *i*-region, as well as the increase of the current leakage due to damaged sidewalls, are inevitable. The growth of GaN *p*-*i*-*n* rectifiers on a *n*-type SiC conducting substrate enables the structural design of full-vertical rectifiers without using a deep mesa etch, having the *n*-contact on the bottom of substrate in contrast to the case of insulating substrates; however, the direct growth of GaN on SiC substrates gives poor GaN material quality. In this case, GaN three-dimensional islands develop and the surface morphology becomes rough.[100] The best results for GaN/SiC epitaxial structures are usually obtained using AlN, acting as a wetting agent, as a buffer layer.[24,105]

To overcome this technological barrier, high-temperature grown AlGaN:Si buffer layers were investigated to realize a full-vertical GaN *p*-*i*-*n* structure for rectifier applications. The layer is required to satisfy two conditions to serve as a conducting buffer layer. First, the buffer layer needs to be conducting and also must be vertically conducting through the buffer-substrate interface and second, it should be effective as a buffer layer in terms of improving the crystalline and structural quality for the subsequent growth of epitaxial layers. The AlGaN:Si buffer layer was calibrated to achieve the improved crystalline and structural quality by altering growth conditions and epitaxial designs. The NH_3 molar flow rate was lowered during the initial stage of AlGaN:Si growth to promote the lateral movement of Al ad-atoms. TMAl and TMGa molar flows

were targeted to obtain the slow growth rate for an AlGaN:Si layer. Also, the total thickness of the AlGaN:Si layer as well as a strain accommodation layer was varied to obtain an atomically smooth and nano-pit free surface on subsequently grown GaN layers. AlGaN buffer layers were grown on (0001) 6H-SiC *n*-type substrates at a low pressure of 50 Torr to minimize the homogeneous gas-phase reactions between TMAl and NH_3 [80,81] while all of the subsequent GaN layers were grown at 200 Torr. The growth temperature was set at 1050˚C to minimize the thermal transient between growth of the AlGaN:Si layer and GaN layers. TMAl, TMGa, and NH_3 molar flows were optimized to promote the lateral movement of Al ad-atoms during the growth of AlGaN:Si buffer layers. The Al mole fraction of the AlGaN layer was measured to be approximately 0.1, determined from photoluminescence and XRD. The carrier concentration in the $Al_xGa_{1-x}N$:Si (x= ~ 0.1) layer was estimated to be 3×10^{18} cm^{-3}, as determined from the layer grown on an undoped GaN layer on a sapphire substrate with similar growth conditions.

The vertical transport characteristics of *n*-type $Al_xGa_{1-x}N$:Si (x= ~ 0.1) on a *n*-type SiC substrate were studied to determine the electrical properties. For this purpose, a metallization scheme using Ti/Al/Ti/Au on top of the *n*-AlGaN:Si and Ni/Au on the backside of the *n*-type SiC substrate was deposited by an electron-beam evaporator system. As shown in Figure 4.1, the structure demonstrated excellent Ohmic characteristics between the *n*-*n* heterojunction with a 180 μm diameter circular mesas.

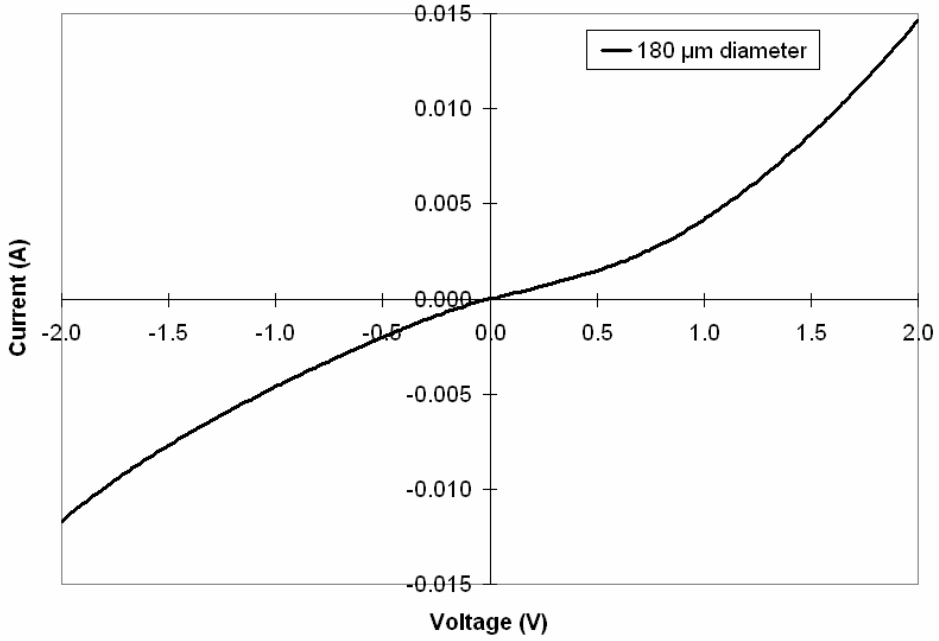

Figure 4.1: Vertical transport characteristics of $Al_{0.1}Ga_{0.9}N$:Si conducting buffer layer grown on an *n*-type 6H-SiC substrate.

A small kink in the *I-V* characteristic was observed for forward bias conditions and it is believed to have originated from the heterostructure barrier at the *N*-AlGaN -- *n*-SiC junction due to the band-offset combined with the Fermi level pinning effect due to interface defects.[106] Another possible origin of the kink could be a non-ideal Ohmic contact behavior; however, the Ohmic behavior of the contact, especially for *n*-AlGaN, was verified by a TLM (transmission line measurement) study. The surface morphology of an $Al_xGa_{1-x}N$:Si (x= ~ 0.1) conducting buffer layer was also characterized by AFM and it resulted in a smooth surface with RMS roughness values of 0.44 nm and 0.63 nm for a 1×1 μm^2 scan and 5×5 μm^2 scan, respectively.

4.3.3 Characterization of Full-Vertical *p-i-n* Rectifiers

The examination with a Nomarski optical microscope revealed a smooth surface for a full-vertical GaN *p-i-n* rectifier structure with $Al_xGa_{1-x}N$:Si (x = ~ 0.1) as a

conducting buffer layer. An $Al_xGa_{1-x}N$:Si (x = ~ 0.1) layer graded to GaN:Si layer was inserted as a strain relaxation layer underneath the *n*-type GaN. The microscopic surface morphology was characterized by AFM. Figure 4.2 shows AFM images (under the *z*-height of 10 nm) revealing an atomically smooth surface with no visible nano-pits. The AFM images show an atomically smooth surface with no visible nano-pits, demonstrating the superior material quality of GaN epitaxial layers grown on AlGaN conducting buffer layers on n-SiC substrates. RMS roughness values are approximately 0.22 nm and 0.26 nm for 1×1 μm^2 scan and 5×5 μm^2 scan, respectively.

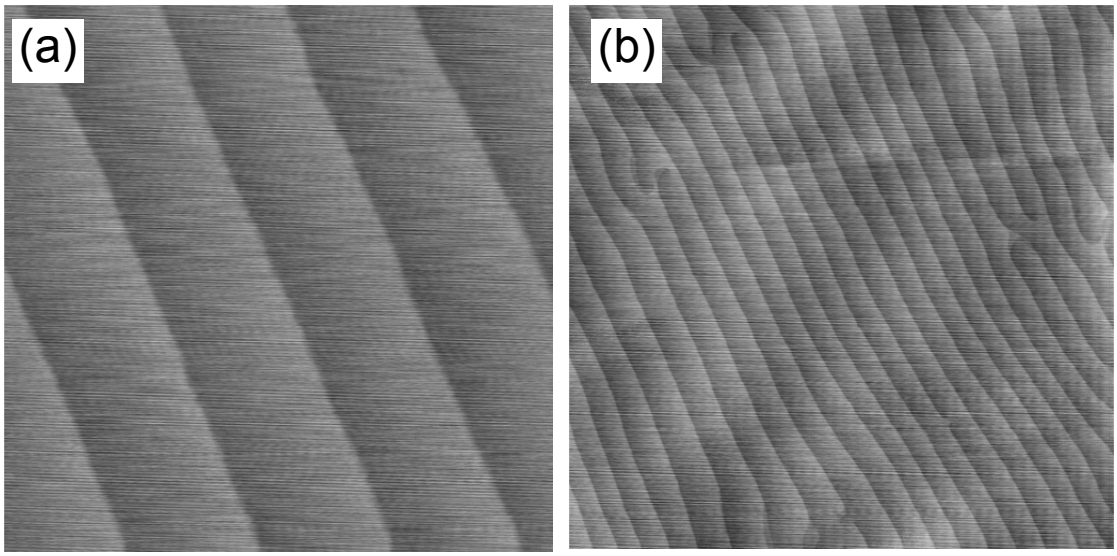

Figure 4.2: AFM microscopic surface morphology of a full-vertical rectifier structure on an *n*-AlGaN:Si conducting buffer layer grown on an *n*-type (0001) 6H-SiC substrate: (a) 1×1μm^2 scan (b) 5×5μm^2 scan with the *z*-height scale of 10 nm.

The crystalline quality of GaN epitaxial layers on a conducting buffer layer/SiC substrate for full-vertical structures was analyzed using a high-resolution X-ray diffractometer. The full-width-at-half-maximum (FWHM) line-widths of the GaN-related peaks show in Figure 4.3 are ~181 arc-sec. and ~320 arc-sec. for (002) and (102) scans respectively, which are comparable to those of GaN *p-i-n* rectifier structures employing a conventional AlN buffer layer on SiC substrates.

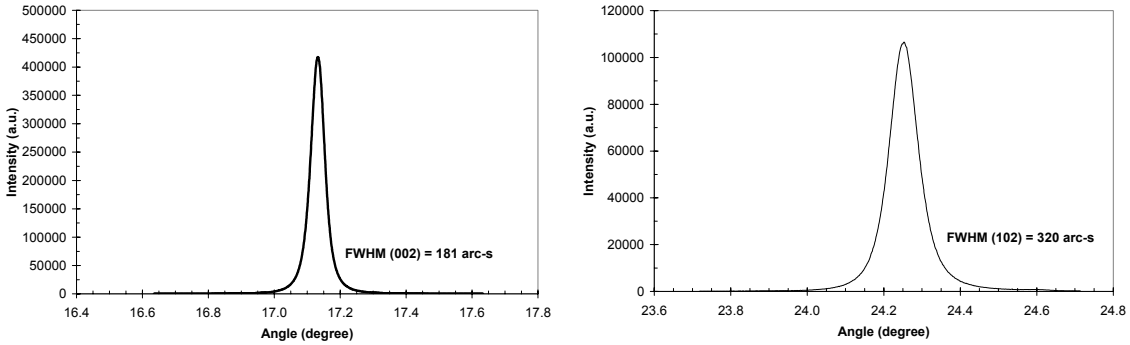

(a) (b)

Figure 4.3: X-ray rocking curves of a full vertical *p-i-n* rectifier: (a) (002) symmetric scan (b) (102) asymmetric scan.

The optimization of *p*-GaN:Mg, *p*-GaN:Mg^{++}, and *n*-GaN:Si layers for the diode were carried out. With the optimization of TMGa and NH_3 molar flows as well as SiH_4 and Cp_2Mg molar flows, the free carrier concentrations and mobilities in the *p*-type and *n*-type GaN for the rectifier structure are measured to be $p = 1\times10^{18}$ cm^{-3} with $\mu_h = \sim12$ $cm^2/V\cdot s$ and $n=5\times10^{18}$ cm^{-3} with $\mu_e = \sim210$ $cm^2/V\cdot s$, respectively, as determined by 300K Hall-effect measurements. Figure 4.4 shows the secondary ion mass spectroscopy (SIMS) depth profiling data for a GaN:Mg sample exhibiting $p = 1\times10^{18}$ cm^{-3}. Unintentional carbon and oxygen impurity levels are well controlled (very low or near the detection limit) and Mg concentration in the GaN:Mg layer is [Mg] = 4×10^{19} cm^{-3}, indicating that ~2.5% of Mg incorporated into GaN is activated as a *p*-type dopant.

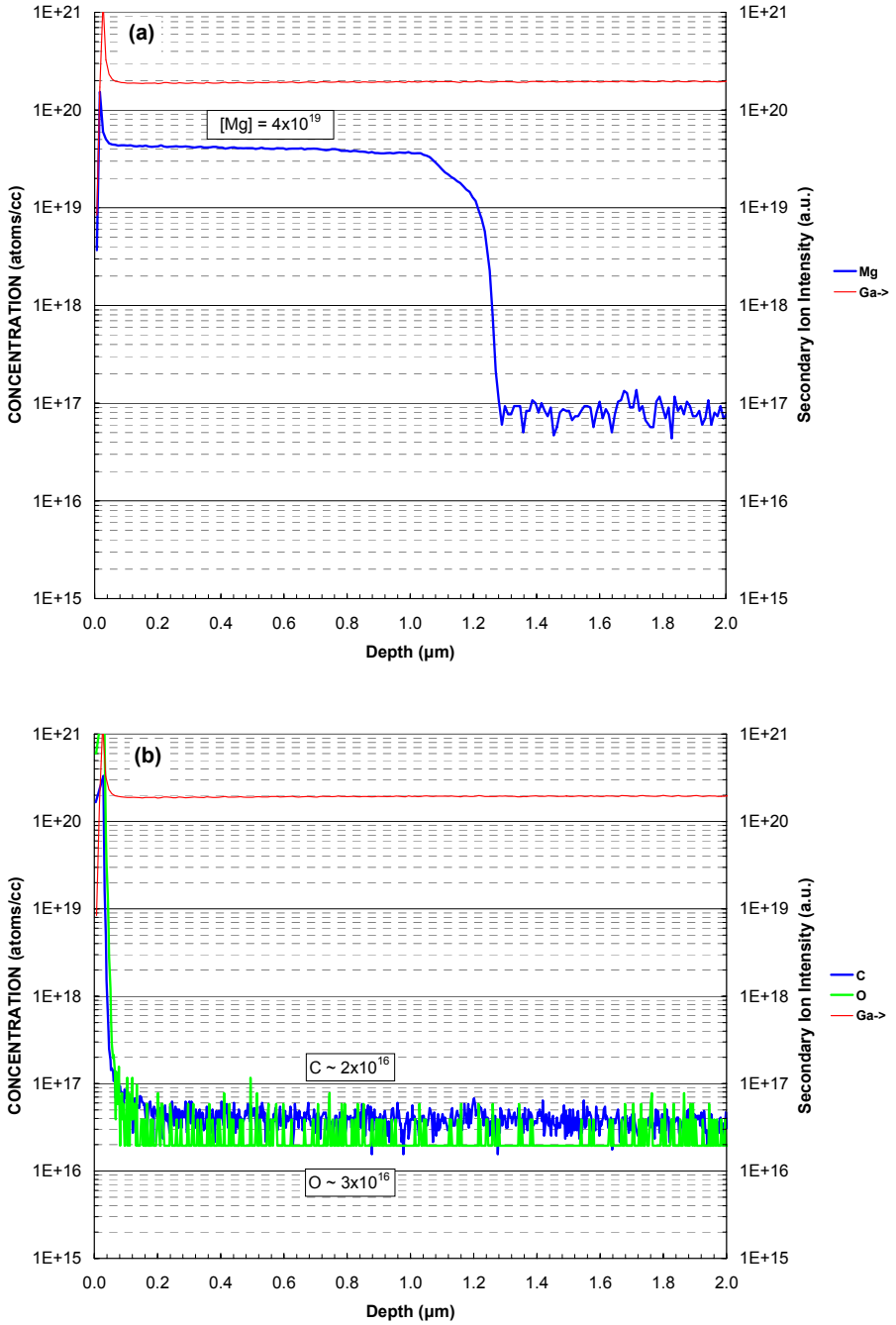

Figure 4.4: (a) SIMS profile of GaN:Mg layer having free hole concentration, $p = 1\times10^{18}$ cm^3 with 12 $cm^2/V{\cdot}s$ (b) SIMS profile of carbon and oxygen impurities for GaN:Mg layer.

The investigation of the *I-V* characteristics of the *p*-GaN:Mg^{++} cap layer was also performed. The Mg concentration as well as the thickness was optimized to optimize the Ohmic behavior. The Cp_2Mg flow rate and growth time for GaN:Mg^{++} cap layer were varied to obtain an improved Ohmic behavior, reducing the specific contact resistance from TLM measurements. The optimized contact layer is estimated to contain [Mg] ~ 1.2×10^{20} cm^{-3} with a thickness of 20 nm.

The epitaxial structure for the rectifier consists of, in order from top to bottom, the GaN:Mg^{++} contact layer, *p*-GaN:Mg^{+}, 2.5 μm-thick unintentionally doped GaN, *n*-GaN:Si^{+}, and an AlGaN:Si^{+} conducting buffer layer. The energy-band diagram of the epitaxial structure for the device is also shown in Figure 4.5. For the construction of the energy-band diagram, a one-dimensional simulation [107] was applied to the GaN *p-i-n* structure. The intrinsic doping level of unintentionally doped *i*-GaN was assumed to be $n\sim1\times10^{15}$ cm^{-3} and the spontaneous and piezoelectric polarization effects were not considered in the simulation. The band structure for a portion of the grading layer, the $Al_xGa_{1-x}N$:Si (x= ~ 0.1) conducting buffer layer, and the *n*-type 6H-SiC substrate is schematically illustrated based on a similar structure from a previous report.[106]

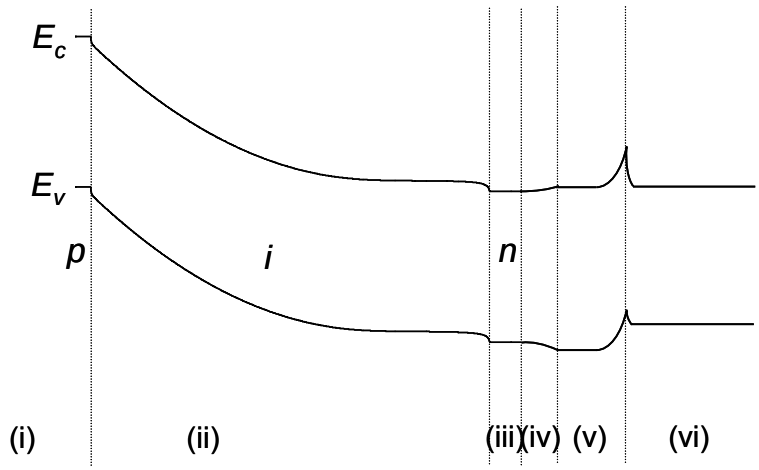

Figure 4.5: Energy-band diagram of the epitaxial structure on the substrate in thermal equilibrium: (i) *p*-GaN:Mg, (ii) unintentionally doped *i*-GaN, (iii) *n*-GaN:Si, (iv) AlGaN-GaN grading, (v) AlGaN conducting buffer layer , and (vi) *n*-SiC substrate.

The planar devices in this study did not use a current guiding structure. The Ni/Au and Pd/Au metallization schemes were applied for the Ohmic contacts on *n*-SiC and *p*-GaN, respectively. The analysis of *I-V* characteristics in the reverse high-voltage regime was carried out using a high-voltage power supply system. Forward *I-V* characteristics and reverse *I-V* characteristics were measured using an Agilent HP4156C precision semiconductor parameter analyzer, HP4142B *I-V* analyzer and Stanford Research Systems PS350 high-voltage power supply. The reverse breakdown of a full-vertical GaN *p-i-n* rectifier with a relatively thin 2.5 μm-thick *i*-region was V_{BR} > -330 V with on-resistance of R_{ON} = 7.5 $\times 10^{-3}$ Ω·cm^2. The forward turn-on voltage (V_f) of the devices in this study is approximately 7.5V, which is related to the thick *i*-layer of wide-bandgap materials. The *I-V* characteristics in the low forward bias regime and the reverse *I-V* characteristics are shown in Figure 4.6.

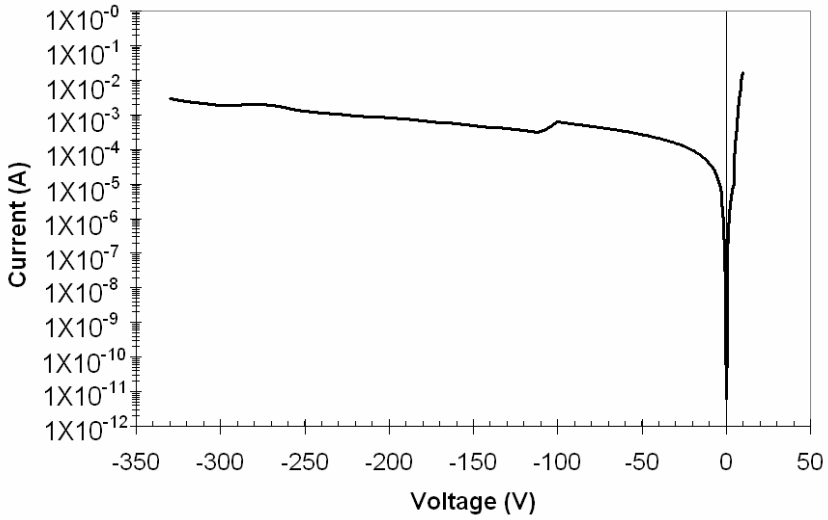

Figure 4.6: Current-voltage characteristics of a full-vertical GaN *p-i-n* rectifier.

4.3.4 Device Design Optimization

Two-dimensional simulations were performed using the DESSIS module bundled in the ISE TCAD software [108], which calculates the currents and electric fields in the devices. Based on the simulation results and consideration of the heteroepitaxy of GaN devices on AlGaN:Si buffer layers, the unintentionally doped *i*-region was set at ~ 2.5 μm to achieve the increase in the blocking voltage with reasonably low series resistance. The full-vertical GaN *p-i-n* rectifier structures employed in this study consist of a 20 nm-thick p^{++}-GaN:Mg cap layer, 100 nm-thick p^{+}-GaN:Mg (p = 1×10^{18} cm^{-3}), 2.5 μm unintentionally-doped GaN *i*-layer, 100 nm-thick *n*-GaN:Si (n = 5×10^{18} cm^{-3}), and 250 nm-thick $Al_{0.1}Ga_{0.9}N$:Si as a conducting buffer layer in the order from the top to the bottom of the epitaxial structure. For fabricated devices, Ni/Au and Pd/Au ohmic contacts were deposited on the backside of the *n*-SiC substrate and on top of *p*-GaN epitaxial layer, respectively. The *n*-type metal contact covered most of the backside of the wafer (a piece approximately 1×1 cm^2), while *p*-type metal contact was defined in circular shape with a diameter from 30 to 100 μm by lithography.

Two configurations of devices schematically shown in Figure 4.7 were fabricated

and compared: one does not have any current guiding scheme and the other has current guiding only in the relatively thin *p*-layer. To provide the current guiding in the *p*-layer, the layer was shallow-etched by ICP (inductively coupled plasma) dry etching and passivated by PECVD (plasma-enhanced chemical vapor deposition)-deposited SiO_2. Using the GaN *p-i-n* structure on the AlGaN:Si conducting buffer layer, two configurations of current-guiding schemes were studied to optimize the device design: one did not employ any current guiding and the other had the current guiding only in the relatively thin *p*-layer. *n*-type GaN:Si layer and *p*-type GaN:Mg^+ layer were kept at a relatively thin 100 nm to lower the series resistance. The diameter of Pd/Au *p*-contact was 60 μm for both configurations while the diameter for *p*-current guiding in full-vertical *p-i-n* rectifiers is 80 μm. The lateral dimensions of the active region for a full-vertical device in this work is determined by the field distribution and the current spreading between *p*-contact and large area backside *n*-contact.

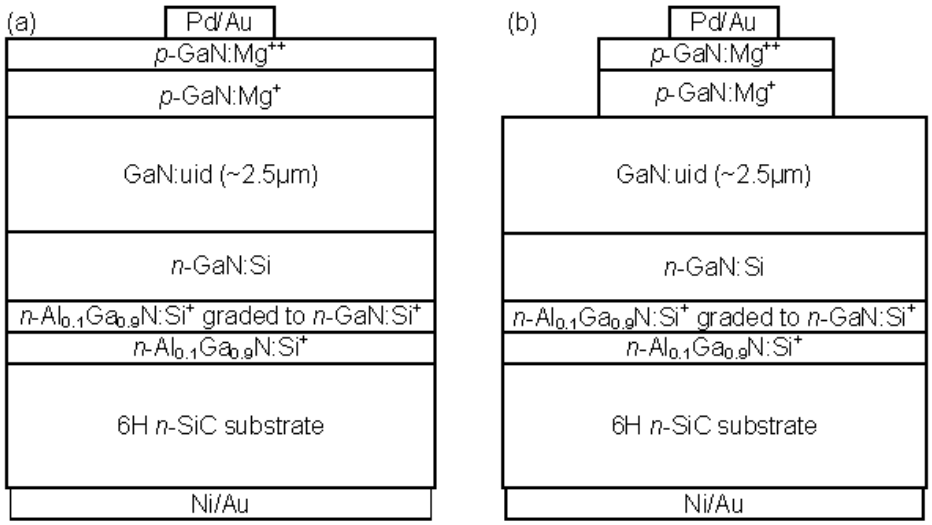

Figure 4.7: Schematic diagrams of full-vertical GaN *p-i-n* rectifier device structures: (a) devices without any current guiding scheme (b) devices with a current guiding scheme only in *p*-layer.

Figure 4.8 shows an *I-V* characteristic comparison between the rectifiers with and without the *p*-current guiding structure. The devices compared have a *p*-type metal contact diameter of 60 μm. Both configurations of devices result in a low on-resistance (R_{ON}) of 7.5 $\times 10^{-3}$ $\Omega \cdot cm^2$ and the forward turn-on voltage (V_f) of the devices is approximately 7.5V, which is related to the relatively thick *i*-layer of wide-bandgap materials. The reverse-breakdown voltage for rectifiers with a relatively thin 2.5 μm-thick *i*-region without the *p*-current guiding was found to be over -330V, while devices with the *p*-current guiding structure were measured to be over -400V. The full-vertical rectifier devices with the *p*-current guiding structures exhibit a much lower reverse-bias leakage current (by 4 orders of magnitude at -100V), indicating that the current guiding even in the relatively thin *p*-layer facilitates the reduction of the reverse-bias leakage current and improves the device performance characteristics.

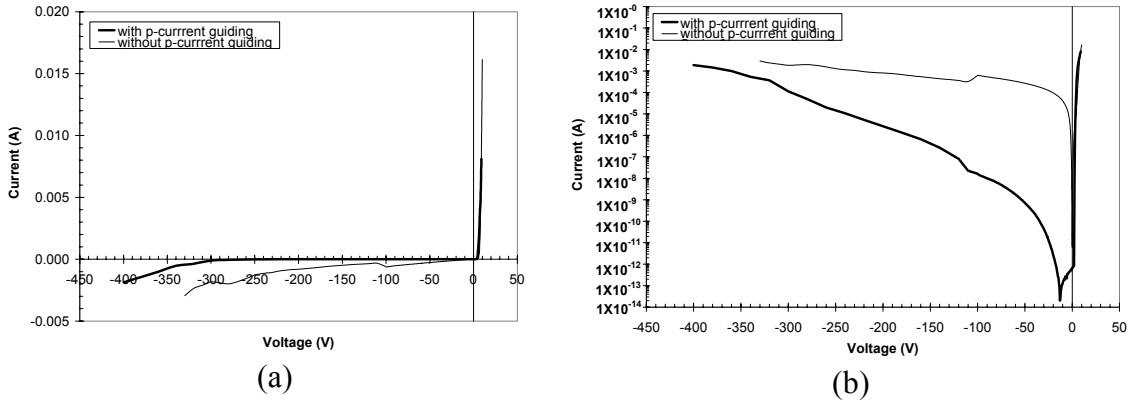

Figure 4.8: *I-V* characteristic comparison between the rectifier structures with and without a *p*-current guiding scheme: (a) linear plot (b) logarithmic plot.

The relatively high reverse leakage current in the device without current guiding can be attributed to current spreading in the *p*-layer and the *i*-region as well as the very thick *n*-layer (including *n*-GaN, AlGaN conducting buffer layer, and *n*-SiC substrate) with the backside contact covering most of the SiC substrate; hence, alternative methods

for current guiding in our rectifiers are proposed: One possibility is proton implantation and the other is *n*-contact area definition using a small-area backside metal contact. To obtain the detailed aspects of the desired ion-implantation profile, a simulation for the proton implantation was carried out using SRIM (Stopping and Range of Ions in Matter) software.[109] Further studies of device design optimization for full-vertical rectifiers will be performed.

4.4 Low On-resistance GaN *p-i-n* rectifiers on SiC substrates

Considering better thermal conductivity and relatively small *a*-axis lattice mismatch of SiC over sapphire substrates as well as availability at relatively low cost of SiC substrartes over bulk GaN substrates, the growth of GaN on an *n*-type 6H-SiC is one of the ways to reduce the dislocation density; thereby, improving device performance. GaN *p-i-n* rectifiers grown on *n*-type 6H-SiC substrates with optimized growth conditions were fabricated using the standard processing techniques. These devices result in the reverse breakdown voltage (V_r) of > -500 V at a current density (I_r) ~1 A/cm^2. The specific On-resistance (R_{ON}) is approximately 2.3 mΩ·cm^2. These values yield a figure-of-merit value of $(V_{RB})^2/R_{ON}$ = 108.69 MW/cm^2.

4.5 High-Performance GaN *p-i-n* rectifiers on Bulk GaN substrates

A wide variety of GaN-based electronic devices have attracted great commercial interest in the past decade due to their superior physical and electrical properties.[88] These devices exhibit lower on-resistance and lower switching loss with high breakdown voltages [95,96] when compared to that of similar Si-based devices. The heteroepitaxial growth of III-N layers on relatively large-area sapphire and SiC substrates have been studied for these devices; however, the high density of defects due to misfit dislocations

created during the heteroepitaxy of group III-Nitride materials can cause a device failure. Hence, it is becoming increasingly clear that growth on low-dislocation-density "bulk" III-N substrates has several intrinsic advantages for high-performance devices. It is considered that the homoepitaxy for power devices enable us to exploit the theoretical performance limit for GaN.

GaN *p-i-n* rectifier structure on bulk GaN substrates having a mesa diameter of 80 μm with a metal contact diameter of 60 μm were fabricated. As shown in Figure 4.9, the reverse breakdown voltage of $V_r \sim$ -540 V and the current density of $I_r \sim 0.1$ A/cm^2 at V_r ~-500 V were obtained.

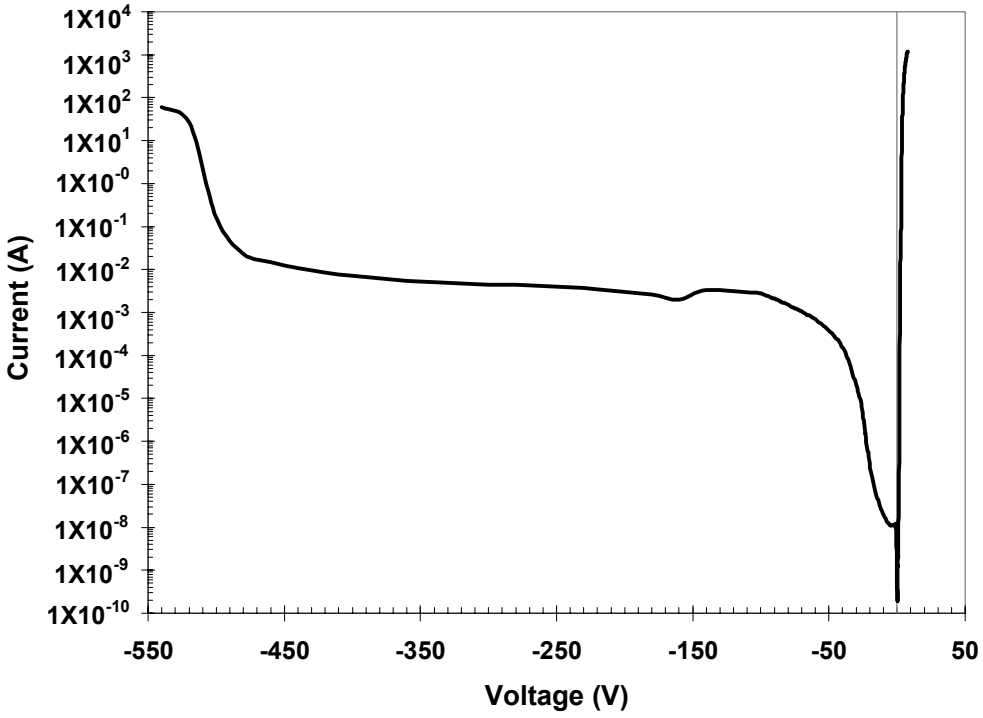

Figure 4.9: Current versus voltage measured for a GaN p-i-n rectifier on a bulk GaN substrate.

The specific On-resistance is R_{ON} ~3 mΩ·cm^2. A figure-of-merit value was calculated to be $(V_{RB})^2/R_{ON}$ = 97.2 MW/cm^2. These values are close to the simulation

results for this device structure using a commercial device simulator, which predict a breakdown voltage V_r ~-700 V and a forward voltage drop of 3.3V at a forward current density of 100A/cm^2 [110]. A high forward voltage drop is expected for wide-bandgap materials, especially for direct-bandgap semiconductors like GaN that have extremely short carrier lifetimes relative to indirect-bandgap semiconductors like SiC [88,111].

CHAPTER 5

SUMMARY AND FUTURE WORK

A wide variety of group III-Nitrides materials system has opened a new era in the field of semiconductor research for the past decade. They have become of great commercial importance fueled by their potentials that extend beyond the capability of Si technology. The direct and large bandgap nature, intrinsic high carrier mobility, and the capability of forming heterostructures allow them to dominate the photonic and electronic device markets such as light emitters, photodiodes, or high-speed/high-power electronic devices. MOCVD has become the dominant technology for epitaxial growth of epitaxial III-nitrides due to its versatility.

Avalanche photodiodes (APDs) based on group III-Nitrides materials are of interest due to their potential capabilities for low dark current densities, high sensitivities and high optical gains in the ultraviolet (UV) spectral region. Wide-bandgap GaN-based APDs, such as AlGaN and GaN-based *p-i-n* diodes, are excellent candidates for short-wavelength photodetectors because they have the capability for cut-off wavelengths in the ultraviolet (UV) spectral region less than $\lambda = 290$ nm. These intrinsically solar-blind UV APDs will not require filters to operate in the solar-blind spectral regime of $\lambda < 290$ nm. For the growth of GaN-based heteroepitaxial layers on lattice-mismatched substrates, a high density of defects is usually introduced during the growth; thereby, causing a device failure by premature microplasma breakdown before the electric field reaches the level of the bulk avalanche breakdown field, which has been a major issue for GaN-based APDs. In contrast, photomultiplier tubes (PMTs) offer high-sensitivity in UV detection; however, PMTs require a high-voltage power supply and are relatively fragile and expensive. Due to their compact footprint and material characteristics, APDs are small, stable, and less expensive in comparison to PMTs.

To bring UV APDs based on group III-Nitrides materials system into realization, the following issues need to be properly addressed. First, AlGaN layers are less prone to formation of cracks which inherite from in-plane compressive strain with respect to bulk AlN substrates. The band edge of a substrate is transparent to deep UV spectral regime. In addition, having a UV transparent substrate enables both front and back illuminating device geometry; however, the quality and size of bulk AlN substrates have limitations to date. On the other hand, AlGaN layers grown on bulk GaN substrates experience in-plane tensile strain with respect to the substrate, which can lead to crack formation; therefore, the development of strain management engineered epitaxial structures is inevitable. There is inevitable light absorption in the *p*-layer for top illuminating device geometry in the case of not UV transparent substrates. The growth of AlGaN APD structures on GaN substrates introduces additional technological challenges such as imperfect materials quality accompanied by more stringent growth conditions of Al-containing epitaxial materials. However, the growth of relatively low Al-content $Al_xGa_{1-x}N$ ($x < 0.2$) on bulk GaN substrates can utilize the matured substrate technology with low defect density of less than 10^6 cm^{-2}.

The development of high-performance GaN and AlGaN APDs has been described in this work. High-quality $Al_xGa_{1-x}N$ ($0 \le x \le 1$) epitaxial layers grown on low dislocation density native bulk III-N substrates have brought never-before-possible high-performance UV APDs into realization. GaN *p-i-n* APDs grown on bulk GaN substrates demonstrated the true stable avalanche gain of > 10,000 out of devices with 50 μm mesa diameter. These are the largest APDs with highest avalanche gain ever reported using GaN. These GaN APDs exhibit the testing-system-limited low-reverse-voltage ($|V_R| < 60$ V) dark current and current density of $I_R = 5\times10^{-14}$ A and $J_R = 7.0\times10^{-9}$ A/cm^2, respectively. It can be attributed partly to high-quality epitaxial layers and partly to the incorporation of low dislocation density bulk GaN substrates. In order to achieve intrinsically solar-blind APDs, the use of wider-bandgap material than GaN is required;

thus, the research was focused on the deeper UV spectral regime. With the aid of a strain management engineered structure, the first demonstration of true avalanche breakdown for $Al_{0.05}Ga_{0.95}N$ APDs on bulk GaN substrates was realized based on the extensive work on the $Al_xGa_{1-x}N$ ($0 \leq x \leq 1$) materials system. The true avalanche gain of ~ 50 was achieved.

The research on high Al-content $Al_xGa_{1-x}N$ ($x > 0.3$) APDs are intensively carried out on bulk AlN substrates. The development of next-generation growth technique such as modulated precursor epitaxial growth (MPEG) to overcome the current growth issues associated with conventional growth technologies for high-quality AlGaN is one of the keys to the realization of true solar-blind APDs operating at $\lambda < 290$ nm. The more effort will be given in this area of the research. However, the material may not be the only issue in development of solar-blind AlGaN APDs. Further optimization of device processing technology such as low-damage sidewall etching or sidewall passivation for AlGaN materials is required.

The growth of $Al_{1-x}In_xN$ ($x = 0.16$) alloys which are lattice-matched to GaN, having a direct bandgap energy of $E_g = 4.61$ eV equivalent to ~ 270 nm at room-temperature will be carried out. This lattice-matched AlInN approach will permit the direct growth of high-quality intrinsic deep UV APDs on bulk GaN substrates.

The superior physical and electronic properties such as high thermal stability, large chemical bond strength, large direct energy bandgap, and high electric field strength of group III-Nirides have brought much research interest to high speed/high power devices such as GaN *p-i-n* rectifiers. The study was focused on the two sections; development of (1) full-vertical GaN rectifiers (2) GaN rectifiers on low-dislocation density bulk GaN subtrates.

The development of a AlN-free full-vertical GaN *p-i-n* rectifier on 6H *n*-type SiC substrates by employing a conducting $Al_xGa_{1-x}N$:Si ($x = \sim 0.1$) buffer layer scheme was discussed. This full vertical configuration provides the advantage of the reduction of

sidewall damage from plasma etching and lower forward resistance due to the reduction of current crowding in the bottom *n*-type layer. In this vertical configuration, the *n*-contact was made on the back-side of the SiC substrate using a Ni/Au metallization scheme. The $Al_xGa_{1-x}N$:Si nucleation layer was proven to provide excellent electrical properties while also acting as a good buffer layer for subsequent GaN growth. The reverse breakdown voltage for a relatively thin 2.5 μm-thick *i*-region was found to be over -400V. For GaN *p*-*i*-*n* rectifiers grown on bulk GaN substrates, the reverse blocking voltage of $V_r \sim$ -540V was demonstrated.

Further development on the proton implantation or Fe-doping study may be required to reduce sidewall leakage current more effectively. In addition, the backside *n*-contact optimization is essential to improve the performances of full-vertical *p*-*i*-*n* rectifiers.

REFERENCES

[1] H. M. Manasevit, Appl. Phys. Lett. 11, 156 (1968).

[2] H. M. Manasevit, F. Erdmann, and W. Simpson, J. Electrochem. Soc. 118, 1864 (1971)

[3] R. D. Dupuis, P. D. Dapkus, R. D. Yingling, and L. A. Moudy, Appl. Phys. Lett. 31, 203 (1977)

[4] S. Yoshida, S. Misawa, and S. Gonda, Appl. Phys. Lett. 42, 427 (1983)

[5] H. Amano, N. Sawaki, I. Akasaki, and Y. Toyoda, Appl. Phys. Lett. 48, 353 (1986).

[6] S. Nakamura, Jpn. J. Appl. Phys. 30, L1705 (1991).

[7] S. Nakamura, M. Senoh, S. Nagahoma, N. Iwasa, T. Yamada, T. Matsushita, H. Kiyoku, and S. Sugimoto, Appl. Phys. Lett. 68, 2105 (1996)

[8] M. Tanaka, S. Nakahata, K. Sogabe, H. Nakata, and M. Tabioka, Jpn. J. Appl. Phys. 36, L1062 (1997).

[9] S. Nakamura and S.F. Chichibu, *Introduction to Nitride Semiconductor Blue Laser and Light Emitting Diodes*, pp. 105-150, Taylor & Francis, New York (2000).

[10] V. Yu. Davydov, A. A. Klockikhin, R. P. Siesyan, V. V. Emtsev, S. V. Ivanov, F. Bechstedt, J. Furthmuller, H. Harima, A. V. Mudryi, J. Aderhold, O. Semchinova, and J. Graul, Phys. Stat. Sol. (b) 229, R1 (2002)

[11] V. Yu. Davydov, A. A. Klockikhin, V. V. Emtsev, S. V. Ivanov, V. V. Vekshin, F. Bechstedt, J. Furthmuller, H. Harima, A. V. Mudryi, A. Hashimoto, A. Yamamoto, J. Aderhold, J. Graul, and E. E. Haller, Phys. Stat. Sol. (b) 230, R4 (2002).

[12] M. Hori, K. Kano, T. Yamaguchi, Y Saito, T. Araki, Y. Nanishi, N. Teraguchi, and A. Suzuki, Phys. Stat. Sol. (B) 234, 750 (2002).

[13] J. Wu, W. Walukiewicz, K. M. Yu, J. W. Ager III, E. E. Haller, H. Lu, W. Schaff, Y. Saito, and Y. Nanishi, Appl. Phys. Lett. 80, 3967 (2002).

[14] J. Wu, W. Walukiewicz, W. Shan, K. M. Yu, J. W. Ager III, E. E. Haller, H. Lu, and W. Schaff, Phys. Rev. B 66, 201403 (2002).

[15] J. Wu, W. Walukiewicz, K. M. Yu, J. W. Ager III, E. E. Haller, Hai Lu, and William J. Schaff, Phys. Stat. Sol. (B) 240, 412 (2003).

[16] J. Wu, W. Walukiewicz, K. M. Yu, J. W. Ager III, S.X. Li, E. E. Haller, Hai Lu, and William J. Schaff, Solid State Comm. 127, 411 (2003).

[17] Y. Ishitani, H. Masuyama, W. Terashima, M. Yoshitani, N. Hashimoto, S. B. Che, A. Yoshikawa, Phys. Stat. Sol. (C) 2, 2276 (2005).

[18] K. M. Yu, Z. Liliental-Weber, W. Walukiewicz, W. Shan, and J.W. Ager III, S.X. Li, R. E. Jones, and E.E. Haller, Hai Lu, and William J. Schaff, Appl. Phys. Lett. 86, 071910 (2005).

[19] S. N. Mohammad and H. Morkoç, Prog. Quant. Electron. 20, 361 (1996).

[20] A.F. Wright, J.S. Nelson, Appl. Phys. Lett. 66,3465 (1995).

[21] I. Vurgaftman, J.R. Meyer, L.R. Ram-Mohan, J. Appl. Phys. 89, 5815 (2001).

[22] H. Morkoç, S. Strite, G. B. Gao, M. E. Lin, B. Sverdlov, and M. Burns, J. Appl. Phys. 76, 1363 (1994).

[23] J. Zolper, M.Skowronski et. al., MRS Bulletin 30, 273 (2005).

[24] T. Weeks Jr., M. Bremser, K. Ailey, E. Carlson, W. Perry, and R. Davis, Appl. Phys. Lett. 67, 401 (1995).

[25] Hadis Morkoc, *Nitride Semiconductors and Devices*, Springer, 1998.

[26] Available: http://www.phys.ksu.edu/area/GaNgroup (04/2007).

[27] E. S. Yang, *Microelectronic Devices*, McGraw-Hill, New York, 1988.

[28] J. H. Edgar, *Properties of Group III Nitrides*, EMIS Datareviews Series 11, 1994.

[29] P. G. Neudeck, D. J. Larkin, J. E. Starr, J. A. Powell, C. S. Salupo, and L. G. Matus, IEEE Trans. Elec. Dev. 41, 826 (1994).

[30] Y. Takeda, Amer. Ceram. Soc. Bull. 67, 1961 (1988).

[31] S. M. Sze, *Physics of Semiconductor Devices*, Wiley, New York, 1981.

[32] B. Gil, Group III Nitride Semiconductor Compound Physics and Applications, pp. 72-74, Oxford Science Publications (1998).

[33] V. Ban, J. Electrochem. Soc. 119, 761 (1972).

[34] C. R. Biber, C.A. Wang, and S. Motakef, J. Crystal. Growth. 123, 545 (1992).

[35] Available via technical presentations from Thomas Swan Scientific Equipments.

[36] Available: http://www.laytec.de (04/2007).

[37] A. Krost, G. Bauer, and J. Woitok, *Optical Characterization of Epitaxia Semiconductor Layers*, G. Bauer and W. Richter (Eds.), pp.287-421, Srpinger, Berlin, Germany (1995).

[38] C. R. Wie, Materials Science and Engineering R13, 1 (1994).

[39] W. J. Bartels, J. Vac. Sci. Technol. B1, 338 (1983).

[40] B. E. Warren, *X-Ray Diffraction* pp. 18, 21, Dover, New York, U.S.A. (1990).

[41] *Digital Instrument TR Mode-Torsional Resonance Mode Imaging Bulletin*, Veeco Instruments Inc., Santa Babara, California (2003).

[42] R. E.Lee, "Scanning Electron Microscopy and X-ray Microanalysis," Prentice Hall, Englewood Cliffs, New Jersey (1993).

[43] M.R.H. Khan, Y. Koide, Itoh, N. Sawaki, and I. Akasaki, Solid State Commun. 60, 509 (1986).

[44] Available: http://mse.iastate.edu/microscopy (04/2007).

[45] Y. Koide, H. Itoh, M.R.H. Khan, K. Hiramatu, N. Sawaki, and I. Akasaki, J. Appl. Phys. 61, 4540 (1987).

[46] A. F. Wright and J. S. Nelson, Appl. Phys. Lett. 66, 3051 (1995).

[47] H. Angerer, D. Brunner, F. Freudenberg, O. Ambacher, M. Stutzmann, R. Höpler, T. Metzger, E. Born, G. Dollinger, A. Bergmaier, S. Karsch, and H.-J. Körner, Appl. Phys. Lett. 71, 1504 (1997).

[48] D. Brunner, H. Angerer, E. Bustarret, F. Freudenberg, R. Höpler, R. Dimitrov, O. Ambacher, and M. Stutzmann, J. Appl. Phys. 82, 5090 (1997).

[49] Yen-Kuang Kuo and Wen-Wei Lin, Jpn. J. Appl. Phys. 41, 73 (2002).

[50] L. van der Pauw, Philips Research Reports, 13, 1 (1958).

[51] K. A. McIntosh, R. J. Molnar, L. Mahoney, A. Lightfoot, M. W. Geis, K. Molvar, I. Melngailis, R. L. Aggarwal, W. D. Goodhue, S. S. Choi, D. L. Spears, and S. Verghese, Appl. Phys. Lett. 75, 3485 (1999).

[52] J. C. Carrano, D. J. H. Lambert, C. J. Eiting, C. J. Collins, T. Li, S. Wang, A. L. Beck, R. D. Dupuis, and J. C. Campbell, Appl. Phys. Lett. 76, 924 (2000).

[53] K. A. McIntosh, R. J. Molnar, L. J. Mahoney, K. M. Molvar, N. Efremow, Jr., and S. Verghese, Appl. Phys. Lett. 76, 3928 (2000).

[54] B. Yang, T. Li, K. Heng, C. Collins, S. Wang, J. Carrano, R. D. Dupuis, J. C. Campbell, M. J. Schurman, and I. Ferguson, IEEE Journal of Quantum Electronics. 36, 1389 (2000).

[55] X. Xin, F. Yan, X. Sun, P. Alexandrove, C. Stahle, J. Hu, M. Matsumura, X. Li, M. Weiner, and H. Zhao, Elec. Lett. 41, 212 (2005).

[56] M. Rahman, A. Al-Ajili, R. Bates, A. Blue, W. Cunningham, F. Doherty, M. Glaser, L. Haddad, M. Horn, J. Melone, M. Mikuz, T. Quinn, P. Roy, V. O'Shea, K.M. Smith, J. Vaitkus, and V. Wright, IEEE Trans. on Nuclear Science 51, 2256 (2004)

[57] S. Verghese, K. A. McIntosh, R. J. Molnar, L. Mahoney, R. Aggarwal, M. Geis, K. Molvar, E. Duerr, I. Melngailis, IEEE Trans. on Elect. Dev. 48, 592 (2001).

[58] A. Beck, G. Karve, S. Wang, J. Ming, X. Guo, and J. C. Campbell, IEEE Photonics Technology Lett. 17, 1507 (2005).

[59] UV-enhanced PMTs are typically based upon Cs-Te photocathodes such as that used in the Hamamatsu R1080 PMT; Hamamatsu Photonics. Available: http://usa.hamamatsu.com (04/2007).

[60] T. Isoshima, Y. Isojima, K. Hakomori, K. Kikuchi, K. Nagai, and H. Nakagawa, Rev. Sci. Instrum. 66, 2922 (1995)

[61] A. Osinsky, M. S. Shur, R. Gaska, and, Q. Chen, Electron. Lett.34, 691 (1998)

[62] K. J. Schoen, J. M. Woodall, J. A. Cooper, and M. R Melloch, IEEE Trans. Electron. Dev. 45, 1595 (1998).

[63] F. Yan, C. Qin, J. H. Zhao, M. Bush, G. Olsen, B. K. Ng, J. P. R. David, R. C. Tozer, and M. Weiner, Solid-State Electronics 47, 241 (2003)

[64] B. K. Ng, F. Yan, J. P. R. David, R. C. Tozer, G. J. Rees, C. Qin, and J. H. Zhao, IEEE Photonics Technology Letters 14, 1342 (2002).

[65] G. Xiangyi, A. Beck, Y. Bo, and J. C. Campbell, Electronics Letters 39, 1673 (2003).

[66] G. Xiangyi, A. L. Beck, L. Xiaowei, J. C. Campbell, D. Emerson, and J. Sumakeris, IEEE Journal of Quantum Electronics 41, 562 (2005).

[67] V. Bougrov, M. E. Levinshtein, S. L. Rumyantsev, and A. Zubrilov, *Properties of Advanced SemiconductorMaterials GaN, AlN, InN, BN, SiC, SiGe*, M. E. Levinshtein, M. Levinshtein, and S. L. Rumyantsev (Eds.), pp.1-30, John Wiley & Sons, Inc. New York (2001).

[68] I. Akasaki, H. Amano, M. Kito, and Hramatsu, J. Lumin. 48, 666 (1991).

[69] Obtained from Epichem Inc., Haverhill, MA.

[70] S. Yoshida, S. Misawa, and S. Gonda, J. Vac. Sci. Technol. B, 1, 250 (1983).

[71] Y. Koide, N. Itoh, X. Itoh, N. Sawaki, and I. Akasaki, Jpn. J. Appl. Phys. 27, 1156 (1988).

[72] S. Nakamura, Jpn. J. Appl. Phys. 30, L1705 (1991).

[73] T. Ito, K. Ohtsuka, K. Kuwahara, M. Sumiya, Y. Takano, and S. Fuke, J. Crystal Growth 205, 20 (1999).

[74] M. S. Yi, H. H. Lee, D. J. Kim, S. J. Park, D. Y. Noh, C. C. Kim, and J. H. Je, Appl. Phys Lett. 75, 2187 (1999).

[75] J. N. Kuznia, M. Asif Khan. D. T. Olson, R. Kaplan, and J. Freitas, J. Appl. Phys. 73, 4700 (1993).

[76] T. Yang, K. Uchida, T. Mishima, J. Kasai, and J. Gotoh, Phys. Stat. Sol. (A), 180, 45 (2000).

[77] K. S. Kim, C. S. Oh, K. J. Lee, G. M. Yang, C. H. Hong, K. Y. Lim, H. J. Lee, and A. Yoshikawa, J. Appl. Phys. 85, 8441 (1999).

[78] T. Ito, M. Sumiya, Y. Takano, K. Ohtsuka, and S. Fuke, Jap. J. Appl. Phys. Part 1 38, 649 (1999).

[79] M. Leszczynski, T. Suski, H. Teisseyre, P. Perlin, I. Grzegory, J. Jun, S. Porowski, and T.D. Moustakas, , J. Appl. Phys. 76, 4909 (1994).

[80] C. Chen, H. Liu, D. Steigerwald, W. Imler, C. Kuo, and M. Craford, J. Electron. Mater. 25, 1004 (1996).

[81] J. Han, J. Figiel, M. Crawford, M. Banas, M. Bartram, R. Biefeld, Y. K. Song, and A. Nurmikko, J. Crystal Growth 195, 291 (1998).

[82] I. D. Goepfert, E. F. Schubert, A. Osinsky, and P. E. Norris, Mat. Res. Soc. Symp. Proc. 595, W3.85.1 (2000)

[83] W. Lee, J. Limb, J. -H. Ryou, D. Yoo, T. Chung, and R. D. Dupuis, J. Crystal Growth 287, 577 (2006).

[84] S.-C. Shen, Y. Zhang, D.-W. Yoo, J.-B. Limb, J.-H. Ryou, and R. D. Dupuis, IEEE Photon. Tech. Lett., submitted (2007)

[85] W. Franz, Einfluß eines elektrischen Feldes auf eine optische Absorptionskante, Z. Naturforschung 13a, 489 (1958)

[86] L. V. Keldysh, Behaviour of Non-Metallic Crystals in Strong Electric Fields, J. Exptl. Theoret. Phys. (USSR) 33, 994 (1957)

[87] K. J. Schoen, J. M. Woodall, J. A. Cooper, and M. R Melloch, IEEE Trans. Electron. Dev. 45, 1595 (1998).

[88] M. Trivedi and K. Shenai, J. Appl. Phys. 85, 6889 (1999).

[89] Q. Wahab, T. Kimoto, A. Ellison, C. Hallin, M. Tuominen, R. Yakimova, A. Henry, J. P. Bergman, and E. Janzen, Appl. Phys. Lett. 72, 445 (1998).

[90] K. G. Irvire, R. Singh, M. J. Paisley, J. W. Palmour, O. Kordina, and C. H. Carter, Jr., Mat. Res. Soc. Symp. Proc. 512, 119 (1998).

[91] Z. Z. Bandic, P. M. Bridger, E. C. Piqutte, T. C. McGill, R. P. Vaudo, V. M. Phanse, and J. M. Redwing, Appl. Phys. Lett. 74, 1266 (1999).

[92] G. T. Dang, A. P. Zhang, F. Ren, X. A. Cao, S. J. Pearton, H. Cho, J. Han, J. I. Chyi, C. M. Lee C. C. Chuo, S. N. G. Chu, R. G. Wilson, IEEE Trans. Electron Dev. 47, 692 (2000).

[93] F. Ren, A. P. Zhang, G. T. Dang, X. A. Cao, H. Cho, S. J. Pearton, J. I. Chyi, C. M. Lee, and C. C. Chuo, Sol. State Electron. 44, 619 (2000).

[94] T. G. Zhu, D. J. H. Lambert, B.S. Shelton, M. M. Wong, U. Chowdhury and R. D. Dupuis, "High-Voltage GaN Vertical p-i-n Rectifier with a 2μm-Thick i-Layer," Electron. Lett., Vol. 36, No. 23, pp. 1971-1972 (2000).

[95] Y. Irokawa, B. Luo, B.S. Kang, J. Kim, J.R. Laroche, F. Ren, K.H. Baik, S.J. Pearton, C.-C. Pan, G.-T. Chen, J.-I. Chyi, S.S. Park, Y.J. Park, Sol.-Stat. Elec. 48, 359 (2004)

[96] Y. Irokawa, J. Kim, F. Ren, K.H. Baik, B.P. Gila, C.R. Abernathy, Pearton, S.J. Pearton, C.-C. Pan, G.-T. Chen, J.-I. Chyi, S.S. Park, Sol.-Stat. Elec. 48, 827 (2004)

[97] R. Zeisel, M. W. Bayerl, S. T. B. Goennenwein, R. Dimitrov, O. Ambacher, M. S. Brandt, and M. Stutzmann, Phys. Rev. B 61, R16283 (2000).

[98] "Vertical" rectifier structure is often used in referring to mesa-defined vertical structures (mesa-defined structure in our term) in order to distinguish it from horizontal structures, which has *p-i-n* configuration in a horizontal direction. In our paper, we use the term "full-vertical" to make it differentiate from mesa-defined vertical structures.

[99] H. Lahréche, P. Vennégues, M. Vaille, B. Beaumont, M. Laügt, P. Lorenzini, and P. Gibart, Semicond. Sci. Technol. 14, L33 (1999).

[100] P. Vennégues and H. Lahrèche, Appl. Phys. Lett. 77, 4310 (2000).

[101] B. Moran, M. Hansen, M. Craven, J. Speck, and S. DenBaars, J. Crystal Growth 221, 301 (2000).

[102] R. Kröger, S. Einfeldt, R. Chierchia, Z. Reitmeier, R. Davis, and Q. Liu, J. Appl. Phys. 97, 083501 (2005).

[103] A. Petersson, A. Gustafsson, L. Samuelson, S. Tanaka, and Y. Aoyagi, MRS Internet J. Nitride Semicond. Res. 7, 5 (2002).

[104] S. Heikman, S. Keller, S. DenBaars, U. Mishra, F. Bertram, and J. Christen, Jpn. J. Appl. Phys., 42, 6276 (2003).

[105] W. G. Perry, T. Zheleva, M. D. Bremser, R. F. Davis, W. Shan, and J. J. Song, J. Electron. Mater., 26, 224 (1997).

[106] Y. Huang, X. D. Chen, S. Fang. D. Beling, C. C. Ling, X. Q. Dai, and M. H. Xie, Appl. Phys. Lett. 86, 122102 (2005).

[107] 1-D Poisson by Prof. Gregory Snider with the University of Notre Dame was used.

[108] ISE TCAD is two-dimensional device simulation software, which includes the MDRAW device design tool and the DESSIS simulator available from Integrated Systems Engineering, Inc, San Jose, California.

[109] SRIM (Stopping and Range of Ions in Matter) software by Dr. James Ziegler at the United States Naval Academy was used.

[110] B.S. Shelton, T.G. Zhu, D.J.H. Lambert, and R.D. Dupuis, IEEE Trans. Electron. Dev. 45, 1498 (2001)

[111] L. Chernyak, A. Osinsky, H. Temkin, J.W. Yang, Q. Chen, and M.A. Khan, Appl. Phys. Lett. 69. 2531, (1996)